

ESTIMATION OF EFFECTIVE
COMPRESSIBILITY AND PERMEABILITY OF
POROUS MATERIALS WITH DIFFERENTIAL
ACOUSTIC RESONANCE SPECTROSCOPY

A DISSERTATION
SUBMITTED TO THE DEPARTMENT OF GEOPHYSICS
AND THE COMMITTEE ON GRADUATE STUDIES
OF STANFORD UNIVERSITY
IN PARTIAL FULFILLMENT OF THE REQUIREMENTS FOR THE DEGREE
OF
DOCTOR OF PHILOSOPHY

Chuntang Xu

May 2007

© Copyright by Chuntang Xu 2007

All Rights Reserved

I certify that I have read this dissertation and that in my opinion it is fully adequate, in scope and quality, as dissertation for the degree of Doctor of Philosophy.

(Jerry M. Harris) Principal Advisor

I certify that I have read this dissertation and that in my opinion it is fully adequate, in scope and quality, as dissertation for the degree of Doctor of Philosophy.

(Mark Zoback)

I certify that I have read this dissertation and that in my opinion it is fully adequate, in scope and quality, as dissertation for the degree of Doctor of Philosophy.

(Anthony R. Kavscek)

I certify that I have read this dissertation and that in my opinion it is fully adequate, in scope and quality, as dissertation for the degree of Doctor of Philosophy.

(Jack P. Dvorkin)

Approved for the University Committee on Graduate Studies

Abstract

Interpreting the flow properties of saturated porous materials from their acoustic responses at low frequencies scale has been a goal of geophysics research for decades. This thesis describes Differential Acoustic Resonance Spectroscopy (DARS), a robust acoustic method we have developed for studying the flow properties of porous materials at a kilohertz frequency scale. The work is subdivided into five parts: Design and build of a low-frequency laboratory measurement system; Establish measurement quality control; Measure and analyze laboratory measurements; Develop an analytical model for dynamic diffusion in porous media; Verify the analytical model with a finite-element numerical approach.

The primary contribution of this study is that we estimate the effective compressibility of fluid-saturated porous media under a low-frequency, dynamic fluid load; we construct an analytical model linking the flow properties with the effective compressibility; and we propose a robust way to estimate the permeability of earth materials under a transient flow condition. The method is applied to a broad range of rock types.

Acknowledgments

I would like to express my deep and sincere gratitude to my supervisor, Professor Jerry M. Harris not only for convincing me to try to obtain a Ph.D. by joining his talented group, but also for his insistent enthusiasm and his many valuable contributions to this work. His wide knowledge and logical way of thinking have been of great value for me. His understanding, encouraging and personal guidance have provided a good basis for the present thesis.

I feel privileged to have interacted with all of my dissertation committee members. I am grateful to Prof. Mark Zoback for his enlightened questions and suggestions, and to Prof. Anthony Kovscek for his support and inspiring advice. I thank Dr. Jack Dvorkin for insightful discussions about wave behavior in fluid-saturated porous media.

I owe my sincere gratitude to Professor Roland N. Horne, who sponsored my Master's degree in the Department of Petroleum Engineering. I also would like to thank him for chairing my defense.

I warmly thank Guoqing (Tom) Tang for his valuable help in the rock sample preparation, and for his companionship in many games.

I wish to thank Youli Quan for his extensive help in analytical model construction, numerical study, lab results discussion and valuable insights into some lab measurements. Dr. Hengshan Hu and Dr. Pratap M. Sahay's valuable discussions about the fluid flow inside porous media are also appreciated.

I owe many thanks to Manika Prasad for her efforts in helping me in the lab experiments and intensive discussions. Her contribution on ultrasound velocity measurements deserves mentioning. I would also like to thank the SRB group for providing facilities for rock measurements.

During this work I have collaborated with many colleagues for whom I have great regard, and I wish to extend my warmest thanks to all those who have helped me with my work in the Department of Geophysics at Stanford.

I owe my loving thanks to my wife Yan Deng, my daughter Taotao and my son Eric. They have lost a lot due to my research abroad. Without their encouragement and understanding it would have been impossible for me to finish this work. My special gratitude is due to my dad, Fangtian Xu, my mom, Xiugui Zhang, my three older sisters and their families, and my in-laws for their loving support.

My English mentor, Mr. Franklin M. Barrell and his wife Mrs. Constance P. Barrell really deserve mentioning here. They not only helped me improve my English speaking, but also gave me valuable guidance in my personal life. Mrs. Claudia Baroni's great help is also appreciated. She not only proofread my thesis, but also provided great financial management for the whole group.

To conclude, I would like to thank many of my friends at Stanford, Liping Jia and her family, Tuanfeng Zhang and his family, Jing Wan, Pengbo Lu, Yuguang Chen, Yuhong Liu, and many other friends for their valuable help and warm support.

The financial support by Stanford University, the Department of Geophysics, the SWP group, the GCEP project, and the Joshua L. Soska fellowship are gratefully acknowledged.

Stanford, Palo Alto, Nov 2006

Chuntang Xu

Table of contents

Chapter 1	Introduction	1
1.1	Motivation and research objectives	1
1.2	Chapter descriptions	2
Chapter 2	DARS concept and preliminary results	5
2.1	Summary	5
2.2	Introduction	5
2.3	DARS Perturbation theory	8
2.3.1	Modulus contribution to frequency shift	10
2.3.2	Density contribution to frequency shift	11
2.4	DARS apparatus	12
2.5	Experimental results	13
2.6	Compressibility results	18
2.7	Conclusions	26
Chapter 3	Dynamic diffusion process	27
3.1	Summary	27
3.2	Introduction	27
3.3	Theory	30
3.3.1	Effective compressibility	31
3.3.2	Effective compressibility at pressure equilibrium	32
3.3.3	Effective compressibility in the undrained state	33
3.4	Numerical simulation of 1D diffusion	34
3.4.1	Numerical expression of effective compressibility	34
3.4.2	Model description and results	36
3.5	Comparison of compressibility	40
3.5.1	Compressibility at varying frequency	40
3.5.2	Compressibility at varying permeability	44
3.5.3	Compressibility at varying porosity	46
3.6	Numerical simulation of 3D diffusion	48
3.6.1	Numerical result of pressure distribution	49
3.6.2	Numerical result of compressibility at varying frequency	52
3.7	Conclusions	54
Chapter 4	Comparison of lab and analytical results	56
4.1	Summary	56
4.2	Experimental procedure	56
4.2.1	Sample preparation	59
4.2.2	Drained and undrained measurements	59
4.3	Data preparation	61
4.4	DARS estimated compressibility	63

4.5	Compressibility calculated from the analytical model	65
4.6	Results analysis and discussion	67
4.6.1	Comparison of drained and undrained results	67
4.6.2	Comparison of analytical and experimental results	68
4.7	Conclusions	74
Chapter 5	Applications of DARS	75
5.1	Summary	75
5.2	Permeability estimation	75
5.3	Estimating Gassmann wet frame compressibility	80
5.4	Conclusions	85
Chapter 6	Practical considerations	86
6.1	Summary	86
6.2	Potential factors affecting DARS measurement	86
6.2.1	Temperature drift	87
6.2.2	Sample size	88
6.2.3	Sample shape	89
6.3	Error analysis	91
6.3.1	Error associated with temperature variation	92
6.3.2	Instrument error	96
6.3.3	Error associated with perturbation theory	96
6.3.4	Error associated with sample volume measurement	99
6.4	Effect of open flow surface on effective compressibility	101
6.5	Diffusion depth discussion	103
6.6	Conclusions	106
Chapter 7	Summary of conclusions and assumptions	107
7.1	Differential Acoustic Resonance Spectroscopy	107
7.2	General conclusions	108
7.3	Major assumptions	108
Appendix A	Standing wave	110
Appendix B	Nonlinear curve fitting	112
Appendix C	Sample preparation	115
Appendix D	1D diffusion equation	116
Appendix E	Effective compressibility	123
E.1	Static effective compressibility	123
E.2	Dynamic effective compressibility	124
Appendix F	Crossover frequency	128
Appendix G	Permeability estimation	131
Bibliography	133

List of tables

Table 2-1. Acoustical properties of five solid materials.....	14
Table 2-2. Acoustical properties of eight wet rock samples.	15
Table 2-3. Dimensions of the five solid materials.....	20
Table 2-4. DARS results of the five solid materials.....	21
Table 2-5. Dimensions of the eight rock samples	22
Table 2-6. DARS results of the eight rock samples	23
Table 3-1. Common parameters used in finite element model.....	37
Table 3-2. Modeling parameters of finite element simulation	48
Table 4-1. Physical properties of seventeen rock samples	57
Table 4-2. Dimensions of seventeen rock samples.	58
Table 4-3. Frequency results of 17 rocks from DARS drained and undrained measurements.	62
Table 4-4. Compressibility of 17 rocks from DARS drained and undrained measurements.	64
Table 4-5. Compressibility of 17 rocks estimated from the analytical model.....	66
Table 4-6. Compressibility of drained samples given by DARS and the analytical model.	72
Table 5-1. Permeability of 17 rocks given by drained DARS and measured by gas injection.	78
Table 5-2. Wet-frame compressibility of 17 samples given by undrained DARS and derived from ultrasonic velocity measurement.....	83
Table B-1. Frequency data and compressibility of 5 nonporous samples.	114

List of figures

Figure 2-1. DARS responses with and without a tested sample.....	7
Figure 2-2. DARS resonance curve.....	8
Figure 2-3. Diagram of DARS setup.....	12
Figure 2-4. Frequency spectrum of DARS with an aluminum placed at different locations..	16
Figure 2-5. Resonant frequency profiles recorded by DARS.....	17
Figure 2-6. Comparison of compressibility estimated by DARS and calculated by ultrasound velocity and density measurements for five nonporous samples.....	24
Figure 2-7. Comparison of compressibility interpreted by DARS measurement and those calculated by ultrasound velocity and density measurements for the eight rocks.	25
Figure 3-1. Finite element model of a 1D diffusion regime.....	37
Figure 3-2. COMSOL Numerical result of the 1D diffusion model..	38
Figure 3-3. Diffusion pressure given by the 1D analytical model and numeric simulation.....	39
Figure 3-4. Effective compressibility at varying frequencies with permeability parameterized.	42
Figure 3-5. Effective compressibility at varying frequencies with porosity parameterized.....	43
Figure 3-6. Effective compressibility at varying permeabilities with porosity parameterized..	45
Figure 3-7. Effective compressibility versus porosity with permeability parameterized.....	47
Figure 3-8. 3D diffusion model.....	49
Figure 3-9. COMSOL Numerical results of diffusion pressure field.....	50
Figure 3-10. Diffusion pressure distribution in the central radial plane.....	50
Figure 3-11. Diffusion pressure distribution along the axis of the model.....	51
Figure 3-12. Effective compressibility versus frequency with permeability parameterized.....	53
Figure 4-1. Sample surface boundary configuration.....	60
Figure 4-2. Comparison of compressibilities of 17 tested samples estimated by drained and undrained DARS measurements.....	67
Figure 4-3. Comparison of compressibilities estimated by drained DARS and calculated by the analytical model without correction.....	68
Figure 4-4. Ratio of acoustic pressure of DARS sample-loaded cavity and empty cavity.....	69

Figure 4-5. Comparison of compressibilities of 17 tested samples estimated by drained DARS and calculated by the modified analytical model after correction	73
Figure 5-1. Comparison of permeabilities of 17 samples estimated from DARS drained measurement and measured by direct gas injection.....	79
Figure 5-2. Comparison of wet-frame compressibilities of 17 samples estimated by DARS undrained measurement and derived from ultrasonic velocity measurement.....	84
Figure 6-1. Acoustic velocity versus temperature for silicone oil.....	87
Figure 6-2. Density versus temperature for silicone oil.	88
Figure 6-3. Frequency shift versus sample volume.....	90
Figure 6-4. Sensitivity of estimated bulk modulus and compressibility to temperature drift in DARS measurement.	93
Figure 6-5. Correlation of errors in estimated compressibility and bulk modulus with the uncertainty in the volume of tested samples	94
Figure 6-6. Resonance frequency drift with temperature variation of DARS apparatus.....	95
Figure 6-7. Error in estimated compressibility and bulk modulus caused by discrepancy between the length of the reference sample and that of the tested sample	98
Figure 6-8. Sensitivity of estimated bulk modulus and compressibility to the uncertainties in the volume of the tested sample.....	99
Figure 6-9. Correlation of errors in estimated bulk modulus and compressibility with the uncertainties in the volume of the tested sample	100
Figure 6-10. Configuration of the surface boundary for four Berea samples.....	102
Figure 6-11. Effective compressibility versus open flow surface area.....	103
Figure 6-12. Ratio of diffusion depth to sample length for rocks with varying permeabilities	105
Figure B-1. Lorentzian curve-fitting technique.....	113
Figure D-1. Configuration of mass divergence in an arbitrary domain.....	116
Figure D-2. Pore pressure distribution inside a porous medium under a dynamic fluid-loading condition.	122
Figure E-1. For a porous sample with cylindrical shape and side surface being sealed, the fluid flow happens only at the two open ends.	126

Chapter 1

Introduction

1.1 Motivation and research objectives

Wave propagation through fluid-saturated earth materials creates complex interaction between the fluid and solid phases. The presence of pore fluid not only acts as a stiffener to the material, but also results in the flow of the fluid between regions of higher and lower pore pressure (Mavko et al., 1979; Murphy et al., 1986; Mavko et al., 1991; Norris, 1993; Dvorkin et al., 1995; Pride et al., 2003). When a compressional wave squeezes the medium, local pressure gradients build up as a consequence of the matrix deformation and subsequent flow of the local pore fluid. The behavior of fluid in the pore space makes the elastic moduli of the rock frequency-dependent (Mavko et al., 1991). 1) At high frequencies, the fluid in the pore structures becomes isolated, causing the rock to be stiffer. 2) At median and low frequencies, the bulk moduli of the porous medium depend on not only the flow properties of the medium, but also the frequency of the passing wave; this frequency dependence of moduli is often connected with the attenuation of seismic waves (White, 1975; Norris, 1993; Dvorkin et al., 1995; Winkler, 1995; Johnson, 2001; Pride et al., 2004).

The local-fluid-flow mechanism was thought to be the only mechanism that could account for the observed variations of compressional and shear-wave attenuations with frequency in partially and fully saturated rocks (Jones, 1986; Bourbie et al., 1987; Sams, 1997). However, no single theory can adequately describe the link between flow properties (permeability, porosity and saturation) and seismic properties, a goal which has been a target of rock-physics research for decades.

This study is driven by laboratory research and based on rational rock physics and flow mechanics of porous media. The basic scientific contribution of this study is that, for the

first time, based on robust experimental results, it provides a specific link between flow properties and the effective compressibility of porous media.

1.2 Chapter descriptions

The goal of this thesis is to develop a reliable laboratory method to investigate the acoustic properties of porous media at a frequency scale close to that of field seismic studies, and to study the link between the acoustic properties and flow properties of earth materials. This thesis is organized as follows:

Chapter 2 describes the construction of a bench top apparatus for measuring the acoustic properties of fluid-saturated porous media under a dynamic fluid-loading condition, mimicking the complicated fluid and solid interaction during wave propagation. In this chapter, I describe the principles of a Differential Acoustic Resonance Spectroscopy (DARS, Harris, 1996) to estimate the acoustic properties of porous media in a frequency range close to that of field seismic. I establish a resonance-spectrum-fitting procedure to automatically and precisely locate the peak resonance frequency and linewidth. I develop a program to calculate the effective compressibility of the sample from the perturbed frequency. This chapter also summarizes the measurement of a set of nonporous materials and porous materials. I estimate the compressibilities of these samples and find that the nonporous samples and real porous rocks demonstrate dramatically different behavior in DARS measurement. The porous materials appear softer in DARS than in the ultrasonic measurements. The derived compressibilities of the porous samples were larger than those given by ultrasonic measurements. However, the compressibilities of the nonporous samples quantified from DARS agree well with those obtained from ultrasonics. The overestimation of the compressibility of porous materials by DARS motivated us to investigate the interaction between the solid and fluid phases in porous media.

Chapter 3 covers the analytical study and numerical simulation of dynamic diffusion in fluid saturated porous media. I derive an analytical compressibility model which connects the effective elastic moduli of fluid bearing porous materials with flow properties of the media. I propose to use this analytical model to interpret the DARS-measured compressibility of porous samples and to estimate the permeability of these materials. I use a finite-element model (COMSOL) to simulate the dynamic diffusion phenomenon in finite porous media and

compare the numerical result of the pressure inside the medium with that given by the analytical solution; the results agree well. I then use the numerical pressure distribution to calculate the dynamic-flow-related compressibility of the medium and compare the result with that derived from the analytical compressibility model; again, the results agree well. The numerical simulation provides the potential to study the flow properties of porous materials with irregular shapes the analytical solution cannot handle. It also provides a way to calculate compressibility under various conditions not possible by the analytical model, e.g., heterogeneity.

Chapter 4 compares the effective compressibility estimated by an analytical model with that given by DARS measurement for 17 porous samples. I calculate their effective compressibility from DARS and also estimate their compressibility with the analytical model, using porosity and permeability information measured with standard and routine rock-physics methods. The comparison shows good agreement, which confirms that the fluid and solid interaction in DARS measurement is a dynamic-diffusion process. Since the derivation of the analytical model in Chapter 3 demonstrated that the effective compressibility of porous media is a function of permeability and porosity, I propose an approach to estimate the permeability of porous media by combining the analytical compressibility model with DARS-quantified compressibility.

Chapter 5 focuses on the potential applications of the DARS method, establishing a way to estimate the permeability of earth materials by combining DARS compressibility with the analytical effective compressibility model. I also propose an approach to estimate the Gassmann wet-frame bulk modulus (Gassmann, 1951) of porous materials at frequencies on the order of a kilohertz using an undrained DARS measurement. I estimate the permeability of 17 samples and compare the estimated permeability with that given by direct gas-injection measurements. Permeability given by the two different methods agrees well for materials with intermediate values of permeability, e.g., tens of mD to several Darcies. However, for materials with ultra-low permeability, e.g., less than 1 mD, and ultra-high permeability, e.g., over 10 Darcy, the analytical-DARS approach may yield over- or under-estimation of permeability.

Chapter 6 summarizes the potential sources of error in DARS method and how they affect DARS results. I conduct a numerical analysis of the affecting factors and the errors they produce in compressibility estimates. The uncertainty in the sample volume and the temperature drift during DARS measurement are the two dominant error sources. However,

these two factors are controllable, and their effect can be reduced by adopting appropriate measurement practices. The other error sources, which are related to the accuracy of the DARS instrument and DARS perturbation theory, are inevitable, but their effects are relatively small compared to the other sources, and can be reduced using numerical models.

Chapter 7 is a summary of the accomplishments and findings of this thesis.

Chapter 2

DARS concept and preliminary results

2.1 Summary

The interpretation of the acoustic properties of saturated porous materials from acoustic responses at field-seismic frequencies has been discussed for decades. For conventional travel time measurements, the frequency is constrained, by the size of the sample, to be in the ultrasonic range. For field sonic logs, the frequency is much lower than ultrasonic, in the kilohertz range. This disparity between routine acoustic and seismic measurement techniques makes it difficult to couple and interpret information at different frequencies. The goal of this project is to investigate the acoustic properties of porous media based on a Differential Acoustic Resonance Spectroscopy (DARS) technique, which works in kilohertz range.

This chapter summarizes the DARS concept and presents measurements from a set of nonporous materials and rocks using a newly developed DARS setup. The compressibility of several nonporous samples as measured with DARS closely matches that obtained from ultrasonic experiments, confirming that the perturbation theory works reliably and the DARS setup can be used to quantify the bulk property of materials. However, the porous materials behaved differently. Porous materials were more compressible, according to DARS, than they were with ultrasound presumably because of free fluid flowing inside the pore structure, driven by the oscillating DARS pressure.

2.2 Introduction

The bulk modulus describes the resistance of the sample to volume change under applied hydrostatic stress. In rock mechanics, the standard way to estimate the bulk modulus

of a rock sample is to measure the density and the ultrasonic p- and s-wave velocities of the sample and then calculate the bulk modulus:

$$K = \rho \left(c_p^2 - \frac{4}{3} c_s^2 \right), \quad (2.1)$$

where K is the bulk modulus, ρ is density, c_p and c_s are the p- and s-wave velocities of the material, respectively. This method is widely used for nonporous and dry porous materials. However, for fluid-saturated porous samples, the velocity measurement results are influenced by the effect of pore fluid inertia at high frequencies. The high-frequency effects of pore fluid on the bulk moduli of porous materials has been studied for decades, especially as it relates to the attenuation of seismic waves in fluid-saturated porous media. Biot (1956a, b; 1962a, b) established a model to describe the solid-fluid interaction in a porous medium during wave propagation. Research on Biot theory demonstrated that his prediction overestimated the bulk modulus and underestimated the measured attenuation at low-frequencies. Mavko and Nur (1975, 1979) and O’Connell and Budiansky (1974, 1977) proposed a microscopic mechanism, due to microcracks in the grains and/or broken grain contacts. When a seismic wave propagates in a rock having a grain-scale broken structure, the fluid builds up a larger pressure in the cracks than in the main pore space, resulting in a flow from the cracks to the pores, which Mavko and Nur (1975) called “squirt flow.” Therefore, the passing wave results in pore pressure heterogeneity in the porous medium, and the pore fluid is driven to flow at pore-scale distances to release the locally elevated pressure. A model to describe this mechanism, which can be applied to liquid-saturated rocks, was provided by Dvorkin et al. (1995). The squirt-flow mechanism seems capable of explaining much of the measured attenuation in the laboratory at ultrasound frequencies. Pride, Berryman and Harris (2004) pointed out, however, that it does not adequately explain wave behavior in the seismic frequency range.

The inertial effect of the pore fluid on the high frequency measurements, e.g., time of signal flight, of porous media limits their application in field seismic data interpretation. To evaluate the physical properties, e.g., the compressibility or bulk modulus, of earth materials at frequencies close to field seismic, Harris (1996) proposed a Differential Acoustic Resonance Spectroscopy approach.

The DARS idea is simple. The resonance frequency of a cavity is dependent on the velocity of sound in the contained fluid. The sound velocity can be easily determined in this way to an accuracy better than 0.05% (Harris, 1996; Moldover et al., 1986; Colgate et al. 1992). In the DARS experiment, we first measure the resonance frequency of the fluid-filled cavity. Next, we introduce a small sample, i.e., rock, into the cavity and measure the change in frequency. Figure 2-1 illustrates an example of the cavity responses with and without the tested sample. Through a combination of calibration and modeling, we determine the compressibility of the sample from the frequency shift. Accurate frequency measurements can be implemented for acoustically small samples at frequencies as low as a few hundred Hertz in the laboratory, i.e., at seismic frequencies.

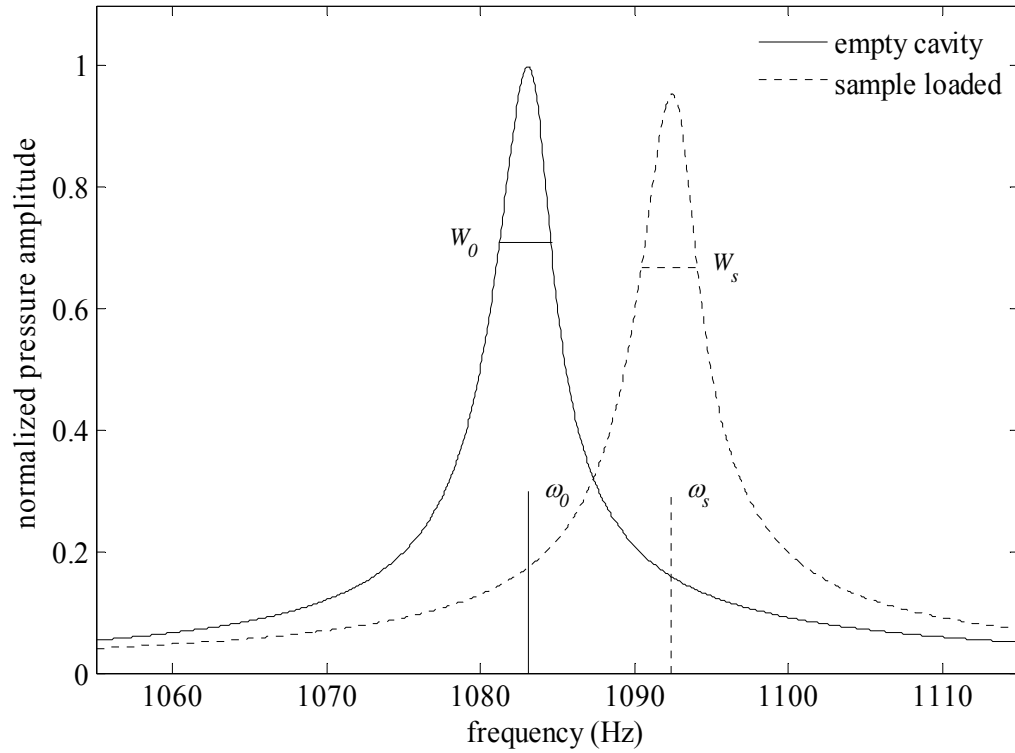


Figure 2-1. DARS responses with and without a tested sample. Parameters ω_0 and ω_s are the resonance frequencies of the empty cavity and sample loaded cavity; W_0 and W_s are the corresponding linewidths.

In the following sections, I will discuss in detail DARS theory and the procedure to estimate the compressibility of fluid-saturated porous media.

2.3 DARS Perturbation theory

A fluid-filled cylindrical cavity (Figure 2-2) with both ends open will vibrate with a fundamental resonance such that the fluid column length is one half the wavelength of the sound wave. In the ideal cavity, each end of the column must be a node for the fluid pressure, since the ends are open.

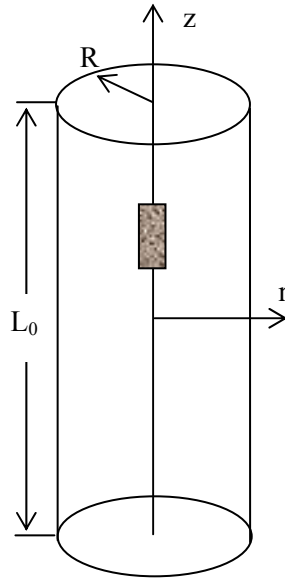


Figure 2-2. A fluid-filled cylindrical resonator with a small sample inside. The resonance frequency will be measured with the sample at different locations in the cavity.

For the fundamental mode, there is one velocity node at the center. The basic wave relationship leads to the frequency of the fundamental (Appendix A):

$$\omega_0 = \frac{\pi c_0}{L_0}, \quad (2.2)$$

where c_0 is the acoustic velocity of the fluid that fills the cavity and L_0 is the cavity length.

The introduction of the sample perturbs the resonance properties of the cavity. The angular resonant frequency shifts from ω_0 to ω_s , Figure 2-1. The frequency perturbation can be expressed as (Morse and Ingard, 1968; Harris, in press)

$$\omega_s^2 - \omega_0^2 = -\omega_0^2 \left(\frac{V_s}{V_c} \right) \frac{\langle p \rangle^2}{\Lambda} \delta\kappa - \omega_0^2 \left(\frac{V_s}{V_c} \right) \frac{\langle \rho_0 c_0 v \rangle^2}{\Lambda} \delta\rho, \quad (2.3)$$

where $\delta\rho = (\rho_s - \rho_0)/\rho_s$ and $\delta\kappa = (\kappa_s - \kappa_0)/\kappa_0$.

In Eqn (2.3), ω_s and ω_0 are the resonance frequencies of the cavity with and without sample respectively; p^2 and v^2 are the corresponding “average” acoustic pressure and particle vibration velocity of the fluid inside the cavity; Λ is a coefficient related to cavity structure; V_s is the volume of the sample, and V_c is the volume of the cavity. The parameters ρ_0 and ρ_s are the densities of the fluid and the sample, respectively; κ_0 is the compressibility of the fluid, defined by $\kappa_0 = (\rho_0 c_0^2)^{-1}$; and κ_s is the compressibility of the sample, given by $\kappa_s = [\rho_s (v_p^2 - 4v_s^2/3)]^{-1}$, where v_p and v_s are the p- and s-wave velocities of the sample.

From Eqn (2.3), the frequency shift caused by the tested sample has two contributions: the compressibility contrast, $\delta\kappa$, and the density contrast, $\delta\rho$, of the tested sample and the background fluid inside DARS cavity. Because most of the earth materials are harder and denser than the fluid inside the cavity; therefore, parameters $\delta\kappa$ and $\delta\rho$ have opposite sign, or in other words, the compressibility and density contrasts between the tested sample and the background fluid contribute oppositely to the frequency shift. This indicates that at some particular locations inside the cavity, the frequency perturbation caused by the compressibility and density contrast may cancel each other. The frequency shift also depends linearly on the sample size, V_s .

To simplify the perturbation expression, I rewrite Eqn (2.3) as

$$\xi = -\frac{\langle p \rangle^2}{\Lambda} \delta\kappa - \frac{\langle \rho_0 c_0 v \rangle^2}{\Lambda} \delta\rho, \quad (2.4)$$

where $\xi = \left[(\omega_s^2 - \omega_0^2) / \omega_0^2 \right] (V_c / V_s)$.

Parameter ξ in Eqn (2.4) is defined as the volume-normalized frequency perturbation, which we use to estimate the compressibility of the samples.

2.3.1 Modulus contribution to frequency shift

As shown in Eqn (2.3), the contribution to the mode shift by the interaction of the object depends on the acoustic contrast between the object and the fluid medium, and also on the relative position of the object inside the cavity because of the spatial distribution of acoustic pressure and velocity. The acoustic pressure distribution for the first mode inside a cylindrical cavity can be approximated as

$$p = p_0 \cos\left(\frac{\omega_0}{c_0} l\right) J_0\left(\frac{\omega_r}{c_0} r\right). \quad (2.5)$$

In Eqn (2.5), coefficient p_0 is the amplitude of the acoustic pressure fluctuation, c_0 is the acoustic velocity of the fluid medium filling the resonator, l and r are longitudinal and radial coordinate inside the resonator, respectively; ω_0 and ω_r are the longitudinal and radial modes respectively. At low frequency, longitudinal resonance dominates the acoustic response in the cavity; consequently, the radial mode, a Bessel's function in Eqn (2.5), will be constant, and the acoustic pressure is a sinusoid in the longitudinal direction. The acoustic velocity is proportional to the spatial derivative of acoustic pressure. Therefore, when a sample is introduced, the resonant frequency either increases or decreases, depending primarily on the velocity and density properties of the sample and also sample location in the cavity (Harris, 1996; Harris etc, 2005).

If the sample is placed at a velocity node, where acoustic pressure is max, then the second term on the right hand side of Eqn (2.4) vanishes. The volume-normalized frequency perturbation, ξ , is linearly dependent on the contrast between the compressibility of the sample and that of the background fluid medium, and Eqn (2.4) can be simplified as follows:

$$\xi = -\frac{\langle p \rangle^2}{\Lambda} \delta \kappa. \quad (2.6)$$

Rearranging Eqn (2.6) yields a compressibility model:

$$\kappa_s = A\xi\kappa_f + \kappa_f, \quad (2.7)$$

where $A = -\Lambda / \langle p \rangle^2$. The coefficient A can be obtained from calibrations using a reference sample.

In Eqn (2.7), κ_f , the compressibility of the fluid inside the cavity, is a given parameter in this study. Therefore, the compressibility of an unknown sample can be quantified by the perturbation it causes to the DARS cavity. The bulk modulus K of the tested sample is simply the reciprocal of the compressibility; therefore, we have

$$K = \frac{1}{\kappa_s} = \frac{1}{A\xi\kappa_f + \kappa_f}. \quad (2.8)$$

2.3.2 Density contribution to frequency shift

If the sample is located at a pressure node, where the velocity is max, then the compressibility contrast term in Eqn (2.4) drops off, and ξ is linearly dependent only on the density contrast between the sample and the background fluid medium. Consequently, Eqn (2.4) reduces to

$$\xi = -\frac{\langle \rho_0 c_0 v \rangle^2}{\Lambda} \delta \rho. \quad (2.9)$$

For nonporous samples, the density is simply the bulk density, which is evaluated by the mass-to-bulk volume ratio. For porous media, however, the pressure gradient inside the fluid phase results in micro-scale fluid flow; therefore the density is affected by fluid inertia and is

no longer the simple bulk density of the sample. In this thesis, I focus on the compressibility of the tested samples, and only in the fundamental resonance mode.

2.4 DARS apparatus

The key component of the DARS apparatus is the cylindrical cavity resonator, which is immersed in a tank filled with fluid – silicone oil in our case. A schematic diagram of the DARS apparatus is shown in Figure 2-3. A pair of piezoceramic discs is used to excite the

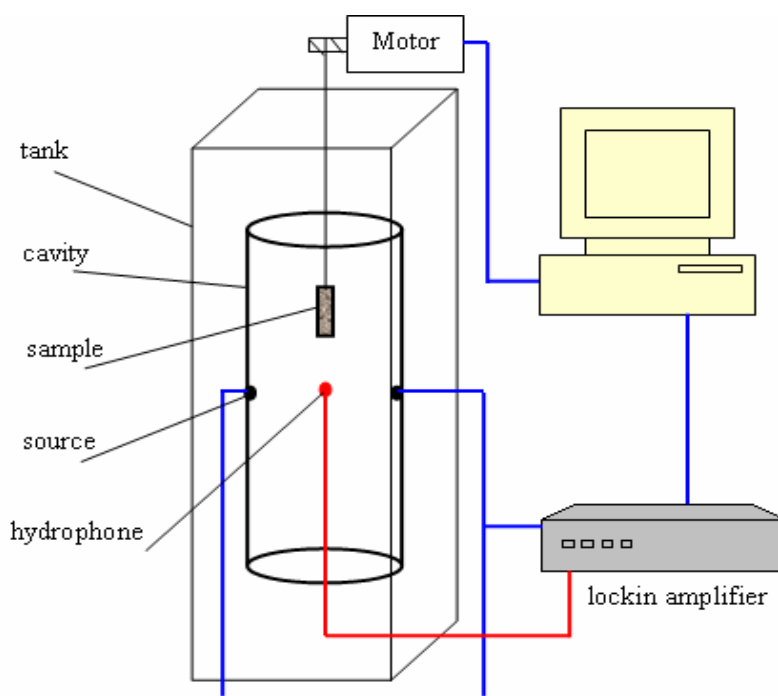


Figure 2-3. Diagram of DARS setup. It includes computer controlled sample positioning and swept frequency data acquisition.

resonator. The disks are embedded in the wall at the longitudinal midpoint of the cavity, where the acoustic pressure is at its maximum for the fundamental mode, thus the disks can efficiently excite the first longitudinal mode. A high-sensitivity hydrophone on the inner surface of the cavity wall, that is also located at the midpoint of the cavity but separated by 90° from the two sources, detects acoustic pressure. The sample is moved vertically along the axis of the cavity to test various conditions of pressure and flow. A computer-controlled stepper motor provides accurate and repeatable positioning of the sample. A lock-in amplifier

is used to scan the frequency, and to track and record a selected resonance curve. A typical scan uses frequency steps of 0.1 Hz from about 1035 – 1135 Hz to cover the first mode. The system is automated and controlled by a computer.

The dimension of the cavity is 15 inches in length and 3.1 inches of internal diameter. The fluid being used in the current system is Dow 200 silicone oil whose nominal acoustic velocity and density, at 20 °C, are 986 m/sec and 918 kg/m³, respectively. The viscosity of the fluid is 5 cs.

2.5 Experimental results

The preliminary measurements involved four plastic materials (Table 2-1) and eight rock samples (Table 2-2). I chose aluminum as the reference sample and used the four plastic samples to test the perturbation theory. The raw DARS measurement results for the reference sample at the first mode are shown in Figure 2-4, with the sample at different locations inside the resonator. At the center of the resonator, the acoustic pressure dominates, and the sample's smaller compressibility increases the frequency compared to that of the resonator without the sample. At the ends of the resonator, the acoustic velocity dominates, and the sample's higher density reduces the frequency compared to that of the resonator without the sample.

Table 2-1. Acoustical properties of five solid materials. Parameter $\kappa_{\text{ultrasound}}$ is calculated with ultrasonic velocities.

	ρ (kg/m ³)	v_p (m/s)	v_s (m/s)	$\kappa_{\text{ultrasound}}$ (GPa ⁻¹)
Aluminum	2700	6320	3090	0.01334
Teflon	2140	1404	750	0.3831
Delrin	1420	2360	1120	0.1808
PVC	1380	2293	1230	0.2237
Lucite	1180	2692	1550	0.2096

Table 2-2. Acoustical properties of eight wet rock samples. Parameter $\kappa_{\text{ultrasound}}$ is calculated with ultrasonic velocities.

	ρ (kg/m ³)	ϕ (%)	k (mD)	v_p (m/sec)	v_s (m/sec)	$\kappa_{\text{ultrasound}}$ (GPa ⁻¹)
SSE1	2152	28.3	4200	3115	1411	0.06588
YBerea7	2398	28	6000	3425	1733	0.05397
SSF2	2210	24.9	1850	3265	1641	0.06398
Berea15	2287	20.85	370	3530	2008	0.06172
Boise8	2419	12	0.9	3593	1852	0.04957
Chalk5	2088	34.5	2.1	3125	1650	0.078
Coal	1133	1.9	0.1	2075	890	0.2717
Granite	2630	0.1	0	5280	2903	0.02284

The frequency profiles of the reference aluminum and the four plastic samples are shown in Figure 2-5a. We can see that the profiles of the moderately compressible materials are systematically distributed between those of the hardest material (Aluminum) and the softest one (Teflon). The soft materials produce less frequency perturbation than the hard ones. The frequency profiles of six rocks are shown in Figure 2-5b. The order of the data traces also shows the same behavior as that of the nonporous samples, the harder and denser materials always show larger perturbation. The general behavior of both the porous and nonporous samples matches the prediction of the perturbation theory.

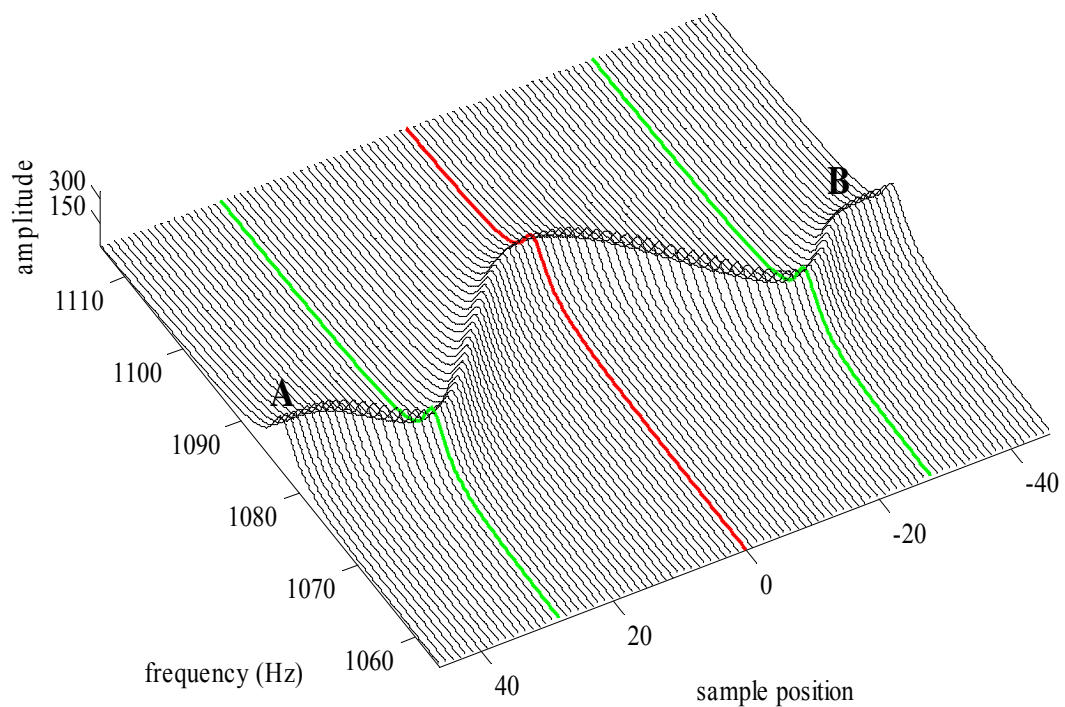
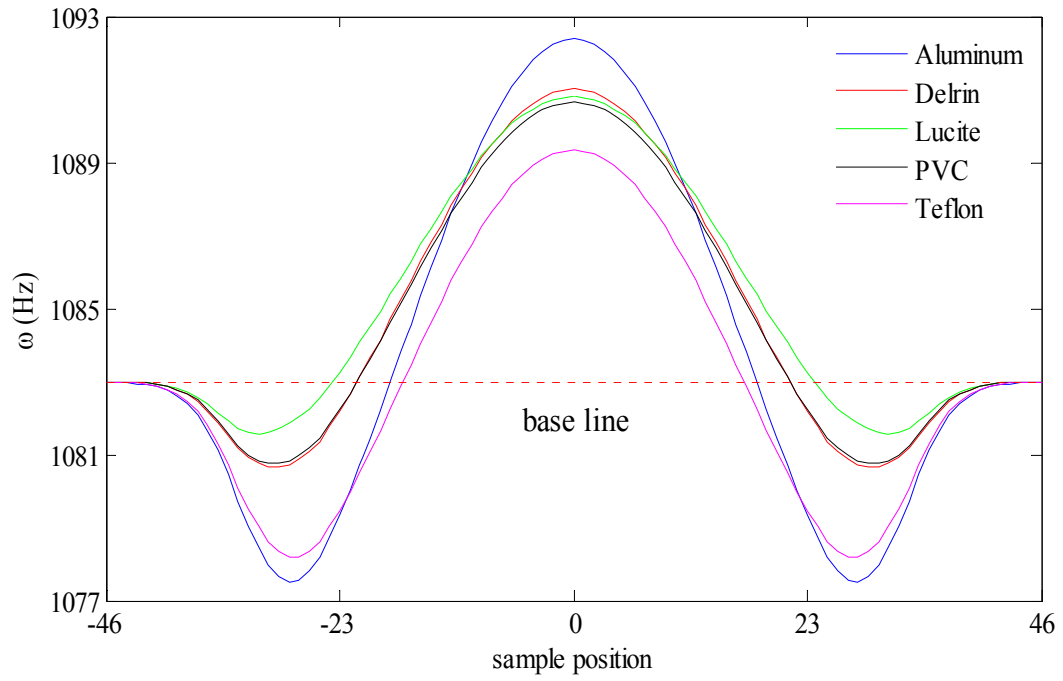
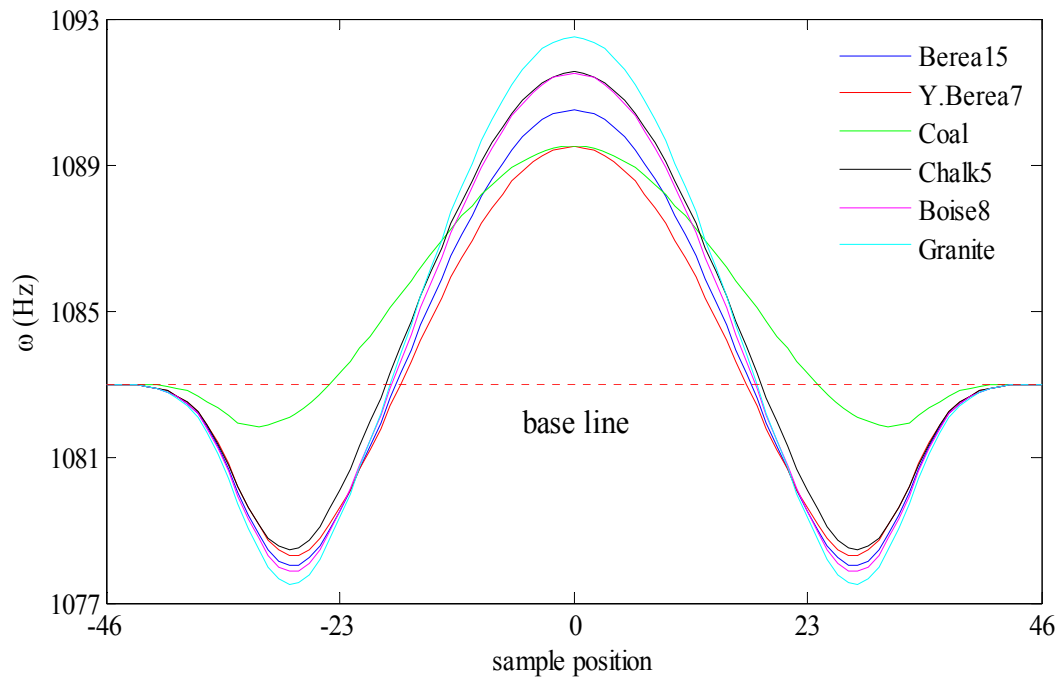


Figure 2-4. Frequency spectrum of the acoustic system with an aluminum sample placed at different locations. The shaded sine shape is the perturbed resonance frequency profile. The red line is the power spectrum corresponding to the case when the sample was centered in the cavity. The two green lines are the power spectra with the sample placed near the two ends of the cavity. The two similar sections labeled A and B are the resonance frequencies with the sample far outside the cavity.



(a)



(b)

Figure 2-5. Resonant frequency profiles recorded by DARS. (a): Nonporous materials. (b): Porous materials.

2.6 Compressibility results

To estimate the compressibility of the tested samples, we record the frequency data with the sample placed at the center of the cavity, where the frequency shift is mainly due to compressibility contrast between the sample and the background fluid medium. The frequency results of the five solid materials and eight porous materials are listed in Tables 2-3 and 2-5 respectively. Also, we need to know the coefficient A in the perturbation model in advance. Normally, we use aluminum as the reference sample to quantify the coefficient A , as follows.

By rearranging Eqn (2.7) we get

$$A = \frac{\kappa_r - \kappa_f}{\xi_r \kappa_f} . \quad (2.10)$$

In Eqn (2.10), the subscript r indicates the reference sample, aluminum, in this case. The compressibility of the reference sample can be quantified by using the ultrasound p- and s-wave velocity measurements and density measurement with Eqn (2.1). To get the parameter ξ_r , we first measure the resonance frequency of the DARS setup with and without the reference aluminum, written as ω_0 and ω_s , respectively. Then, from the definition of ξ , equation (2.4), we can compute ξ_r , immediately. Substituting ξ_r and κ_r of the reference aluminum into Eqn (2.10), we can solve for coefficient A . Plugging the frequency information of the aluminum sample (Table 2-4) into Eqn (2.10) we get the value of A as -0.5936. This value will be held constant over all of the other tested samples.

To obtain the compressibility of the other tested samples, the procedures are as follows: we first calculate the perturbation quantity, ξ , of each sample, then substitute ξ into Eqn (2.7) and (2.8) to calculate the compressibility of the sample. The results of compressibility of the four plastic samples and eight rock samples are listed respectively in Tables 2-4 and 2-6.

The errors in the DARS compressibility estimates of both the nonporous and porous samples are attributed to the uncertainties in the sample volume and temperature drift in DARS experiments (details reference chapter 6, section 6.3.1 and 6.3.4). From Eqn (2.7), DARS compressibility is estimated from the frequency shift caused by the tested sample, and

the frequency shift is a linear dependent of the sample volume. Therefore, the uncertainty in the sample volume will directly affect the accuracy of the compressibility estimate. The sample volume in this thesis is calculated from the sample's length and diameter (listed in Tables 2-3 and 2-5), both of which are an average of five measurements at different locations and orientations. The uncertainties in the length and diameter and thus the calculated volume of the nonporous and porous materials are listed in Tables 2-3 and 2-5, respectively.

Temperature drift used in this thesis refers to the possible temperature change between the two consecutive measurements: DARS empty cavity and sample-loaded cavity measurements. Temperature drift affects DARS observation by affecting the fluid acoustic velocity and thus the resonance frequency. The acoustic velocity of the background fluid inside DARS cavity shows linear dependent on temperature,

$$c_0 = -2.81T + 1051.8,$$

where c_0 is the acoustic velocity of the background fluid and T is ambient temperature.

In the current DARS apparatus, the temperature is loosely controlled at about 22 °C by a room air conditioner, and a slow temperature drift with time always exists in the measurement. The typical rate of temperature change with time is about ± 0.5 °C/12hr. The time interval between the empty cavity and sample-loaded cavity measurements is about 5 minutes; therefore, the possible temperature change between the two consecutive measurements is about ± 0.007 °C. Transferring into frequency through equation (2.2), this temperature change may result in ± 0.026 Hz frequency shift.

Combining the errors in the samples volume and the uncertainty of temperature drift, the possible errors in the compressibility estimates of the nonporous and porous samples are calculated and listed in Tables 2-4 and 2-6, respectively.

To better understand the DARS measurements of compressibility for both nonporous and porous materials, we also take ultrasonic velocity measurements on these materials and use Eqn (2.1) to calculate the compressibility of both the plastics and the porous samples (in fully saturated condition). The results for plastics and wet rocks are listed in Tables 2-1 and 2-2, respectively.

Table 2-3. Dimensions of the five solid materials.

	L (in)	Error in L (%)	D (in)	Error in D (%)	V_s (in ³)	Error in V_s (%)
Aluminum	1.5000	± 0.056	0.9988	± 0.045	1.1762	± 0.145
Delrin	1.4983	± 0.030	0.9979	± 0.055	1.1692	± 0.140
Lucite	1.4972	± 0.094	0.9989	± 0.131	1.1699	± 0.356
PVC	1.5078	± 0.076	0.9956	± 0.071	1.1721	± 0.218
Teflon	1.4960	± 0.067	0.9984	± 0.071	1.1718	± 0.209

Table 2-4. DARS results of the five solid materials

	ω_s (Hz)	ω_0 (Hz)	ξ	κ_{DARS} (GPa ⁻¹)	Uncertainty in κ_{DARS}
Aluminum	1091.5079	1082.1850	1.6669	0.01351	Reference sample
Delrin	1090.0310	1082.0728	1.4263	0.3788	$\pm 2.58\%$
Lucite	1089.4041	1081.6104	1.3956	0.1838	$\pm 3.32\%$
PVC	1089.2622	1081.5922	1.3728	0.2257	$\pm 2.45\%$
Teflon	1088.0883	1081.5785	1.1671	0.2096	$\pm 1.37\%$

Table 2-5. Dimensions of the eight rock samples

	L (in)	Error in L (%)	D (in)	Error in D (%)	V_s (in ³)	Error in V_s (%)
SSE1	1.4907	± 0.169	0.9935	± 0.041	1.1555	± 0.252
YBerea7	1.4585	± 0.109	0.9995	± 0.044	1.1444	± 0.198
SSF2	1.4696	± 0.042	0.9903	± 0.333	1.1318	± 0.710
Berea15	1.4940	± 0.195	1.0000	± 0.067	1.1736	± 0.330
Boise8	1.4802	± 0.174	1.0008	± 0.027	1.1644	± 0.230
Chalk5	1.4855	± 0.115	0.9940	± 0.138	1.1614	± 0.391
Coal	1.3575	± 0.07	0.9965	± 0.056	1.0588	± 0.182
Granite	1.5285	± 0.149	0.9962	± 0.019	1.1914	± 0.188

Table 2-6. DARS results of the eight rock samples

	ω_s (Hz)	ω_0 (Hz)	ξ	κ_{DARS} (GPa ⁻¹)	Uncertainty in κ_{DARS}
SSE1	1089.3487	1082.8674	1.1763	0.3449	±1.5%
YBerea7	1089.3099	1082.8004	1.1931	0.3343	±1.4%
SSF2	1089.5475	1082.8674	1.2378	0.3092	±2.9%
Berea15	1090.2563	1082.6706	1.3568	0.2334	±2.5%
Boise8	1091.1208	1082.6054	1.5356	0.1137	±4.8%
Chalk5	1091.1545	1082.6059	1.5571	0.0995	±7.2%
Coal	1089.1558	1082.6419	1.2907	0.2598	±1.9%
Granite	1092.1532	1082.6337	1.6785	0.0229	±6.1%

We compared the DARS-estimated compressibilities of the four plastic materials with those obtained from the ultrasound measurements. The results are shown in Figure 2-6. The data points of the compressibility cross plots all fall approximately along a 45° line passing through the origin, indicating a strong agreement of the results obtained by the two different methods. Within the error of measurement, applying the same approach to the porous rocks, the cross plots of the compressibility obtained by the two different methods are shown in

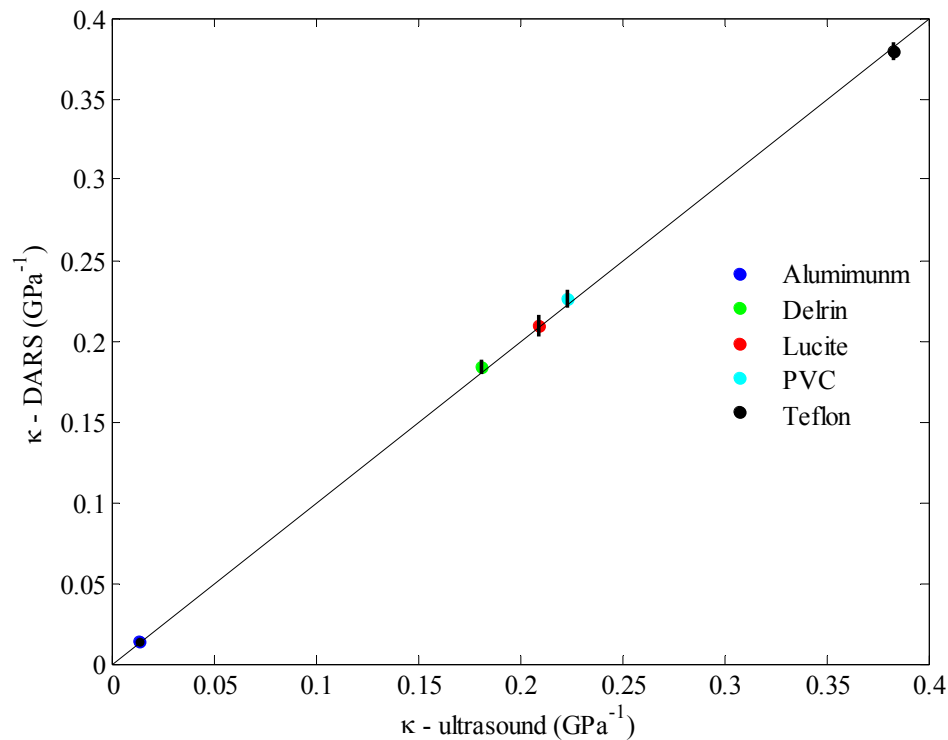


Figure 2-6. Comparison of compressibility estimated by DARS and calculated by ultrasound velocity and density measurements for five nonporous samples. The short vertical bars crossing the data points represent the uncertainty range in DARS compressibility estimates.

Figure 2-7. Samples with low permeability and porosity (coal and granite, e.g) demonstrate similar behavior to that of the nonporous materials — the DARS-predicted compressibility agrees with that obtained by ultrasonic measurements, which indicates that the compressibility given by both techniques are comparable for these particular rocks. However, for the materials with high permeability and porosity, the cross points all fall off the 45° line, and the magnitude of deviation shows permeability and porosity dependence. This behavior is due to

the acoustic-pressure-induced fluid flow through the open flow surface of the samples, which implies that DARS measurements may be useful for interpreting flow properties of porous materials. We will address this phenomenon in Chapters 3.

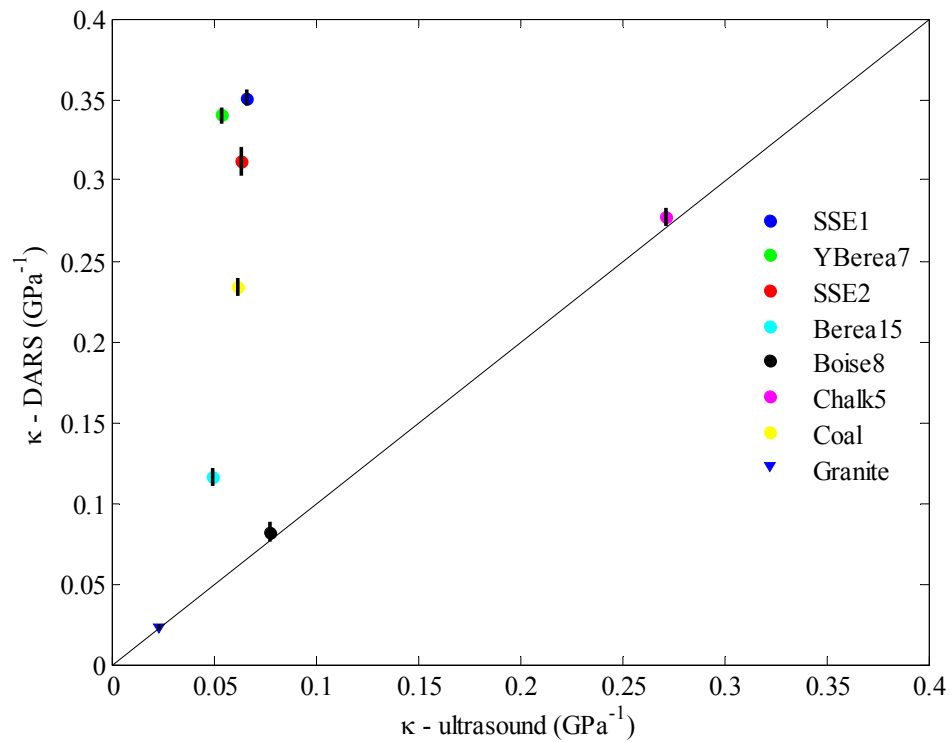


Figure 2-7. Comparison of compressibility interpreted by DARS measurement and those calculated by ultrasound velocity and density measurements for the eight rocks. The rocks are 100% fluid saturated. The short vertical bars crossing the data points represent the uncertainty range in DARS compressibility estimates.

2.7 Conclusions

A custom-designed Differential Acoustic Resonance Spectroscopy (DARS) apparatus was built based on a resonance perturbation theory. The DARS operates on the principle that the introduction of a compressible sample into an acoustic resonator causes perturbation in the resonance modes. By analyzing the difference between fundamental modes with and without a sample, we can characterize the acoustic properties of the sample.

Our methodology for nondestructive measurement allows for rapid, accurate measurement of the compressibility of small samples, based on this newly developed DARS system. The measurement results from four routine plastic samples validated the perturbation theory. The compressibilities estimated from the measurement of these four plastics agree with those derived from ultrasonic velocity and density measurements.

The DARS results from a set of real rocks show that, for low permeability and low porosity materials, the compressibility estimated from DARS agrees with that derived from the ultrasonic velocity measurement. However, for materials with high porosity and permeability, DARS yields higher compressibility than the ultrasonic measurement. This phenomenon motivated us to study fluid and solid interactions in DARS experiment of porous materials.

Chapter 3

Dynamic diffusion process

3.1 Summary

Wave propagation in a fluid-saturated porous medium results in complex interactions between the saturating fluid and the solid matrix. The presence of fluid in the pore space makes the elastic moduli frequency-dependent. The compressibility of a porous medium involves information about the flow properties of the medium. Because the micro-flow associated with acoustic wave does not involve mass transportation of the pore fluid, we call it dynamic flow to distinguish it from conventional flow. In this chapter, I derive a dynamic diffusion model, which relates the effective compressibility to the permeability, and we propose to apply this approach to interpret the DARS experimental results. To verify the analytical solution, I use COMSOL, a finite-element tool, to study the diffusion pressure distribution inside a finite, homogeneous porous medium. I estimate the dynamic-flow-dependent compressibility of the medium from the numerical pressure calculation, and compare the numerically calculated compressibility with an analytical solution for a simple case.

3.2 Introduction

In physical terms, when a fluid-saturated porous material is subjected to stress, the resulting matrix deformation leads to volumetric changes in the pores. Since the pores are fluid-filled, the fluid not only acts as a stiffener of the material, but also flows (diffuses) between regions of higher and lower pore pressure. Therefore, the effective compressibility of the material—the reciprocal of its dynamic bulk modulus—will be a combination of the

compressibility of the solid matrix and an additional compressibility due to the fluid-occupied pore spaces and its ease or difficulty to flow. Similarly, when a passing pressure wave squeezes the rock, local pressure fluctuations develop as a consequence of the matrix deformation and subsequent flow of the local pore fluid.

Within any porous system subject to dynamic flow with a given pore structure and saturating fluid, there is a frequency below which the system is said to be drained. In other words, within the period of the propagating wave, the fluid in the pore space can flow far enough to relieve the local pressure gradients. At low frequencies, fluid loss from high-pressure zones to low-pressure zones reaches a maximum, so that the bulk volume of the high-pressure undergoes maximum shrinkage and demonstrates maximum compressibility. On the other hand, at high frequencies, the time for fluid flow is insufficient for significant flow, and the pressure gradients persist. This latter regime is called an undrained state. Local compressibility is a minimum under undrained conditions, and the rock demonstrates stiffer elastic response. For waves with intermediate frequencies, the compressibility of the rock will be between these two extremes, and will depend on the frequency.

Many theories have been developed to describe the fluid-solid interaction caused by wave propagation, yet no single one fully explains this complex phenomenon (Norris, 1993). Gassmann (1951) derived a simple expression relating the saturated rock bulk modulus to the dry rock bulk modulus and the bulk modulus of the saturating fluid. This theory makes it convenient to estimate the wet bulk modulus of porous materials with different fluids. However, the application is limited to static rather than dynamic cases, frequency-dependent effects need not be considered. Biot (1956a, b, 1962a, b) developed a theory to describe wave propagation in fluid-saturated porous rocks, but his theory is limited to homogeneous materials and is not easily extended to spatially non-uniform media. Furthermore, his model underestimates the observed seismic velocity at high frequencies (Mavko, 1991, Winkler, 1985, 1986). Experiments (Murphy et al., 1984; Wang and Nur, 1988) and models (Mavko and Nur, 1979; O'Connell and Budiansky, 1974, 1977, 1990) suggest that the limitation of Gassmann and Biot at high frequencies is related to neglecting grain-scale microscopic fluid flow induced by the passing wave. Mavko et al. (1991) summarized how heterogeneities, such as variations in pore shape, saturation, and orientation, are likely to produce pore pressure gradients and flow on the scale of individual pores, when a section of rock is excited by a passing wave. The rock appears stiffer in both bulk and shear moduli under unequilibrated

pressure than under equilibrated pressure. However, this mechanism is not considered in Biot's model.

To compensate for the inadequacy of Biot and Gassmann theory, patchy saturation (White, 1975, 1983; Dutta and Ode, 1979a, b; Dutta and Seriff, 1979; Brie et al., 1995; Knight et al., 1998), squirt flow (Mavko and Nur, 1975; Mavko and Nur, 1979; Palmer and Traviolia, 1980; Murphy, et al., 1986; Dvorkin et al., 1993; Dvorkin and Nur, 1993; Dvorkin et al., 1995) and grain-scale microscopic fluid flow (Mavko and Jizba, 1991) mechanisms have been proposed, but still, no single theory is considered sufficient to explain the complex fluid-solid interaction at all frequencies.

The dynamic bulk modulus reflects the elastic wave propagation in fluid-saturated porous media (Lemarinier et al., 1995; Johnson, 1990, 2001; Johnson et al., 1994). Chapter 2 introduced a way to estimate the compressibility or dynamic bulk modulus of nonporous and porous materials using Differential Acoustic Resonance Spectroscopy (DARS). I used DARS to estimate the compressibilities of both nonporous and porous materials and compared the results with those derived by ultrasound measurements. The compressibilities obtained by the two different methods are comparable for nonporous materials (Figure 2-6), but not always for porous samples (Figure 2-7). For samples with extremely low permeability, such as coal and granite, the compressibilities obtained by the two different techniques are close to each other. However, for samples with intermediate and high permeability, such as the two Berea sandstones and the Boise sandstone, the estimates do not agree, and the samples with higher permeability disagree most. Porosity does not have this effect, or at least the effect is not obvious. For instance, the chalk has high porosity; but its compressibility given by the two different measurements are comparable. Another interesting observation in Figure 2-7 is that the DARS-estimated compressibilities of the samples are larger than those derived by ultrasound measurement of both the dry and wet materials, except in coal and granite, which have nearly zero porosity. This phenomenon indicates that the compressibility derived by DARS measurements is apparently not the compressibility usually quantified by other techniques, e.g., ultrasound method.

This observation motivated us to investigate the mechanism of the fluid and solid matrix interaction in the DARS measurements. Because DARS works in kilohertz frequency range, we expect this fluid dynamic study may lend insight into how pore fluid and solid matrix interact during seismic wave propagation in earth materials.

3.3 Theory

In DARS, a standing wave inside the cavity provides a spatially varying but harmonic pressure field in the cavity. In a fluid-saturated porous medium that is subjected to this small-amplitude oscillatory pressure gradient, the pressure fluctuation will cause micro-scale fluid flow through the surface of the sample to release the differential pressure across the surface boundary. The net mass transport of the pore fluid is zero; therefore, this micro-scale flow behaves differently from conventional fluid flow. This dynamic flow phenomenon can be described as a quasi-static diffusion process. If the porous medium is homogeneous, the dynamic flow can be understood through use of a 1D diffusion model (see details in Appendix D):

$$\frac{\partial^2 p}{\partial x^2} = \frac{1}{D} \frac{\partial p}{\partial x}, \quad (3.1)$$

with diffusivity D given by $D = k / \phi \eta \beta$. Here, p is the acoustic pressure in the fluid, ϕ and k are porosity and permeability of the porous sample, respectively, η is the viscosity of the fluid, and β is the compressibility factor involving both the fluid and the solid matrix simultaneously.

Furthermore, if acoustic pressure is harmonic in time, $p(x, t) = p(x)e^{i\omega t}$, we can rewrite Eqn (3.1) as

$$\frac{\partial^2 p}{\partial x^2} - \frac{i\omega}{D} p = 0. \quad (3.2)$$

A general solution of Eqn (3.2) is

$$p(x) = Ae^{\alpha x}. \quad (3.3)$$

Here, $\alpha = \sqrt{i\omega/D}$ in which ω is angular frequency written as $\omega = 2\pi f$.

In our particular case, the dynamic flows are in and out the sample at the two open ends when the exciting mode has longitudinal pressure variations; therefore, the pressure distribution inside the pore space is a superposition of two opposite pressure profiles, with boundary conditions $p(L) = p_0$ and $p(-L) = p_0$, respectively, when the sample is at the center of the cavity.

Applying the two boundary conditions, we get the solution of the pressure field inside the porous sample,

$$p(x) = \frac{e^{\alpha L}}{1 + e^{2\alpha L}} (e^{\alpha L} + e^{-\alpha L}) p_0. \quad (3.4)$$

3.3.1 Effective compressibility

The effective compressibility of fluid-saturated porous materials under a periodic load can be expressed by the ratio of the net volumetric strain of the material to the applied stress on the sample. The net volume change of the sample consists of contributions from the solid matrix and the pore fluid. Therefore, the effective compressibility of the porous sample can be written as

$$\kappa_e = -\frac{1}{V_s} \frac{(\Delta V_m + \Delta V_f)}{p_0}, \quad (3.5)$$

where V_s is the bulk volume of the sample. ΔV_m is the volume change of the frame (the wet frame in this case, because the sample is saturated), and ΔV_f is the volume of the extra amount of fluid flowing in and out the pore space; p_0 is the amplitude of pressure change.

Here we assume the compressibility of the wet matrix is κ_u , hence, ΔV_m can be expressed as

$$\Delta V_m = -\kappa_u V_s p_0. \quad (3.6)$$

The parameter κ_u is defined to be the undrained wet-frame compressibility for fluid-saturated porous materials. This parameter is also recognized as the reciprocal of the Gassmann wet frame bulk modulus. This topic will be discussed in Chapter 5.

In a cylindrical porous sample with a jacketed side surface, diffusion happens only at the two open ends. The volume of the free-flowing fluid can be quantified as follows (details in Appendix E):

$$\Delta V_f = -\int \phi \kappa_f p(x) dV = -\pi r_0^2 \phi \kappa_f \int p(x) dx . \quad (3.7)$$

Rewriting Eqn (3.5) by substituting (3.4), (3.6) and (3.7) into it, we get the final expression for the effective compressibility,

$$\kappa_e = \kappa_u + \frac{\phi \kappa_f}{\alpha L} \frac{e^{2\alpha L} - 1}{e^{2\alpha L} + 1}, \quad \alpha = \sqrt{\frac{i\omega}{D}} = \sqrt{\frac{i\omega \phi \eta \kappa_f}{k}} . \quad (3.8)$$

The second term on the right hand side of equation (3.8) is named as the dynamic flow component of compressibility.

Equation (3.8) shows that the effective compressibility of a fluid-saturated porous material under periodic loading is simply the superposition of the wet-frame compressibility and a nominal contribution from the amount of fluid flowing into and out of the sample, in this case longitudinally. This model also indicates that micro-scale fluid flow induced by wave propagation in fluid-saturated porous media has a softening effect that exists at any frequency scale, although the magnitude of the effect varies with frequency. Moreover, the dynamic flow contribution to compressibility is a function of porosity, permeability and fluid viscosity; therefore, this effective compressibility model provides a way to analyze the effect of these flow properties by studying effective compressibility.

3.3.2 Effective compressibility at pressure equilibrium

When the ratio of frequency to diffusivity is small, $\omega/D \ll 1$, e.g., low frequency or high permeability, the exponential term on the right hand side of Eqn (3.8) can be approximated by a Taylor expansion as follows:

$$e^{2\alpha L} \approx 1 + 2\alpha L. \quad (3.9)$$

We can further approximate Eqn (3.8) as

$$\kappa_e \approx \kappa_u + \frac{\phi \kappa_f}{1 + \alpha L}. \quad (3.10)$$

Because $\alpha L \ll 1$, we get a simplified expression for the effective compressibility at low frequencies:

$$\kappa_e = \kappa_u + \phi \kappa_f. \quad (3.11)$$

3.3.3 Effective compressibility in the undrained state

When the ratio of $\omega/D \gg 1$, in other words in high frequency or low permeability situations, both the expression $e^{2\alpha L}$ and the parameter αL will approach infinity, and Eqn (3.8) can be simplified as follows:

$$\kappa_e \approx \kappa_u. \quad (3.12)$$

Under this scenario, the wet-frame compressibility dominates the effective compressibility of the sample, and the contribution by the free-moving fluid can be neglected.

Physically, pore fluid flow is restricted under high-frequency loading or in a low-permeability porous medium, thus the pressure gradient across the boundary of the sample surface remains. The frame matrix and the pore fluid counteract the loading pressure together and both undergo identical deformation.

The approach for quantifying κ_u with DARS will be addressed in Chapter 5, which discusses experimental results.

3.4 Numerical simulation of 1D diffusion

To verify the analytical results of diffusion pressure and effective compressibility, in this section, we applied COMSOL, a finite-element tool, to simulate the diffusion inside a cylindrical, finite, homogeneous porous medium. We introduce the finite element simulation here because it gives us the potential and flexibility to handle realistic configurations (heterogeneity, etc.) that are impossible with the analytical study. We first consider the simple 1D diffusion problems. In section 3.5, we will discuss 3D diffusion problem.

3.4.1 Numerical expression of effective compressibility

The analytical expression of the dynamic-flow component of compressibility is

$$\kappa_{flow} = \frac{\phi \kappa_f}{\alpha L} \frac{e^{2\alpha L} - 1}{e^{2\alpha L} + 1}, \quad \alpha = \sqrt{\frac{i\omega}{D}} = \sqrt{\frac{i\omega\phi\eta\kappa_f}{k}}. \quad (3.13)$$

This expression is derived from the volume integral of the pressure profile, Eqn (3.4), in the pore space of the studied porous sample (details in Appendix E).

The numerical approach to calculating the effective compressibility is similar to the analytical process. The COMSOL simulation yields the pressure in a set of meshed elements. Therefore, we can estimate the amount of fluid stored in each element by using the definition of compressibility,

$$\Delta V_i = -\phi \kappa_f p_i dV_i, \quad (3.14)$$

where p_i and dV_i represent the pressure and volume of the i -th element. Parameter ϕ is the porosity of the medium, and κ_f is the compressibility of the pore fluid.

Hence, the total amount of the fluid involved in the dynamic flow during the half wave period will be

$$V_f = \sum_{i=1}^N \Delta V_i = -\phi \kappa_f \sum_{i=1}^N p_i dV_i, \quad (3.15)$$

where N is the number of meshed elements.

Finally, we get the expression of compressibility given by the numerical pressure results as follows:

$$\kappa_{flow} = -\frac{1}{V_s} \frac{V_f}{p_0} = \frac{1}{V_s} \frac{\phi \kappa_f \sum_{i=1}^N p_i dV_i}{p_0}, \quad (3.16)$$

where V_s is the bulk volume of the studied domain and is given by $V_s = 2\pi r_0^2 L$, in which r_0 and L are the radius and half-length of the domain, respectively. The summation expression, $\sum_{i=1}^N p_i dV_i$, can be obtained by a sub-domain integration, a built-in function in COMSOL.

The numerical expression of the effective compressibility will be

$$\kappa_e = \kappa_u + \frac{1}{V_s} \frac{\phi \kappa_f \sum_{i=1}^N p_i dV_i}{p_0}. \quad (3.17)$$

Following we will compare the diffusion pressure distribution and dynamic-flow contribution to compressibility given by the analytical model with that derived from the numerical result. And we extend this computational model to heterogeneous case.

The results in this section are conditioned from Berea sandstone, of which the dry bulk density is 2.2 g/cc and, the dry p-wave and s-wave velocities are 2.64 km/sec and 1.65 km/s, respectively. The permeability and porosity of the sample are 500 mD and 20%, respectively. The effects of frequency, permeability and porosity on the effective compressibility of the sample are discussed below.

3.4.2 Model description and results

The simulated object is a finite cylindrical shaped rock sample. The cylinder surface of the sample is covered with a thin layer of non-permeable material. The two open ends of the sample are subject to dynamic fluid loading; therefore, the fluid can freely flow across the open surface boundaries. We further assumed that there is no cross flow in the radial direction, and the flow is purely along the axis of the sample. We accordingly constructed a finite element model of which the meshed plot is shown in Figure 3-1. The cylindrical surface of the model is non-permeable, and diffusion can occur only at the two open ends. The modeling parameters are listed in Table 3-1, and three permeabilities are studied.

Figure 3-2 illustrates the numerical results of the diffusion pressure distribution inside the medium. The pressure decreases systematically and symmetrically from the two ends of the sample. Since the model is homogeneous, no transverse flow forms in the radial direction, and the pressure field in the radial plane is always uniform (Figure 3-2).

We studied the numerical result of the diffusion pressure profile along the axial direction and compared it with the analytical result. Figure 3-3 shows the comparison of the real and imaginary components of the pressure profile. Clearly, the diffusion pressure results given by the two methods agree reasonably well, as they should. However, we also noticed that the numerical solution will yield error at low permeability. This can be seen for the 10 mD case in Figure 3-3. The imaginary part of pressure clearly shows disagreement, but on the real part of pressure, this is not apparent.

The good agreement of the diffusion pressure results given by the two different methods indicates that we can apply the numerical approach to estimate the dynamic-flow component of compressibility in porous media. The following section will focus on this topic.

Table 3-1. Common parameters used in finite element model.

Length (mm)	38.1
Radius (mm)	25.4
Permeability (mD)	10, 100, 1000
Porosity (%)	20
Viscosity (cts)	5
Fluid compressibility (GPa^{-1})	1.1204
Frequency (Hz)	1000

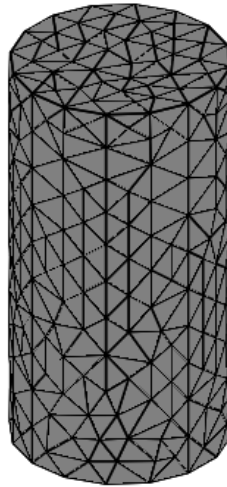


Figure 3-1. Finite element model of a 1D diffusion regime. Diffusion is along the axial direction. The cylinder surface is non-permeable.

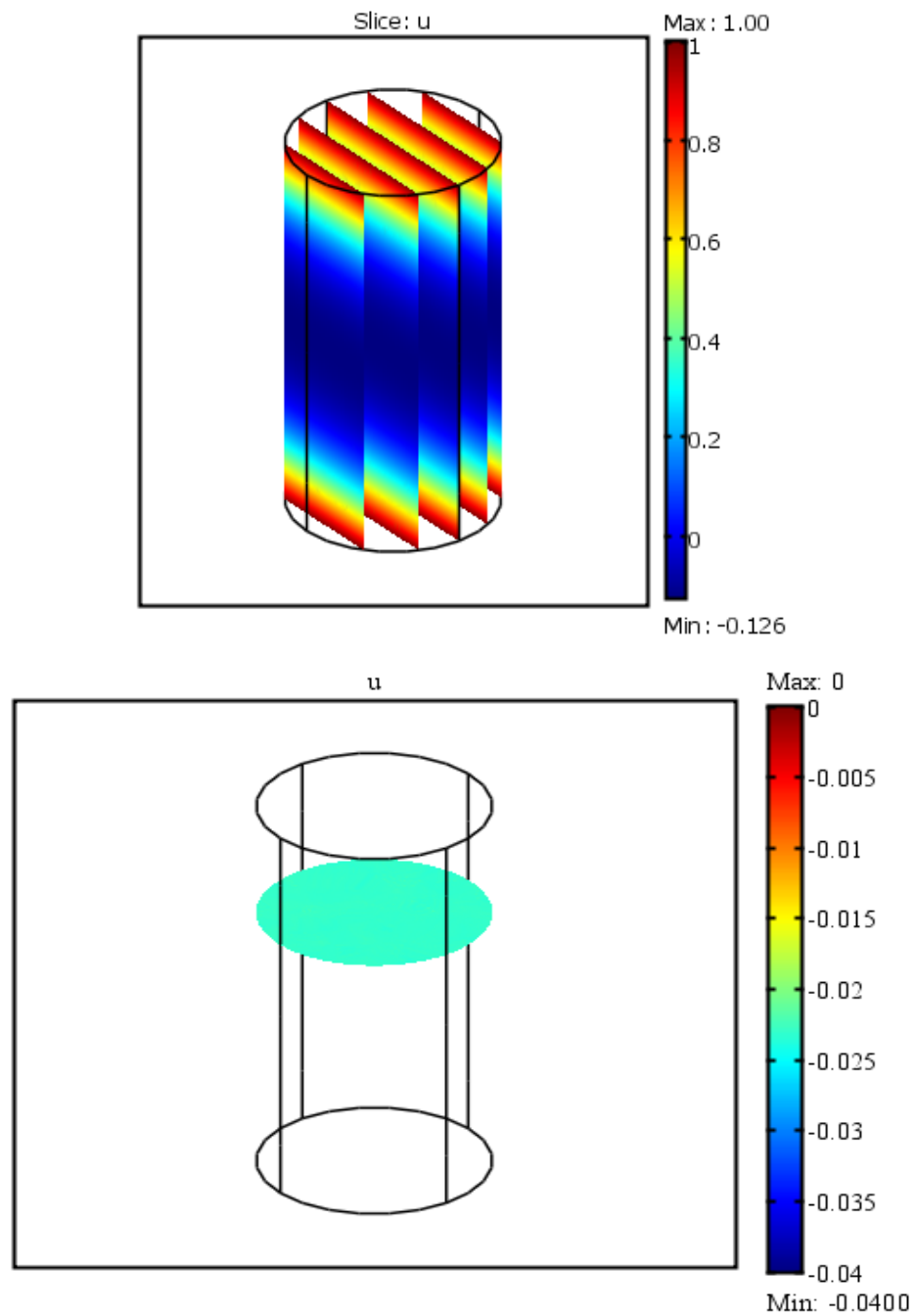


Figure 3-2. COMSOL Numerical result of the 1D diffusion model. The pressure decreases systematically and symmetrically starting from the two open ends (Top). Because the medium is homogeneous, there is no cross flow in the radial direction and the pressure is always constant in the radial plane (Bottom). The model has 500 mD permeability and 20% porosity.

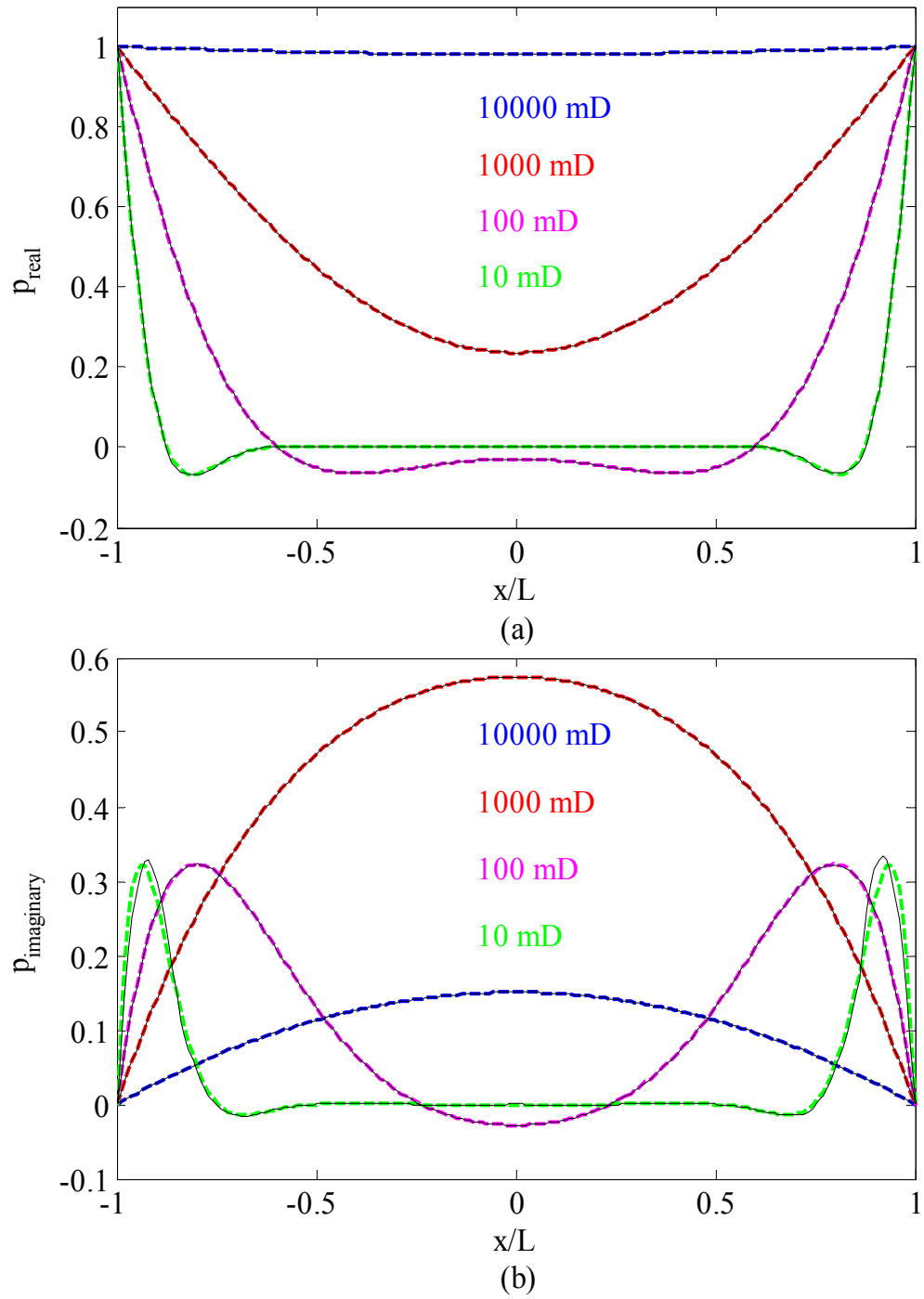


Figure 3-3. Comparison of the diffusion pressure given by the 1D analytical model and numeric simulation. (a): Real part. (b): Imaginary part. The porous medium has a length of L . Dashed lines: analytical results. Solid black lines: numerical results.

3.5 Comparison of compressibility

Following we will use Eqn (3.8) and (3.17) to calculate and compare the effective compressibility at different frequencies, permeabilities, and porosities.

3.5.1 Compressibility at varying frequency

From Eqn (3.8), for a porous sample with a known flow properties, κ_e changes with frequency. Figure 3-4 compare the real part and imaginary part of the analytical and numerical results of the change of κ_e with frequency for a set of materials with identical wet-frame bulk moduli and porosities (20%) but different permeabilities. The results given by the two different methods are comparable.

At low frequency, the fluid has more time to relieve the pressure gradient than at high frequency. Thus, more fluid can flow into or out of the sample during the half wave period. In other words, the material is “softer.” As frequency increases, the amount of dynamic flow decreases accordingly, and the material is “harder”; the κ_e decreases. The interesting observation is that a critical frequency exists, where the rate of the change of κ_e with frequency reaches a maximum. Below or above this critical frequency, the rates of the change of compressibility slow down systematically. The critical frequency corresponds to a state where the energy loss caused by dynamic flow reaches a maximum. In other words, the quality factor of the sample reaches a minimum. This frequency can be more easily determined on the imaginary plot of κ_e (Figure 3-4), where values of κ_e reaches negative maximum. The numerical characterization of this crossover frequency is described in Appendix F.

Because the three materials have identical porosity and wet-frame compressibility, those with relatively high permeability can deliver more fluid in a given time. Hence, the κ_e of these materials will be larger than that of those with relatively low permeability. When the loading frequency is extremely low, the κ_e profiles converge to a single value. Physically, this is because the wave period is so long that the pressure gradient is fully equilibrated and the compressibility is independent of permeability. In this state, the material is fully relaxed. On the other hand, when the frequency is extremely high, the pressure gradient across the

sample surface boundary remains, because the fluid has insufficient time to flow. Consequently, κ_e is independent of fluid flow and thus independent of permeability. The κ_e profiles for different permeabilities converge to another constant, κ_u . This high frequency strain-stress scenario is called the undrained state, where the fluid has too little time to flow. The corresponding compressibility is called the undrained wet-frame compressibility. Permeability has no effect in this extreme case.

Figure 3-5 compares the real and imaginary part of the analytical and numerical results of κ_e at varying frequency for a set of materials with identical wet-frame bulk moduli and permeabilities (500 mD), but different porosities. The results given by the two different methods agree well.

This study here was to investigate the superimposed effect of porosity on κ_e at different frequencies. Now, the permeability of the material is fixed but the storage is changing. The κ_e of the three cases all exhibit frequency dependence, but with different magnitudes. The materials with higher porosity behave softer than those with low porosity. This is generally true, because high porosity provides more storage space to hold more fluid; consequently, the κ_e will be larger. At high frequencies, the κ_e of each case decreases and the profiles converge to a constant when the frequency reaches the megahertz range. Physically, this is because the fluid is constrained in the pore structure and has no time to flow at high frequencies, thus the κ_e of the sample are mainly those of the wet frame. On the other hand, at the low frequency end, the κ_e profiles of the studied cases flatten out. However, the data curves corresponding to relatively low porosity reach a plateau faster than those with higher porosity. This is because low porosity requires less fluid to reach pressure equilibrium, or equivalently, the pressure gradients inside the low-porosity materials can be balanced more quickly. Consequently, the κ_e profiles of these low-porosity materials reach a plateau at a relatively higher frequency.

The imaginary part of the compressibility is related to attenuation, which is another research topic and not covered in details in this thesis. But clearly, the analytical and numerical results of compressibility can give us some qualitative insights about the attenuation of fluid saturated porous media at varying frequencies.

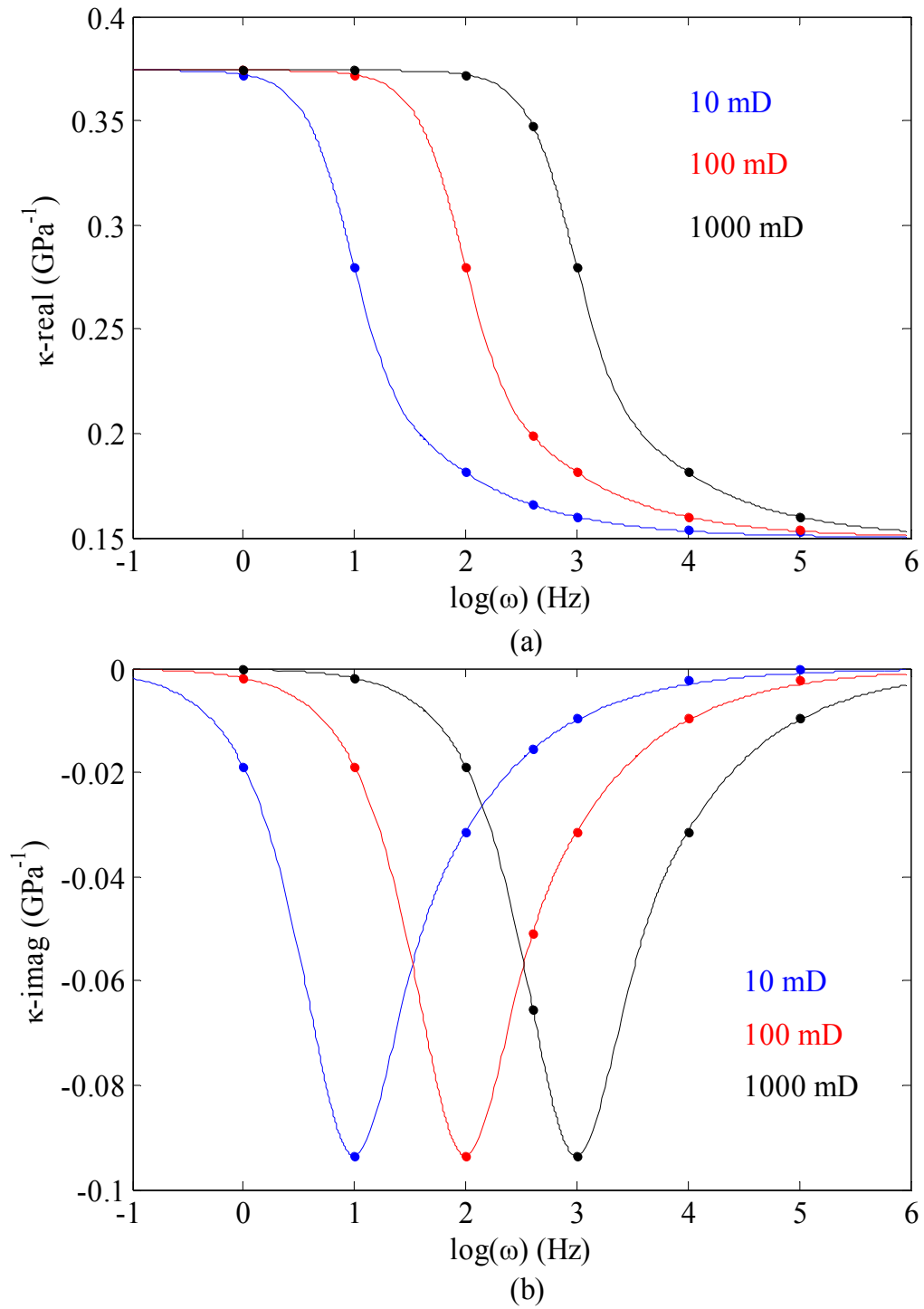


Figure 3-4. Effective compressibility at varying frequencies with permeability parameterized. (a): Real part. (b): Imaginary part. Solid lines are analytical results and colored dots are numerical results.

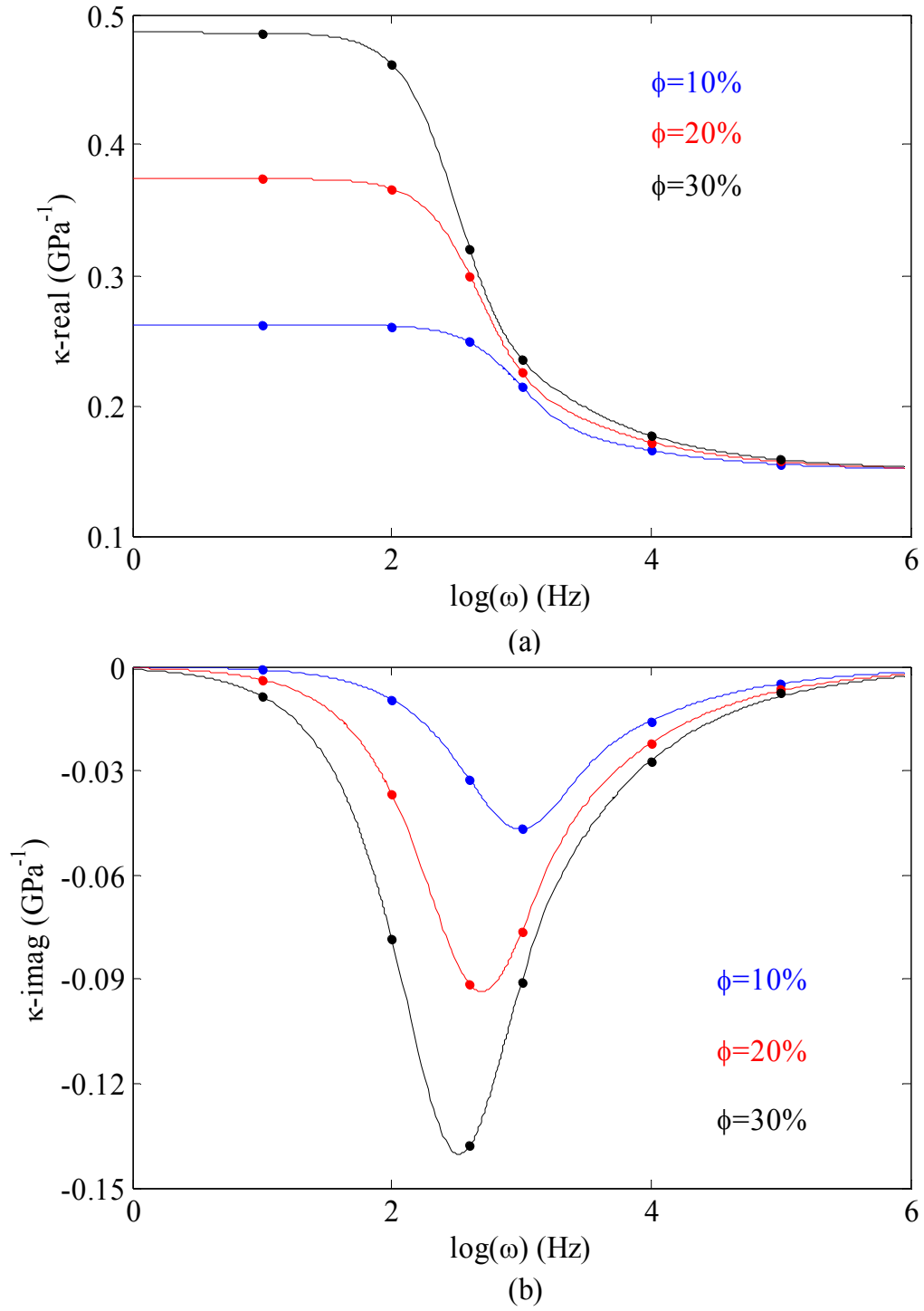


Figure 3-5. Effective compressibility at varying frequencies with porosity parameterized. (a): Real part. (b): Imaginary part. Solid lines are analytical results and colored dots are numerical results.

3.5.2 Compressibility at varying permeability

Permeability's influence on κ_e is the opposite of frequency's, as can be seen from the definition of diffusivity D in equation (3.3). In the following discussion, we investigate the change of κ_e with permeability for a set of materials with identical wet-frame bulk moduli but different porosities at 1000 Hz. Figure 3-6 compares the real and imaginary part of κ_e given by the analytical model, Eqn (3.8), and numerical simulation.

The results given by both methods show that as permeability increases, κ_e increases because high permeability means low flow resistance, and thus more fluid can participate in flow under a certain pressure gradient and time. However, the magnitude of the change of κ_e with permeability is different for each porosity case. The change of κ_e with high porosity is much greater at low porosities. This is not surprising, since a large pore space can accommodate more fluid under a given pressure gradient and flow time. At the high-permeability end, the κ_e profiles of all three cases flatten out, because the pore pressure is fully equilibrated. However, the profiles of those with low porosity reach a plateau faster than those with high porosity. This is because low porosity requires less fluid to balance the pressure gradient, or equivalently, these materials require less permeability to reach pressure equilibrium. Consequently, the low porosity materials can reach equilibrium faster in terms of permeability. On the other hand, at the low permeability end, the κ_e profiles of all three cases converge to a constant, the wet-frame compressibility, because the pressure gradient across the sample surface boundary persists.

The peak and trough on the imaginary part of κ_e (Figure 3-6) indicate the existence of a critical permeability under certain frequency. This critical permeability corresponds to a state where the energy loss caused by the dynamic flow reaches a maximum.

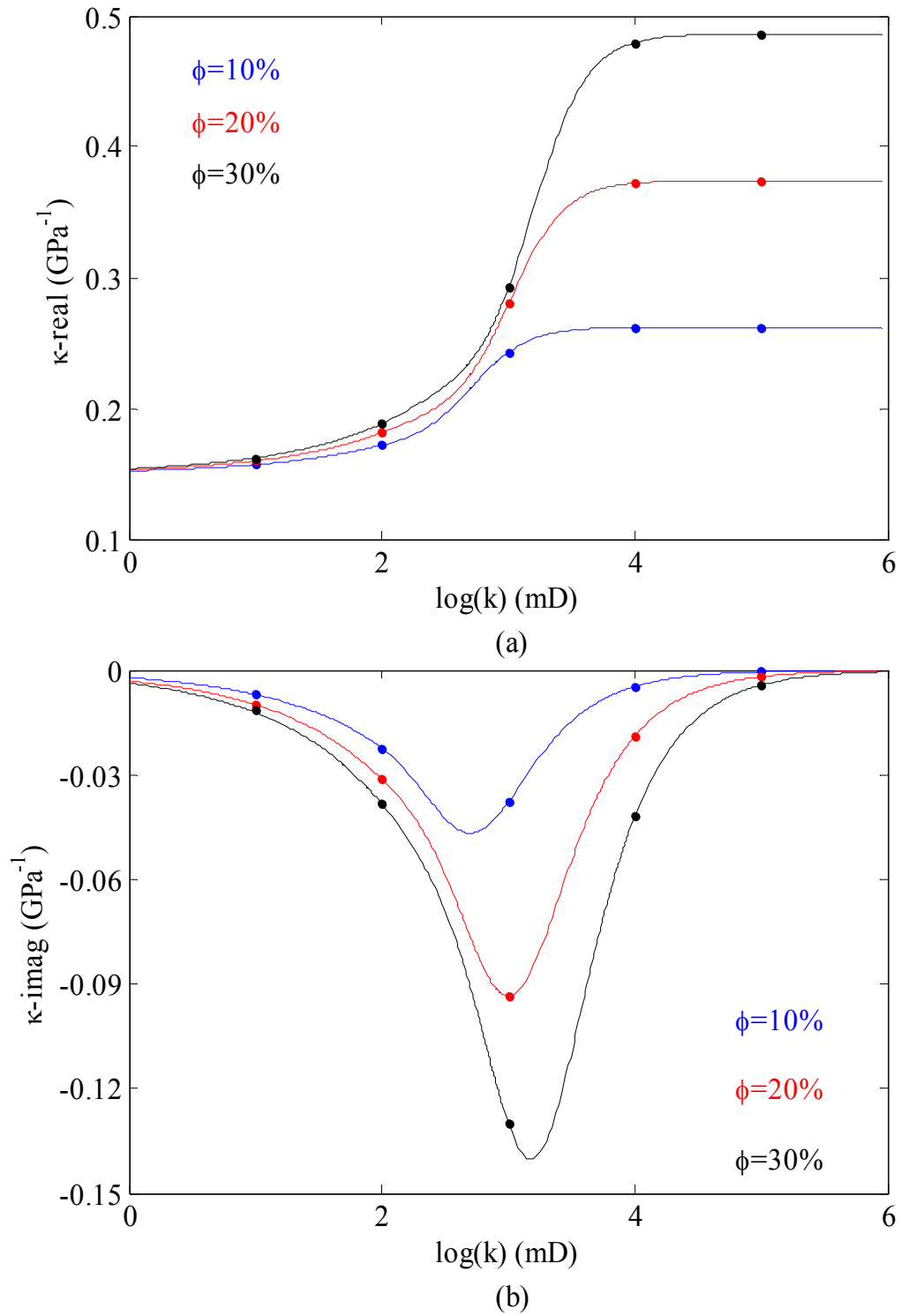


Figure 3-6. Effective compressibility at varying permeabilities with porosity parameterized. (a): Real part. (b): Imaginary part.

3.5.3 Compressibility at varying porosity

The following discussion reviews the porosity dependence of κ_e for three materials with identical wet-frame bulk moduli but varying permeability. Again, the simulation is at 1000 Hz. Figure 3-7 compares the real and imaginary part of κ_e given by the analytical model, Eqn (3.8), and the numerical results at varying porosity.

At the low-porosity end, the κ_e profiles converge systematically to a constant and show less permeability dependence. An explanation of this is that the pore space is so small that no fluid can flow into the pore structure, thus the fluid makes no contribution to the modulus of the porous medium. As porosity increases, more pore space becomes open to fluid; therefore, the material behaves softer. The effect of permeability is more evident as porosity increases. High permeability provides more chance for the fluid to get into the pore space, while low permeability limits the flow. Therefore, the κ_e show more permeability dependence at the high-porosity end.

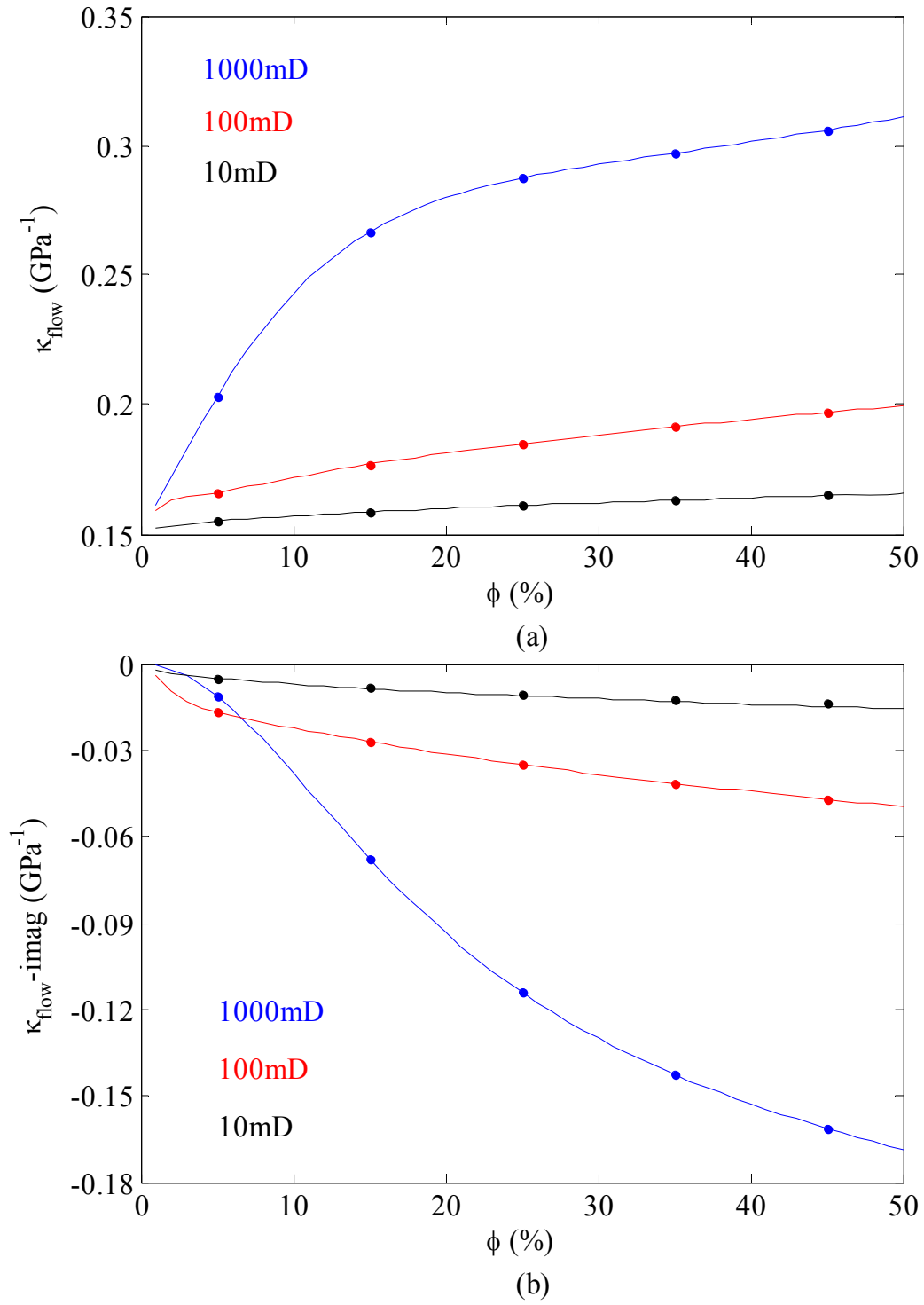


Figure 3-7. Effective compressibility versus porosity with permeability parameterized. (a): Real part. (b): Imaginary part.

3.6 Numerical simulation of 3D diffusion

This section focuses on the numerical simulation of 3D diffusion. The reason we are interested in 3D simulation is because firstly it could handle situations that are closer to the reality—most earth materials are heterogeneous and the diffusion inside is non-uniform, which is impossible for analytical study. Secondly, the 3D simulation provides the flexibility to handle materials with irregular shape, e.g., drilling cuttings or fragile earth materials which are difficult to core. The latter characteristic is particularly interesting to us.

The simulation object is a hybrid heterogeneous model—a cylindrical shell embedded with a cylindrical core (Figure 3-8). The shell and the core are both homogeneous and share identical rock properties beside permeability. Also, the two sections both have fully open surface boundaries. This configuration allows fluid freely diffuse into the medium along any direction. The pore pressure at the interface of the shell and core is continuous. The modeling parameters are listed in Table 3-2.

Table 3-2. Modeling parameters of finite element simulation

Length (mm)	Shell: 50
	Core: 20
Radius (mm)	Shell: 13
	Core: 8
Permeability (mD)	Shell: 1000 mD
	Core: 100 mD
Porosity (%)	20
Viscosity (cts)	5
Fluid compressibility (GPa ⁻¹)	1.1204
Frequency (Hz)	1000



Figure 3-8. 3D diffusion model. The sample surface of the model is fully open thus diffusion can be in any direction into the sample.

3.6.1 Numerical result of pressure distribution

The numerical results of the pressure field are shown in Figures 3-9 and 3-10. We also studied the pressure distribution along the axis of the model, as shown in Figure 3-11. From these figures we can clearly see that the pressure decreases gradually toward the center of the domain. However, we can easily identify the discontinuity of the pressure field at the interface of the shell and the core. The pattern of the pressure transition at the interface changed dramatically due to the discontinuity of permeability. The permeability in the core zone is 10 times less than that in the shell; therefore, the damping of the diffusion pressure inside the core is much larger than inside the shell region (Figure 3-11). Or in the other word, the resistance to the dynamic flow is much higher in the core than in the shell. This characteristic indicates that the dynamic flow inside the core contributes much less effect on the overall performance of the effective compressibility of the model, as compared to the effect caused by the dynamic flow inside the shell zone.

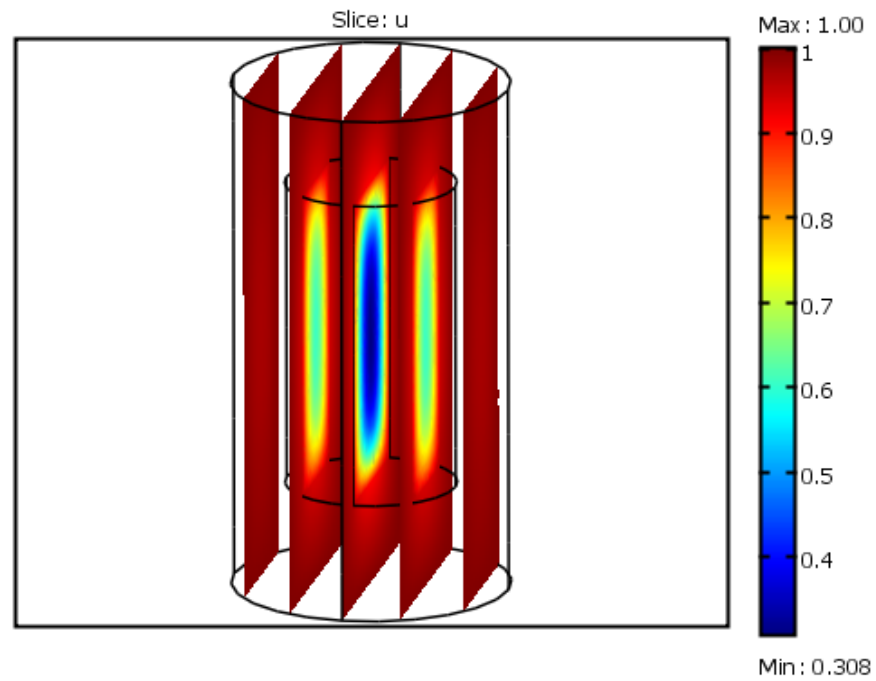


Figure 3-9. COMSOL Numerical results of diffusion pressure field.

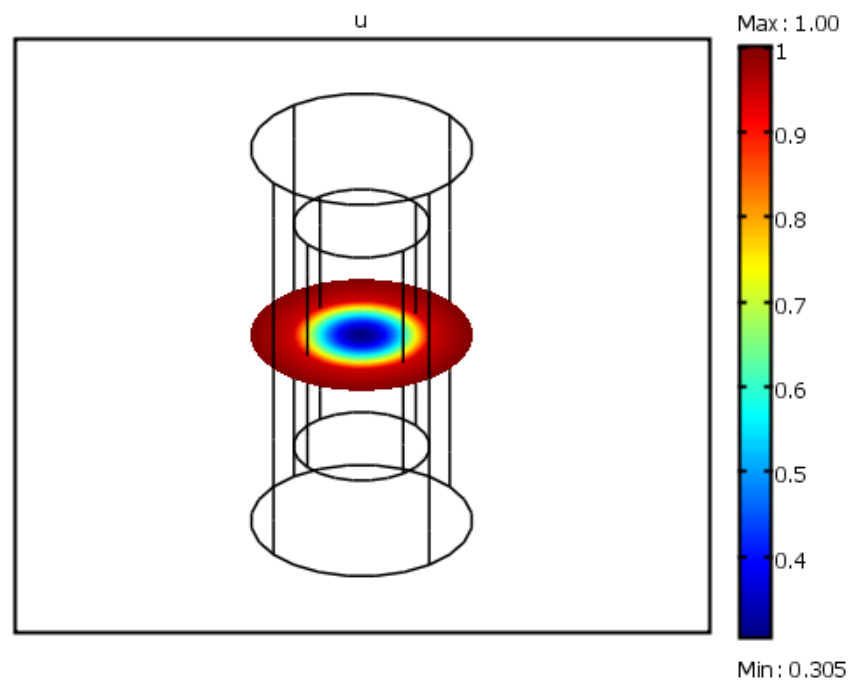


Figure 3-10. Diffusion pressure distribution in the central radial plane.

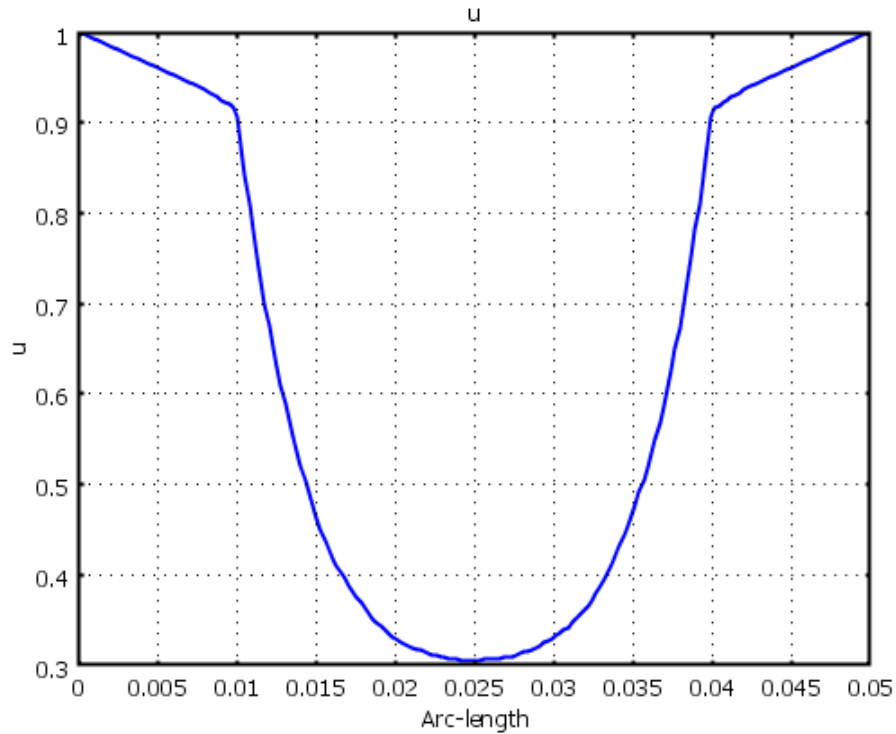


Figure 3-11. Diffusion pressure distribution along the axis of the model.

Compared to the simple 1D diffusion model (Figure 3-1), the diffusion in the 3D model is much more complicated and we currently do not have an analytical solution to describe the pressure distribution for this scenario. However, from the study of the 1D diffusion model we already know that the diffusion pressure profile given by the analytical solution and the numerical simulation are comparable. Meanwhile, from the study of the 1D model we know that the numerically estimated compressibility is comparable to that given by the analytical expression; hence we argue that we may extend the same approach to estimate the dynamic-flow component of compressibility in the 3D diffusion regime. Following we will estimate the effective compressibility with the numerical results of the diffusion pressure distribution. The fundamental rock properties are also conditioned with the same Berea sandstone as used in the 1D diffusion model in section 3.4.1.

3.6.2 Numerical result of compressibility at varying frequency

With the numerical diffusion pressure results, we calculated the κ_e at changing frequencies by using Eqn (3.17). Two different permeability combinations inside the shell and core are studied with the permeability ratio being maintained at 10. Case 1: the permeability in the shell and core are 1000 mD and 100 mD, respectively; Case 2: the permeability in the shell and core are 100 mD and 10 mD respectively. The results are plotted in Figure 3-12. Clearly, the high permeability combination yields larger compressibility. This trend agrees with the 1D diffusion model (Figure 3-5). The trough on the imaginary part of κ_e indicates the existence of a critical frequency at where the energy loss caused by the dynamic flow reaches a maximum.

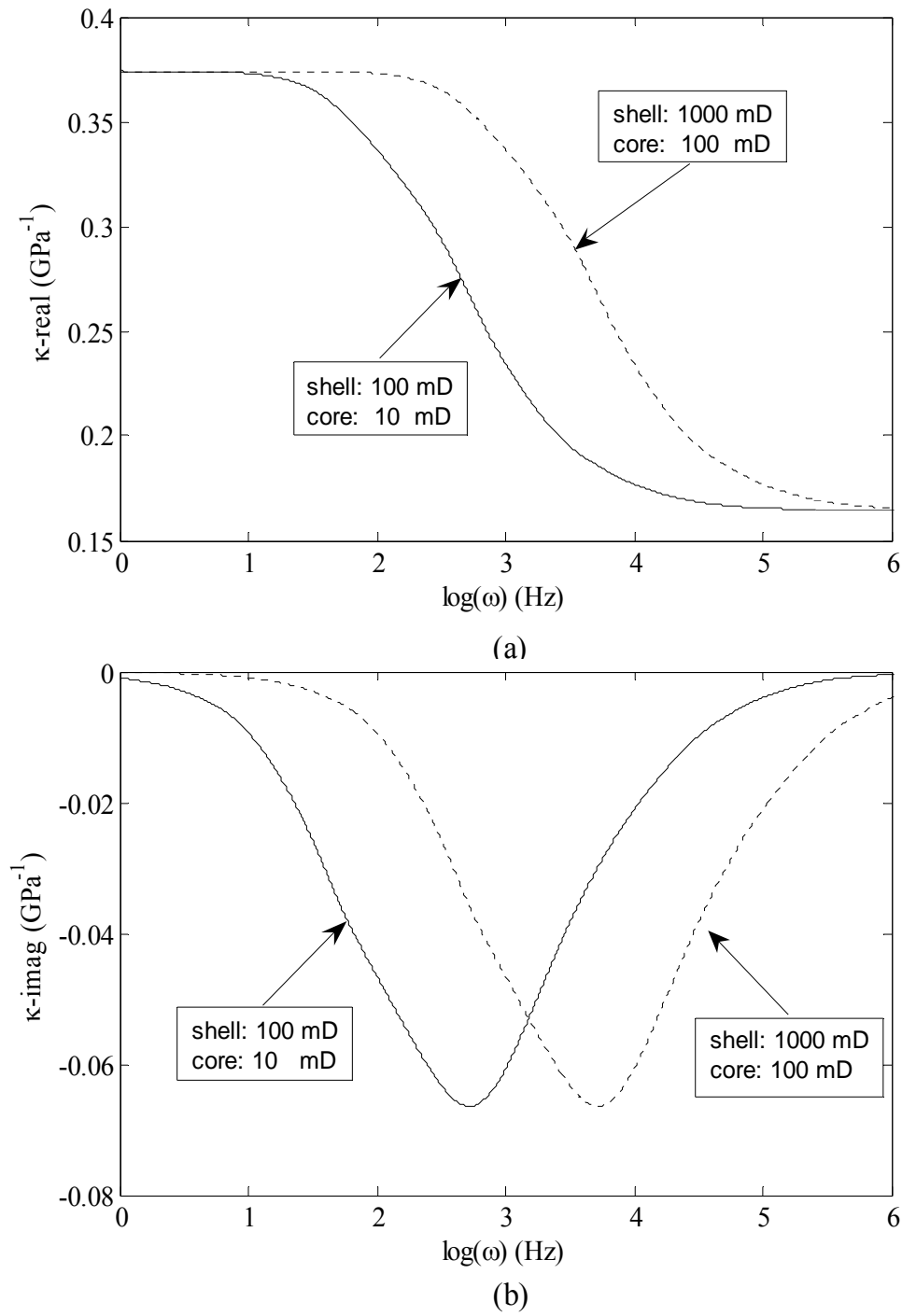


Figure 3-12. Effective compressibility versus frequency with permeability parameterized. (a): Real part; (b): Imaginary part.

3.7 Conclusions

An effective compressibility model was derived based upon a dynamic diffusion process. The model estimates the effective compressibility of fluid-saturated porous materials under a condition of dynamic fluid-loading, which mimics the interaction between the fluid and the solid skeleton in DARS measurements on permeable samples.

The effective compressibility given by the dynamic model contains information about the loading frequency, the permeability and porosity of the tested medium, and the viscosity of the fluid inside the pore space. Therefore, the analysis of the effective modulus provides us a way to estimate the permeability of the materials. It might also be possible to investigate the fluid type inside the pore space by analyzing the viscosity from the diffusivity; the permeability and porosity of the medium of course should be known in this case.

According to the effective compressibility model, the loading frequency and diffusivity of the porous sample jointly control the total amount of free moving fluid driven by the periodically changing pressure. At low frequency and high diffusivity, the pressure gradient across the sample surface boundary has time to equilibrate, and the porous medium shows maximum softness. On the other hand, at high frequency and low diffusivity, the pressure difference has less time and high flow resistance; therefore, the porous samples cannot equalize pressure variations and therefore demonstrate maximum stiffness.

A crossover frequency exists at which the change of effective compressibility with frequency reaches a maximum. Beyond or below this crossover frequency, the rate of change of compressibility with frequency slows down gradually and reaches plateaus at both the high-frequency and low-frequency ends. This crossover frequency corresponds to a state at which the energy loss caused by dynamic flow reaches maximum. In other words, the quality factor of the sample reaches a minimum.

We applied COMSOL, a finite-element tool, to study the diffusion in a cylindrical object with finite length. Two different scenarios: 1D homogeneous diffusion and 3D heterogeneous diffusion, were studied.

We compared the diffusion pressure given by the numerical simulation with that given by analytical solutions for the 1D diffusion model. The results agree well.

We numerically estimated the dynamic-flow contribution to compressibility for the 1D model and compared the result with that given by an analytical solution. The results are

comparable. We argued that we might extend the numerical approach to estimate the dynamic-flow component of compressibility for more complicated 3D diffusion problem, for which we do not have explicit analytical solutions.

Chapter 4

Comparison of laboratory and analytical results

4.1 Summary

In Chapter 3 I derived an analytical compressibility model based upon the concept of dynamic diffusion. In the model, the effective compressibility of the porous medium is a function of the loading frequency, the viscosity of the loading fluid, and most importantly, the porosity and permeability of the sample. In this chapter, I estimate the compressibility of seventeen rock samples (sixteen real and one synthetic) with DARS, and compare it with the effective compressibility calculated with the analytical model. The results of the two different approaches show reasonable agreement. This proves that the fluid and solid interaction in DARS measurement is a dynamic diffusion process.

4.2 Experimental procedure

The acoustic and flow properties of the seventeen experimental samples are listed in Table 4-1. The dimensions and corresponding measurement errors of the seventeen rocks are listed in Table 4-2. The porosity spans a range from near zero for granite and coal to 38% for a synthetic rock, and the permeability covers a range from less than 1 mD for the granite and coal to over 10 Darcy for several Berea sandstones. One of the samples is a synthetic rock.

Table 4-1. Physical properties of seventeen rock samples. The samples were 100% saturated.

	k_{gas} (mD)	ϕ (%)	ρ (kg/m ³)	v_p (m/s)	v_s (m/s)	Description
VIF02	12808	38.33	1947	2397	1380	Synthetic
NIV45	8056	31.65	2099	3128	1811	Nivelsteiner
SSB7	2748	28.56	2109	3416	2010	Berea sandstone
SSF2	2669	26.78	2176	2915	1337	Coarse sandstone
QUE10	2441	22.20	2263	3053	1736	Unknown sandstone
SSG1	1862	24.29	2227	3226	1551	Unknown sandstone
BEN28	1149	24.13	2232	3574	2131	Benheimer sandstone
SSA4	362	20.80	2277	3186	1920	Berea sandstone
BIP14	315	20.41	2312	3099	1794	Berea sandstone
BIN21	212	19.92	2317	3145	1801	Berea sandstone
YB3	182	18.94	2285	3410	1955	Berea sandstone
FEL37	9	22.67	2256	3383	1967	Felser
CAS17	5	19.54	2314	3261	1900	Castlegate
Chalk3	1.1	28.30	2184	3505	2013	Chalk
COL25	0.8	11.44	2462	3657	2157	Colton
SSC5	0.7	11.75	2425	3665	2114	Boise
UNK51	0.2	15.76	2390	3930	2379	Unknown sandstone

Table 4-2. Dimensions of seventeen rock samples.

	L (in)	Error in L (%)	D (in)	Error in D (%)	V_s (in ³)	Error in V_s (%)
VIF02	1.4656	±0.078	0.9772	±0.611	1.0992	±1.305
NIV45	1.4628	±0.170	0.9840	±0.072	1.1124	±0.314
SSB7	1.4846	±0.130	0.9962	±0.056	1.1572	±0.242
SSF2	1.4842	±0.130	0.9950	±0.008	1.1541	±0.146
QUE10	1.4594	±0.281	0.9826	±0.357	1.1067	±0.998
SSG1	1.4888	±0.100	0.9976	±0.055	1.1637	±0.210
BEN28	1.4678	±0.148	0.9852	±0.111	1.1189	±0.371
SSA4	1.4927	±0.385	0.9959	±0.113	1.1627	±0.612
BIP14	1.4646	±0.394	0.9922	±0.297	1.1324	±0.992
BIN21	1.4650	±0.232	0.9792	±0.112	1.1032	±0.456
YB3	1.1674	±0.239	0.9846	±0.234	1.0051	±0.709
FEL37	1.4682	±0.163	0.9730	±0.126	1.0917	±0.415
CAS17	1.4822	±0.451	0.9782	±0.086	1.1139	±0.623
Chalk3	1.4784	±0.273	1.014	±0.283	1.2066	±0.841
COL25	1.4664	±0.375	0.9788	±0.086	1.1034	±0.547
SSC5	1.4814	±0.141	1.0002	±0.041	1.1636	±0.223
UNK51	1.4704	±0.218	0.9832	±0.046	1.1164	±0.310

4.2.1 Sample preparation

All samples studied in this thesis are prepared with a nominal diameter of 1 inch and cut to a nominal length close to 1.5 inches. The plugs were rinsed, dried at ambient temperature for one day, oven dried at 85 °C for two days, and then allowed to cool to room temperature in a desiccator.

Helium gas permeability, k_{gas} , was measured in a Hassler-type core holder at a confining pressure of 14 bars. The porosities were measured with a porosimeter. Densities were measured by the routine mass-to-bulk volume ratio. The wet densities were calculated based on the dry-frame density, density of the saturating fluid, and measured porosity.

Ultrasound p- and s-wave velocities were measured following the density, porosity and permeability measurements. All velocity measurements were at room temperature in a pressure vessel filled with hydraulic oil used as pressurizing fluid. Samples were jacketed by Tygon tubing. During measurement, a 0.5 bar confining pressure was applied to obtain a better sample-sensor coupling. Pore pressure was vented to the atmosphere so that the effective pressure was simply the confining pressure. Standard ultrasonic pulse transmission was used to measure dry velocity. After these routine velocity measurements, the samples were immersed in a tank filled with silicone oil (the same fluid as inside the acoustic resonator), and the pressure of the tank was decreased to 0.1 torr for 4 hours. This depressurization induces expansion of the gas bubbles trapped in the samples. Eventually, air escaped and fluid filled the pore space as the tank re-equilibrated to atmosphere pressure.

After these procedures, the samples were ready for drained and undrained DARS measurements. The details are discussed in the following sections.

4.2.2 Drained and undrained measurements

The terms “drained” and “undrained” in this thesis refer to the sample surface boundary conditions. In the drained condition, the sample has a (partially or fully) open flow surface boundary (Figure 4-1a, b); therefore, fluid can freely flow across the sample surface boundary during the DARS measurement.

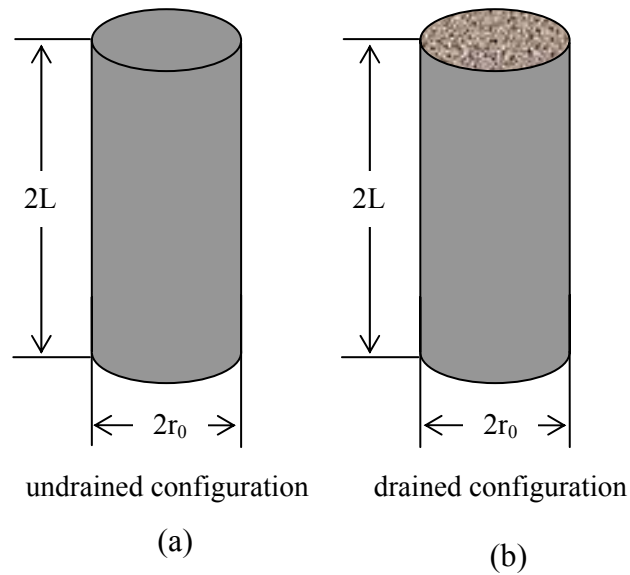


Figure 4-1. Sample surface boundary configuration. Undrained sample has a completely sealed surface. Drained sample has its cylindrical surface sealed and its two ends open. The sealing material is epoxy resin (Devcon® 5-Minute® Epoxy and 5-Minute® Epoxy Hardener).

Core boundary conditions are defined by the parts of the external surface of the core that were closed to flow. No-flow boundaries were established by sealing parts of the core surfaces with epoxy resin (Devcon® 5-Minute® Epoxy and 5-Minute® Epoxy Hardener). Many different scenarios could be modeled by sealing the sample surface in different patterns. The open boundary we used in this thesis is partially open, with the sample's cylindrical surface being sealed with a thin layer of epoxy resin, while the two ends of the sample are open. The purpose of this treatment is to constrain fluid flow across the open surface boundary of the tested sample to be one-dimensional; therefore, we can adopt a simple 1D diffusion model to characterize flow phenomena inside the porous medium. In the undrained condition, the sample surface is fully closed (Figure 4-1a) and no flow crosses the sample surface boundary.

The quality of the sealing has a significant effect on the measurement result. To check the sealing, the sealed sample was tested under 800mTorr vacuum for half an hour. If no air bubble came out of the sample, the sealing was recognized as successful. Otherwise, the

sample surface was sanded and resealed with epoxy, and the test was repeated until sealing was successful.

The undrained measurement yields the wet-frame compressibility, κ_u , which is required for the application of the effective compressibility model, Eqn (3.8).

4.3 Data preparation

Our current focus is to study the compressibility of porous materials. As discussed in Chapter 2, the frequency shift with the sample at the center of the cavity is dominated by the contrast between the compressibility of the sample and that of the background fluid. Therefore, I need only two resonance frequencies, one of the empty cavity (no sample inside the cavity) and the other of the sample-loaded cavity (with the sample centered in the cavity) to quantify the compressibility of the sample. Experimentally, the empty-cavity resonance frequency was measured immediately after each sample-loaded measurement in order to minimize the frequency drift caused by temperature variation during the two consecutive measurements. To control measurement noise and to best locate the resonant frequency, we apply Lorentzian curve fitting procedure (Appendix B) to each of the two recorded frequency spectra and the fitting yields an optimal estimation of the peak resonance frequency. The frequency estimates of the seventeen rock samples from DARS drained and undrained measurements are listed in Table 4-3. It is clear that the resonance frequency of sample-loaded system always increases under the influence of each sample, but the magnitude of the increase depends on the sample properties. The small fluctuations of the empty-cavity resonance frequency are due to changes in room temperature and perhaps dissolved air in the silicone oil.

Following I will focus on the calculation of the effective compressibility.

Table 4-3. Frequency results of 17 rocks from DARS drained and undrained measurements.

	Undrained measurement		Drained measurement	
	ω_s (Hz)	ω_0 (Hz)	ω_s (Hz)	ω_0 (Hz)
VIF02	1089.5983	1082.4637	1090.5889	1082.856
NIV45	1089.5234	1083.1594	1091.1631	1083.1514
SSB7	1090.7406	1083.3589	1091.1609	1082.6344
SSF2	1084.9336	1078.0831	1090.1965	1082.1418
QUE10	1090.3247	1083.1368	1091.2809	1083.2379
SSG1	1085.491	1077.9221	1091.0662	1082.6286
BEN28	1090.6803	1083.1057	1091.2637	1083.0845
SSA4	1091.5514	1083.5217	1091.94325	1083.5874
BIP14	1090.946	1083.1287	1090.5595	1082.4083
BIN21	1090.9691	1083.1470	1091.4831	1083.5668
YB3	1089.3033	1082.9981	1090.126	1083.6428
FEL37	1090.738	1083.0991	1090.2905	1082.5209
CAS17	1090.5049	1082.489	1091.1439	1083.2061
Chalk3	1089.215	1080.1171	1091.8126	1082.6832
COL25	1091.5138	1083.3612	1090.7236	1082.601
SSC5	1088.618	1080.038	1091.4486	1082.834
UNK51	1091.2826	1083.1217	1091.2826	1083.1217

4.4 DARS estimated compressibility

To estimate the compressibility of the seventeen rock samples by utilizing DARS frequency results (Table 4-3), we will use equations (2.7),

$$\kappa_s = A\xi\kappa_f + \kappa_f .$$

In the two equations, κ_f is 1.1205 GPa^{-1} calculated from the fluid's density (918 kg/m^3) and velocity (986 m/s) at 20°C . Coefficient A is -0.5951 , quantified by using the 1.5 inches in length and 1 inch in diameter aluminum sample (details see Chapter 2, section 2.6). The perturbation parameter ξ of each sample is calculated from

$$\xi = \frac{(\omega_s^2 - \omega_0^2)}{\omega_0^2} \left(\frac{V_c}{V_s} \right),$$

where ω_s and ω_0 are the resonance frequencies of the sample-loaded and empty-cavity cavity, respectively; V_s is the sample volume calculated from the diameter and length of each relevant sample; V_c is the volume of the acoustic resonator and is equal to 113.22 in^3 .

Using these parameters A , κ_f and ξ , we calculated the drained and undrained compressibility of the seventeen samples. To differentiate the results, the drained compressibility is defined as κ_d , while the corresponding undrained compressibility is defined as κ_u . The results are summarized in Table 4-4.

The difference between the drained and undrained compressibility is the dynamic flow contribution to compressibility and we will compare this quantity with the analytical results of dynamic flow component in the following section.

Table 4-4. Compressibility of 17 rocks from DARS drained and undrained measurements.

	κ_u (GPa ⁻¹)	Uncertainty in κ_u	κ_d (GPa ⁻¹)	Uncertainty in κ_d
VIF02	0.1179	±2.51%	0.4160	±2.88%
NIV45	0.1224	±1.37%	0.3227	±1.75%
SSB7	0.0986	±1.39%	0.2307	±2.24%
SSF2	0.1547	±1.25%	0.2968	±1.49%
QUE10	0.1061	±4.84%	0.2144	±5.39%
SSG1	0.1121	±0.79%	0.2176	±2.36%
BEN28	0.0997	±2.11%	0.1759	±3.69%
SSA4	0.1278	±3.52%	0.1666	±5.40%
BIP14	0.1172	±4.84%	0.1667	±7.45%
BIN21	0.1205	±3.15%	0.1409	±5.60%
YB3	0.1038	±1.77%	0.1410	±7.75%
FEL37	0.1385	±3.44%	0.1441	±4.86%
CAS17	0.1214	±6.00%	0.1256	±7.57%
Chalk3	0.0515	±1.34%	0.0548	±17.87%
COL25	0.0925	±12.18%	0.0895	±9.03%
SSC5	0.0868	±4.59%	0.0885	±5.78%
UNK51	0.0993	±5.20%	0.1002	±6.01%

4.5 Compressibility calculated from the analytical model

According to the analytical model of effective compressibility, Eqn (3.8),

$$\kappa_e = \kappa_u + \frac{\phi \kappa_f}{\alpha L} \frac{e^{2\alpha L} - 1}{e^{2\alpha L} + 1}, \quad \alpha = \sqrt{\frac{i\omega}{D}} = \sqrt{\frac{i\omega \phi \eta \kappa_f}{k}}$$

the effective compressibility of a fluid-saturated porous material under periodic fluid loading is simply the superposition of the wet-frame compressibility, κ_u , and a dynamic flow contribution of compressibility. To assist the following discussion, we assign a parameter, κ_{flow} , to represent the dynamic flow component of compressibility,

$$\kappa_{flow} = \frac{\phi \kappa_f}{\alpha L} \frac{e^{2\alpha L} - 1}{e^{2\alpha L} + 1}, \quad \alpha = \sqrt{\frac{i\omega}{D}} = \sqrt{\frac{i\omega \phi \eta \kappa_f}{k}}.$$

Therefore, to calculate the effective compressibility of each tested sample, we need κ_u and κ_{flow} of the sample. The quantification of κ_u has been discussed in section 4.4 and the results of the seventeen samples are listed in Table 4-4. We thus only need to estimate κ_{flow} , which can be simply calculated by using the viscosity and compressibility of the pore fluid, and porosity and permeability of each tested sample. The viscosity and compressibility of the pore fluid are constant and given, which are 5 cs and 1.1203 GPa⁻¹, respectively. The flow properties of the tested samples have been determined from the rock-physics measurements (Table 4-1). Using these parameters, we calculated the κ_{flow} , and κ_e of the seventeen samples. The results are listed in Table 4-5.

So far we have estimated the κ_u and κ_d of the seventeen samples from their DARS measurements and calculated their κ_{flow} , and κ_e by using their flow properties. Following we will compare and interpret these results.

Table 4-5. Compressibility of 17 rocks estimated from the analytical model.

	κ_{flow} (GPa ⁻¹)	κ_e (GPa ⁻¹)
VIF02	0.4124	0.5303
NIV45	0.3425	0.4648
SSB7	0.2558	0.3545
SSF2	0.2431	0.3978
QUE10	0.2104	0.3164
SSG1	0.1963	0.3085
BEN28	0.1470	0.2467
SSA4	0.0584	0.1862
BIP14	0.0547	0.1719
BIN21	0.0440	0.1645
YB3	0.0500	0.1538
FEL37	0.0098	0.1483
CAS17	0.0067	0.1281
Chalk3	0.0038	0.0553
COL25	0.0019	0.0944
SSC5	0.0021	0.0889
UNK51	0.0026	0.1018

4.6 Results analysis and discussion

4.6.1 Comparison of drained and undrained results

As discussed in section 4.2.2, the drained samples have partially opened surface while the undrained ones have completely closed surface which blocks the dynamic flow across the surface boundary. Clearly, the undrained samples will be less compressible than the drained ones because the irreducible pore fluid serves as a stiffer in the undrained samples.

We compared the drained and undrained compressibility of the seventeen samples by crossplot the data in Figure 4-2. The results verify our expectation that the undrained samples have smaller compressibility than the drained ones. An interesting observation is that the

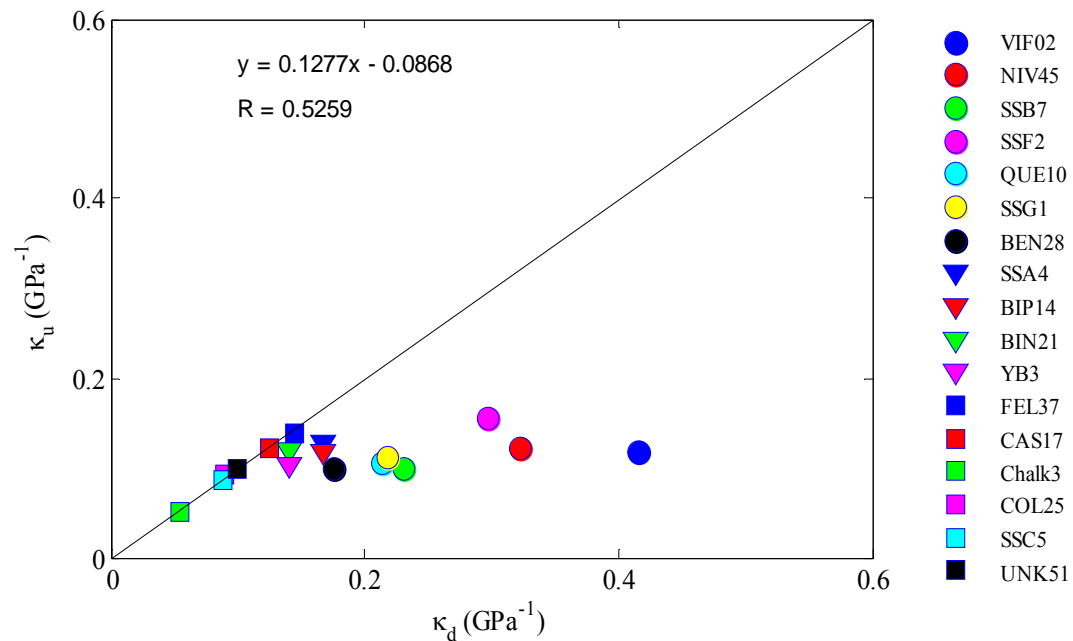


Figure 4-2. Comparison of compressibilities of 17 tested samples estimated by drained and undrained DARS measurements. Circles, triangles and squares identify high, intermediate and low permeability respectively.

magnitude of the difference in the two compressibilities shows permeability dependency. For instance, for low permeability materials, e.g., CAS17, SSC5, and UNK51, the difference is less than 3%. On the other hand, for the high permeability materials, e.g., VIF02, NIV45 or

SSB7, the drained compressibility could be 2 to 3 times larger than the undrained values. The reason is because, for high permeability materials, more fluid could flow in and out the pore space to release the pressure gradient; for low permeability materials, however, the flow is constrained by the permeability and only limited amount of fluid is allowed to move freely. Therefore, the dynamic flow contribution on compressibility has less effect on the overall compressibility for low permeability materials as compared to high permeability materials.

4.6.2 Comparison of analytical and experimental results

We estimated the dynamic flow contribution to compressibilities from DARS drained and undrained measurement and compared these results with those calculated from the compressibility model by cross-plot the data in Figure 4-3. To our surprise, the analytical

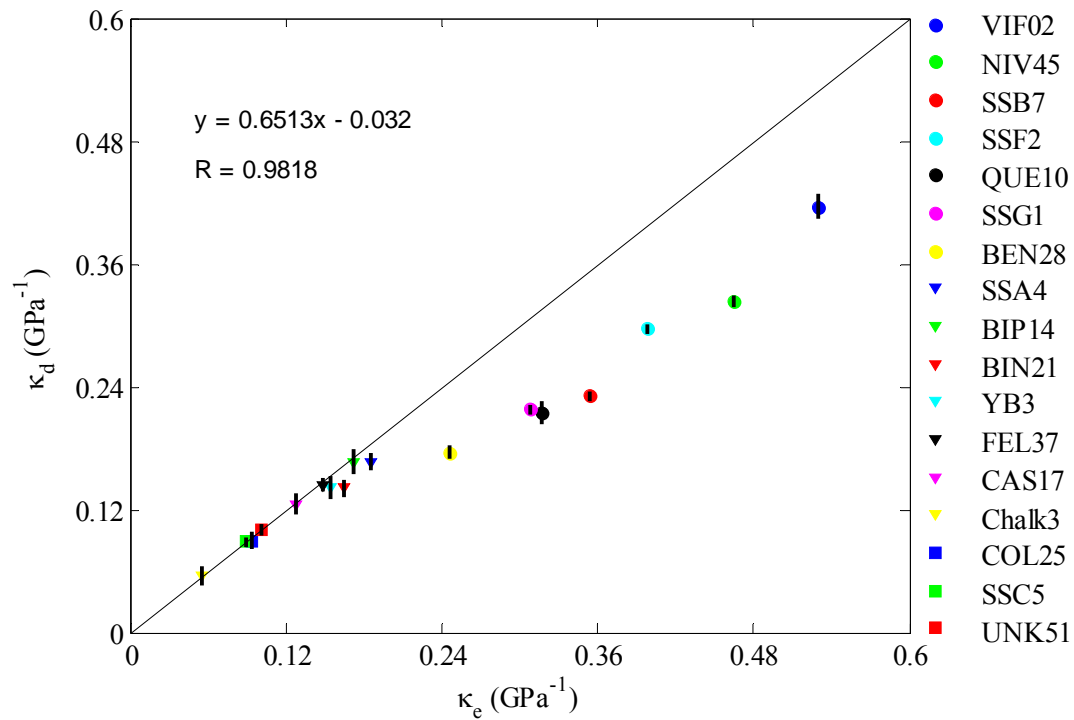


Figure 4-3. Comparison of compressibilities estimated by drained DARS and calculated by the analytical model without correction. Circles, triangles and squares identify high, intermediate and low permeability respectively. The short vertical bars crossing the data points represent the uncertainty in DARS compressibility estimates.

results didn't match with the experimental data, except for several samples with extremely low permeability, e.g., chalk5, SSC5 and UNK51. The data points of most of the samples deviate systematically from a 45° line through the origin. This shows that the analytical effective-compressibility model overestimates the measured compressibility of the tested samples.

I checked the acoustic amplitude spectrum of the porous materials and the reference sample, and found that the peak amplitude of the porous materials is dramatically different from that of the reference sample (Figure 4-4), particularly for those samples with relatively

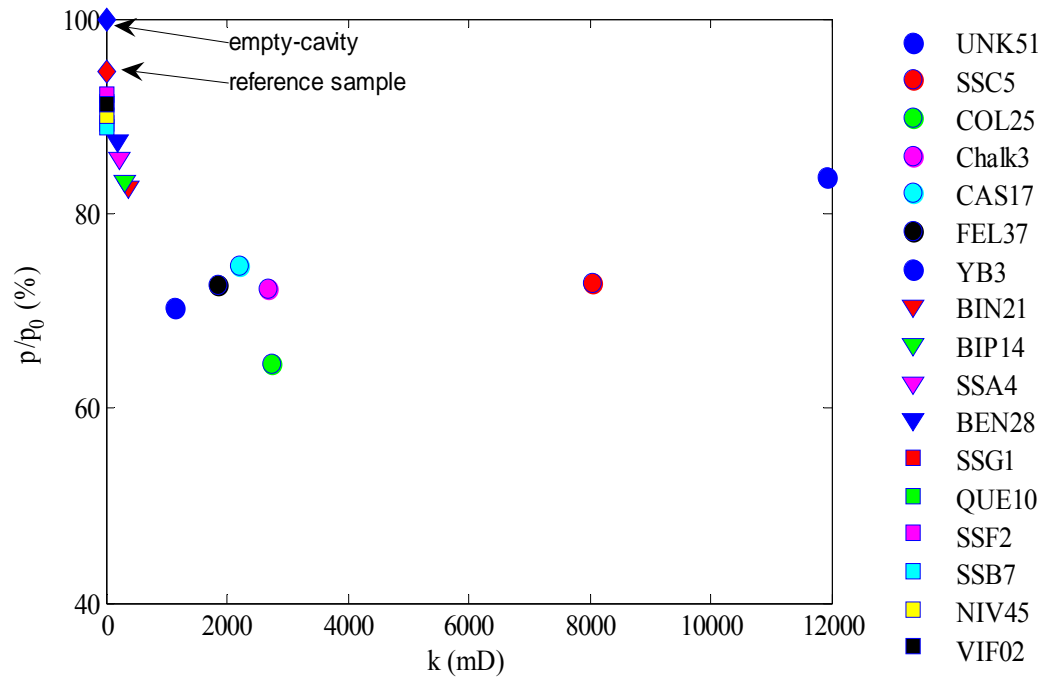


Figure 4-4. Ratio of acoustic pressure amplitude of DARS sample-loaded cavity and empty cavity. The value of the reference aluminum is much higher than that of highly permeable rocks. This difference should be considered in the analytical compressibility model.

high permeability; their peak amplitude is much lower than that of the reference sample and even far smaller than that of the empty-cavity response. The pressure decrement is caused by the losing fluid into the porous medium from inside the cavity. From the derivation of the effective compressibility model, Eqn (3.8), we know that the dynamic flow component of compressibility of the tested sample is a linear function of the amount of free-flowing fluid across the sample's open surface boundary. However, in the derivation of equation (3.8), we

assumed that the acoustic pressure is constant over different samples (p_0 is constant in Eqn (3.4)). This assumption certainly results in an overestimation of the amount of fluid flow, and thus of the compressibility of the tested sample. To correct this overestimation, the pressure amplitude p_0 used in Eqn (3.4) should be replaced with the real pressure amplitude in the measurement of each tested sample. Therefore, the modified diffusion pressure profile will be,

$$p(x) = \frac{e^{\alpha L}}{1 + e^{\alpha L}} (e^{\alpha x} + e^{-\alpha x}) p_0' . \quad (4.1)$$

Parameter p_0' in Eqn (4.1) will be the real pressure amplitude from DARS measurement for each corresponding sample.

From Figure 4-4 we have already that the pressure amplitude in the measurement of the tested samples and the reference sample is different; hence a coefficient C , the ratio of the pressure amplitudes of the cavity with the tested sample and with the reference sample, should be used in the dynamic flow component of compressibility in Eqn (3.8). The modified effective compressibility will be

$$\kappa_{flow} = C \frac{\phi \kappa_f}{\alpha L} \frac{e^{2\alpha L} - 1}{e^{2\alpha L} + 1}, \quad \alpha = \sqrt{\frac{i\omega}{D}} = \sqrt{\frac{i\omega \phi \eta \kappa_f}{k}} . \quad (4.2)$$

The compressibilities of the seventeen samples were recalculated with the modified compressibility model (Table 4-6). Figure 4-5 compares the new results with those given by DARS measurement. The cross-plotted data points of both the compressibilities now all fall along the 45° straight line through the origin. The correlation of the two observations is 0.998, and the standard deviation of the data points from the 45-degree line is 0.0042. This result strongly indicates that 1) the results given by two different methods are comparable; 2) more importantly, the interaction between the solid and fluid phase in the drained DARS measurement of porous samples is proven to be a dynamic diffusion process; 3) the replacement of the pressure amplitude in the effective compressibility model with that from the real measurement is essential for interpreting the DARS measurement results. From the effective compressibility model we can see that the compressibility measured by DARS for porous materials is not the routine compressibility we quantified using other techniques, such

as the ultrasonic method. The compressibility given by DARS measurement is the superposition of the wet-frame compressibility of the tested sample and a pseudo-compressibility contributed by a portion of free-flowing fluid moving across the open surface boundary of the sample.

The fluctuation of the data points around the 45-degree line in Figure 4-5 may be attributed to errors in sample volume measurement, temperature variation during DARS measurement, the sample heterogeneity, or effects of the epoxy sealing layer.

Table 4-6. Compressibility of drained samples given by DARS and the analytical compressibility model.

	κ_d (GPa ⁻¹)	κ_e (GPa ⁻¹)	$\frac{\kappa_e - \kappa_d}{\kappa_e}$
VIF02	0.4160	0.4134	-0.6%
NIV45	0.3227	0.3240	0.4%
SSB7	0.2307	0.2305	-0.1%
SSF2	0.2968	0.2950	-0.6%
QUE10	0.2144	0.2194	2.3%
SSG1	0.2176	0.2270	4.1%
BEN28	0.1759	0.1801	2.3%
SSA4	0.1666	0.1669	0.2%
BIP14	0.1667	0.1635	-2%
BIN21	0.1409	0.1527	7.7%
YB3	0.1410	0.1422	0.9%
FEL37	0.1441	0.1463	1.5%
CAS17	0.1256	0.1268	1%
Chalk3	0.0548	0.0547	-0.1%
COL25	0.0895	0.0941	4.9%
SSC5	0.0885	0.0887	0.2%
UNK51	0.1002	0.1012	1%

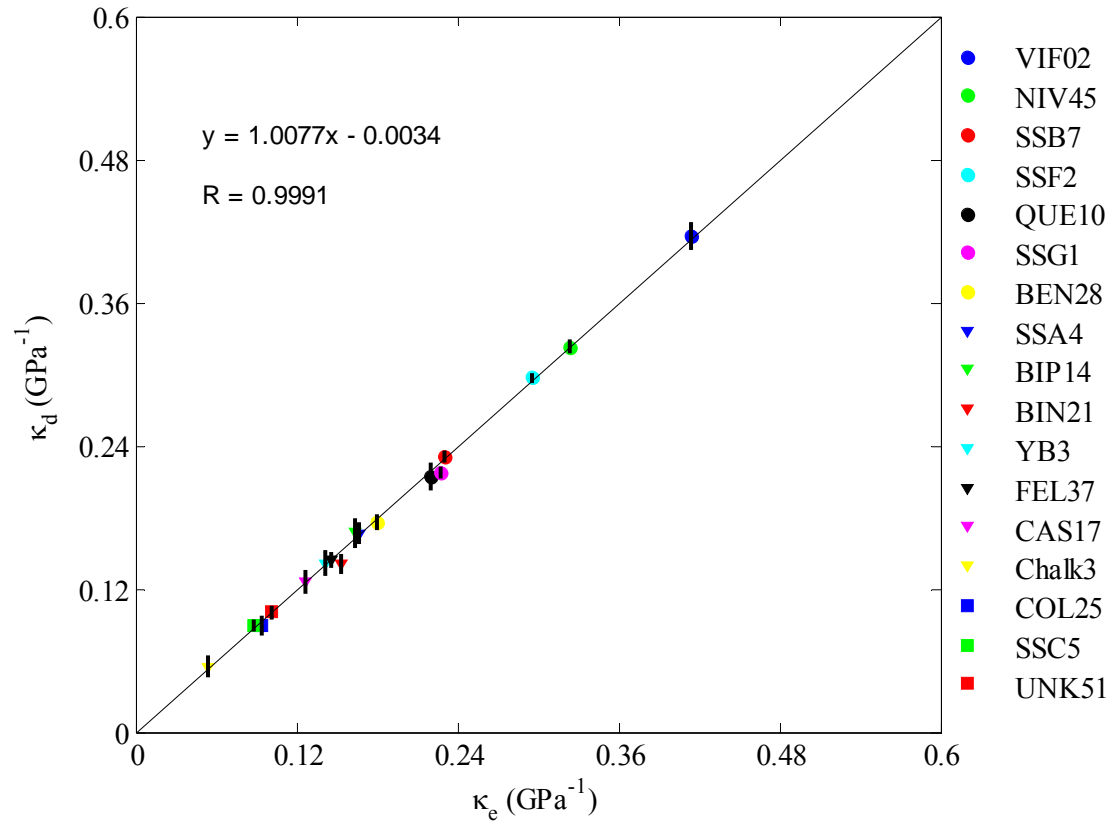


Figure 4-5. Comparison of compressibilities of 17 tested samples estimated by drained DARS and calculated by the modified analytical model after correction. The short vertical bars crossing the data points represent the uncertainty range in DARS compressibility estimates.

4.7 Conclusions

Sixteen real rocks and one synthetic rock were measured with DARS in drained and undrained conditions. The effective compressibilities of the samples were estimated from the DARS measurements. The drained measurements yield larger estimates for compressibility as compared to undrained measurements due to dynamic flow effect.

We also calculated the compressibility of the seventeen samples using the analytical model. The compressibility results given by the two different methods agree well, indicating that the interaction between the fluid and the solid matrix in DARS measurements of permeable samples is a dynamic diffusion process.

The acoustic and flow properties of the seventeen tested samples cover a rather large range, indicating that the analytical compressibility model can be applied generally to all porous media.

Diffusivity is the dominant controlling factor on the effective compressibility of the porous materials measured by DARS. Therefore, the analysis of the effective compressibility provides us a way to estimate the permeability of the materials, as will be shown in Chapter 5.

Chapter 5

Applications of DARS

5.1 Summary

The previous chapters have validated the DARS concept and the reliability of DARS compressibility measurements and have investigated the mechanism of the diffusive interaction in DARS measurement of porous media. This chapter focuses on applications of the DARS method. Anticipated applications include estimating the permeability of porous media, estimating the wet-frame compressibility (reciprocal of bulk modulus) in Gassmann's equation.

5.2 Permeability estimation

In Chapter 3 we discussed that the effective compressibility of fluid-saturated porous materials under dynamic fluid loading situation is a function of frequency, pore fluid viscosity, and more importantly, the porosity and permeability of the medium. In Chapter 4, we compared the DARS-quantified compressibilities of 17 samples with those given by the analytical compressibility model and found that the results agreed well. We thus argued that the drained compressibility measured by DARS is the result of a dynamic diffusion process. Therefore, we proposed to combine the analytical model for compressibility with DARS compressibility to determine the flow properties of porous media.

From Eqn (3.8),

$$\kappa_e = \kappa_u + \frac{\phi \kappa_f}{\alpha L} \frac{e^{2\alpha L} - 1}{e^{2\alpha L} + 1}, \quad \alpha = \sqrt{\frac{i\omega}{D}} = \sqrt{\frac{i\omega \phi \eta \kappa_f}{k}},$$

the effective compressibility of a cylindrical porous sample with open ends (drained) is a function of seven free parameters: wet-frame compressibility of the sample (reciprocal of the Gassmann wet frame bulk modulus), the scaling coefficient C , frequency, the viscosity and compressibility of the pore fluid, the porosity and permeability of the medium, and the length of the tested sample. Among the seven parameters, the frequency is known from the drained measurement of the tested sample; the coefficient C can be obtained by taking the ratio of the pressure amplitudes of the tested sample and the reference sample; the viscosity and compressibility of the pore fluid is constant and given; the wet-frame compressibility of the sample can be measured in the undrained sample; and the length of the sample can be measured with a caliper. The only possible unknowns are porosity and permeability. Since porosity can be easily measured by the ratio of the weight difference between the dry and wet sample to the sample bulk volume, we hence assume that permeability is the only unknown parameter. We of course can measure permeability with other methods; however, we propose to use DARS measurement to estimate it.

It is difficult to get an explicit expression of permeability from Eqn (3.8); hence we relied on a numerical search (details reference Appendix G) for the optimal permeability by forcing the calculated compressibility from the analytical model to match that estimated by DARS.

The permeability obtained for the seventeen samples is listed in Table 5-1. We also measured the gas permeability of these samples by a direct gas injection measurement. We cross-plotted the permeability given by the two different approaches in Figure 5-1. The results are comparable for samples with intermediate value of permeability (from 10s mD to several Darcy). However, for those with extremely low (1 mD or less) or high permeability (beyond 10 Darcy), the results given by the two methods do not match well. The reason for the mismatch is that our current system is not sensitive to ultra-low and ultra-high permeabilities. In Chapter 3, section 3.5.2, we have discussed that the effective compressibility relies less and less on permeability when the permeability is extremely high or low (Figure 3-6). In high permeability materials, the conductivity of the pore space is so high that the pore fluid can be recognized as part of the DARS system and the pore pressure can simultaneously balance the

pressure change outside the material; hence the dynamic flow has less and less contribution to the effective compressibility within high permeability range. To extend DARS measurement into the high-permeability range, we may need to explore higher resonance modes, in which case the pore pressure cannot reach equilibration in a wave period and the compressibility will see more effect by the dynamic flow. On the other hand, in low permeability materials, the pore fluid is limited to flow to release the pressure gradient; hence the dynamic flow also has no contribution to the compressibility. In order to investigate low-permeability materials, we have to rely on a lower-frequency cavity and a possible approach is to build a long cavity or to use a lower-velocity fluid, which may provide frequencies at 10s or 100s Hz; this would push the permeability sensitivity below one milliDarcy.

Table 5-1. Permeability of 17 rocks given by drained DARS and measured by gas injection.

	k_{gas} (mD)	k_{DARS} (mD)	Uncertainty in k_{DARS}
VIF02	12809	9009	±21%
NIV45	8055	7240	±12.4%
SSB7	2747	2865	±4.7%
SSF2	2669	2762	±7.2%
QUE10	2194	1950	±5%
SSG1	1862	1659	±2.4%
BEN28	1149	1070	±4.3%
SSA4	361	335	±3.5%
BIP14	315	290	±3.2%
BIN21	212	206	±2.8%
YB3	181	170	±3.1%
FEL37	9	4.5	±9%
CAS17	5	3.1	±21.7%
Chalk3	1.08	1.12	±4%
COL25	0.7	0.05	±15.3%
SSC5	0.8	0.7	±6.7%
UNK51	0.9	0.2	±20%

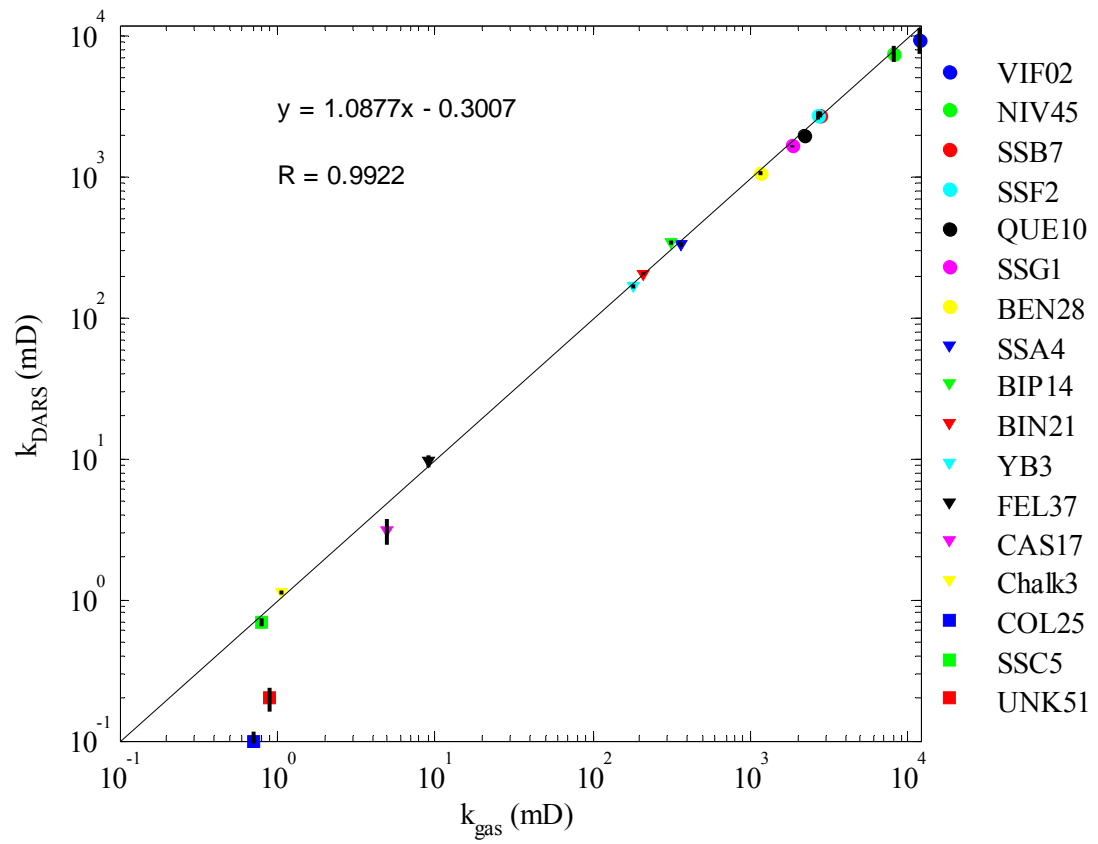


Figure 5-1. Comparison of permeabilities of 17 samples estimated from DARS drained measurement and measured by direct gas injection. The vertical black bars crossing the data points represent the error range in DARS permeability estimates. The short vertical bars crossing the data points represent the uncertainty range in DARS permeability estimates.

5.3 Estimating Gassmann wet frame compressibility

The presence of pore fluid complicates the seismic signature of earth materials. When a passing wave compresses a rock, the deformation in the pore space leads to pore-scale pressure gradients and subsequent pore fluid flow. Gassmann's equation provides a fast way to predict the effects of fluid saturation on the seismic properties of a porous medium (Gassmann, 1951; Wang, 2001; Han and Batzle, 2004). Gassmann's equation written in compressibility form is

$$\kappa_G = \kappa_s + \frac{\phi(\kappa_{dry} - \kappa_s)(\kappa_f - \kappa_s)}{\phi(\kappa_f - \kappa_s) + (\kappa_{dry} - \kappa_s)},$$

where κ_G and κ_{dry} are wet- and dry-frame bulk moduli, respectively, κ_s is the grain compressibility, κ_f is the compressibility of the pore fluid, and ϕ is the porosity.

Generally, Gassmann's equation is robust; however, the successful application of this equation is strictly subject to the following assumptions (Mavko, 1998): 1) the porous medium is homogeneous and isotropic, 2) all pores are interconnected and communicating, 3) the rock-fluid system under study is closed, 4) pore fluids are frictionless, and 5) the fluid-rock system is relaxed (there are no pressure gradients in the fluid phase). These strict requirements make the application of Gassmann equation questionable when we work with earth materials, especially at high frequency, because the complicated and heterogeneous constituents of earth materials often fail to satisfy these assumptions.

The routine way to quantify the Gassmann wet frame bulk modulus is through low frequency strain-stress measurements (Hofmann, 2000; 2005) by taking the bulk volume normalized ratio of the volume strain to the corresponding stress. The challenges associated with such experiments are: 1) the surface boundary of the tested materials has to be well sealed and any leaking of pore fluid will significantly bias the results; 2) the tested sample has to be well machined in a particular shape (cylinder or cubic depending on the experiment apparatus); 3) the tested sample should be strong enough to bear certain amount of strain and this requirement excludes fragile earth materials, e.g., coal, which is particular interesting to us. Due to these difficulties, we propose an alternative approach to quantify the wet-frame bulk modulus of porous media through a fast, indirect and nondestructive undrained measurement with our DARS system, which has no particular requirements on the sample

shape and strength. The advantage of the DARS undrained measurements is that it avoids the need for strict assumptions associated with the application of Gassmann's relation, and it does not require prior knowledge of the bulk moduli of minerals, information that frequently is not known for most earth materials. The details of the proposed approach are discussed in the following sections.

In Chapter 3 we derived an analytical model for the effective compressibility of a porous medium subject to cyclic fluid loading. The model includes a critical parameter, κ_u , the compressibility of the wet rock frame. The reciprocal of this compressibility yields a bulk modulus. In the derivation of the analytical model, the porous medium is fluid-saturated; this modulus is thus the property of the wet frame. In DARS experiments, this parameter is quantified by the measurement of the undrained or sealed sample. We believe that this parameter is the Gassmann wet-frame compressibility, or at least can be used to approximate that quantity, because our undrained measurement satisfies almost all of the major assumptions of Gassmann's equation. Our approach is not subject to the first two assumptions of Gassmann's theory, because it uses a direct measurement of the wet-frame bulk modulus, which is not limited to homogeneous and isotropic materials. The third assumption is automatically satisfied with our approach because our measurements are carried out in the undrained state. As for the 4th assumption, the fluid we currently use in DARS experiment is low-viscosity silicone oil, ($\eta = 5 \text{ cts}$); practically, this can be considered frictionless.

Only the fifth assumption may be problematic: that the rock-fluid system is relaxed and has no pressure gradients in the fluid phase. However, we believe that our approach can still satisfy this requirement because of two facts: 1) the frequency in DARS measurement is at about 1000 Hz (and can be even lower), and 2) the dimension of our samples is far less than one wavelength in the experiment. In our current experiment, the typical working frequency is about 1080 Hz and the acoustic velocity of the fluid medium is about 986 m/sec. Therefore, the wavelength is close to 92 cm. On the other hand, the typical length and radius of our tested samples are about 4 cm and 1.25 cm, respectively, far less than the wavelength. Hence, we argue that the pore fluid has sufficient time to flow to equilibrate the wave-induced pressure gradients inside the pore spaces during a wave period. The pressure drop across the sample surface boundary, however, still remains and can never reach equilibration. This argument is valid for most the earth materials.

We tested 17 samples with DARS and quantified their wet-frame compressibilities through undrained measurement; the results are listed in Table 5-2. We also calculated these

properties from ultrasonic p- and s-wave velocity measurements and density measurements of the saturated samples; the results are also listed in Table 5-2. The comparison of the compressibilities given by the two methods are shown in Figure 5-2. Clearly, the compressibility given by high-frequency ultrasonic measurements are much lower than those from low-frequency DARS measurements. The comparison here is only for reference, since Gassmann's equation can not be applied to the ultrasound frequency range, where the pore fluid has no time to flow and equilibrate the pore pressure gradients. In DARS undrained measurement, the pressure inside the pore space is equilibrated thus the undrained bulk modulus gives a better estimation of the Gassmann wet frame bulk modulus.

Table 5-2. Wet-frame compressibility of 17 rocks given by undrained DARS and derived from ultrasonic velocity measurement. The samples were 100% saturated.

	$\kappa_{\text{ultrasound}} \text{ (GPa}^{-1}\text{)}$	$\kappa_u \text{ (GPa}^{-1}\text{)}$	Uncertainty in κ_u
VIF02	0.16027	0.1179	$\pm 2.51\%$
NIV45	0.08803	0.1224	$\pm 1.37\%$
SSB7	0.07547	0.09861	$\pm 1.39\%$
SSF2	0.07519	0.15466	$\pm 1.25\%$
QUE10	0.08333	0.1061	$\pm 4.84\%$
SSG1	0.06283	0.11214	$\pm 0.79\%$
BEN28	0.06671	0.09969	$\pm 2.11\%$
SSA4	0.08396	0.12781	$\pm 3.52\%$
BIP14	0.08143	0.1172	$\pm 4.84\%$
BIN21	0.07758	0.12051	$\pm 3.15\%$
YB3	0.06698	0.10378	$\pm 1.77\%$
FEL37	0.07052	0.1385	$\pm 3.44\%$
CAS17	0.07424	0.12139	$\pm 6.00\%$
Chalk3	0.06653	0.05149	$\pm 1.34\%$
COL25	0.05666	0.09245	$\pm 12.18\%$
SSC5	0.05519	0.08676	$\pm 4.59\%$
UNK51	0.05297	0.09926	$\pm 5.20\%$

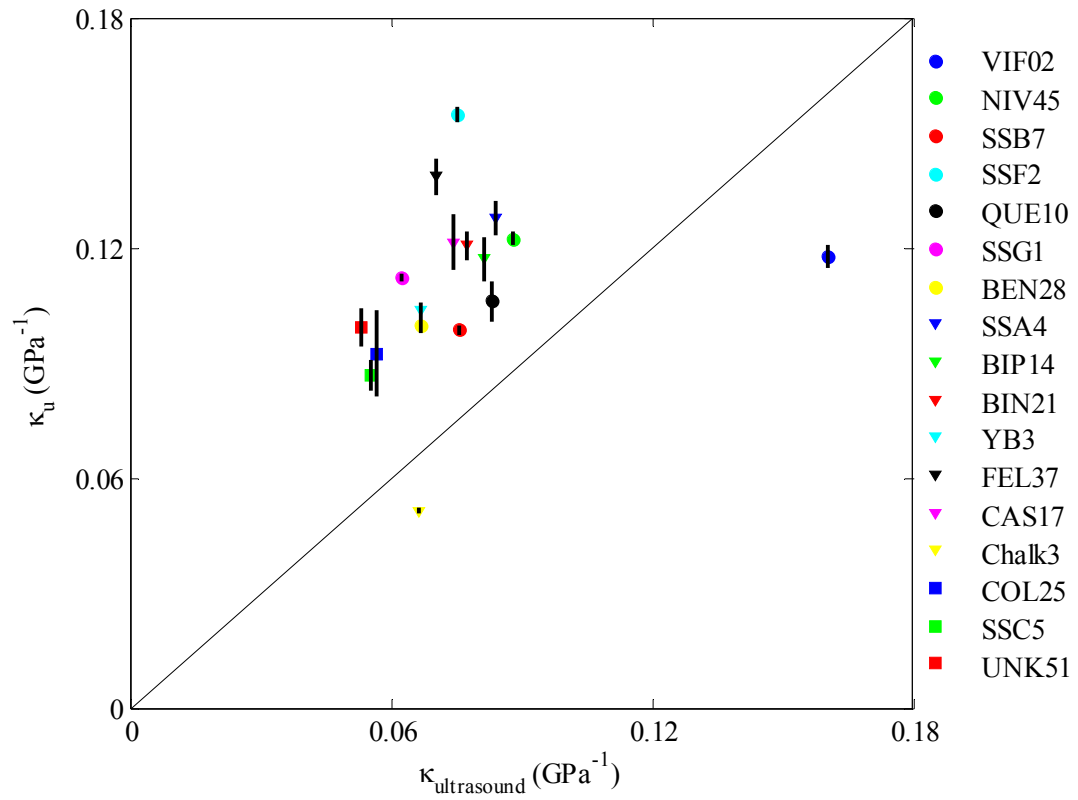


Figure 5-2. Comparison of wet-frame compressibilities of 17 samples estimated by DARS undrained measurement and derived from ultrasonic velocity measurement. The short vertical bars crossing the data points represent the uncertainty range in DARS permeability estimates.

5.4 Conclusions

The combination of DARS-quantified compressibility with the analytical effective compressibility model provides a way to estimate the permeability of porous materials. We estimate the permeability of the 17 tested samples and compare the estimated permeability with that given by a direct gas-injection measurement. The results agree well for the materials with intermediate permeabilities, e.g., 10 to several thousand mD.

The current DARS setup is not suited to estimate the permeability of rocks with extremely low or high permeability, for instance less than 10 mD or above 10,000 mD, because the compressibility estimated with the current system is insensitive to extremely low- or high-permeability samples. To extend our measurement to the low-permeability range, we need a lower-frequency cavity. On the other hand, to have a better study of highly permeable materials, we may need to explore multiple-resonance modes.

The current study on permeability estimation is limited to homogeneous materials. For heterogeneous materials this needs further study.

Gassmann's equation is frequently used in fluid substitution analysis to predict the wet-frame bulk moduli of earth materials; however, this equation is subject to strict assumptions which restrict its application to limited rock types. We propose an alternative approach to measure the wet-frame bulk modulus by undrained DARS measurement of fluid-saturated porous materials. Our approach is reasonable because it satisfies the major assumptions of Gassmann's equation.

We quantify the wet-frame bulk moduli of 17 samples using their undrained DARS measurement and compare the results with those derived by ultrasonic p- and s-wave velocity measurements and density measurements. Our results are much smaller than the ultrasound results, because in the ultrasonic measurement, the pore fluid has no time to flow, making the rock frame stiffer.

Chapter 6

Practical considerations

6.1 Summary

DARS measurement is subject to some sources of error that may affect its accuracy. This chapter summarizes the potential error sources, their effects, and possible ways to compensate for them.

In a numerical study of the affecting factors, the errors they produce in compressibility and bulk modulus estimates, the two dominant error sources were uncertainty in the sample volume and temperature drift during the DARS measurement. However, these two factors are controllable, and their effect can be reduced by adopting appropriate measurement tools. The other errors, which are related to the accuracy of the DARS instrument and DARS perturbation theory, are inevitable, but their effects are relatively small compared to the other two error sources.

6.2 Potential factors affecting DARS measurement

The key of DARS is that the acoustic pressure and velocity fields in the background fluid medium inside the cavity are assumed to remain unchanged by the interference of the reference sample and the studied samples. To fulfill these assumptions, these factors potentially affecting observations should be carefully considered: temperature variation, sample size, and sample shape. They are discussed below.

6.2.1 Temperature drift

Implicitly, the application of DARS assumes a constant working temperature for both the reference and the studied material, throughout the entire measurement process of each relevant sample. The potential influence of temperature variation stems from the difference in the acoustic velocity and density, and thus the compressibility of the background fluid, at different temperatures. Figures 6-1 and 6-2 demonstrate the temperature dependence of the acoustic velocity and density of the background fluid medium. Clearly, if the temperature is not well controlled, these changes in the acoustic velocity and density, and thus the compressibility of the fluid medium, will be propagated into the interpreted compressibility of

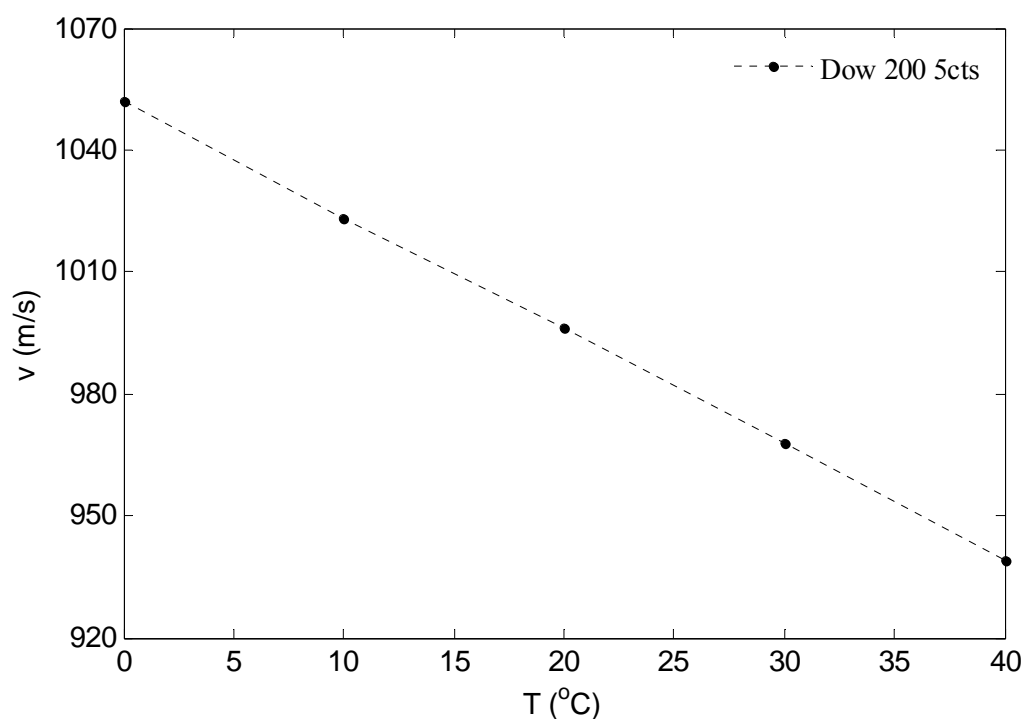


Figure 6-1. Acoustic velocity versus temperature for silicone oil.

the studied materials. The possible error contribution to the estimated compressibility of tested samples will be addressed in the following error analysis section (6.3.1).

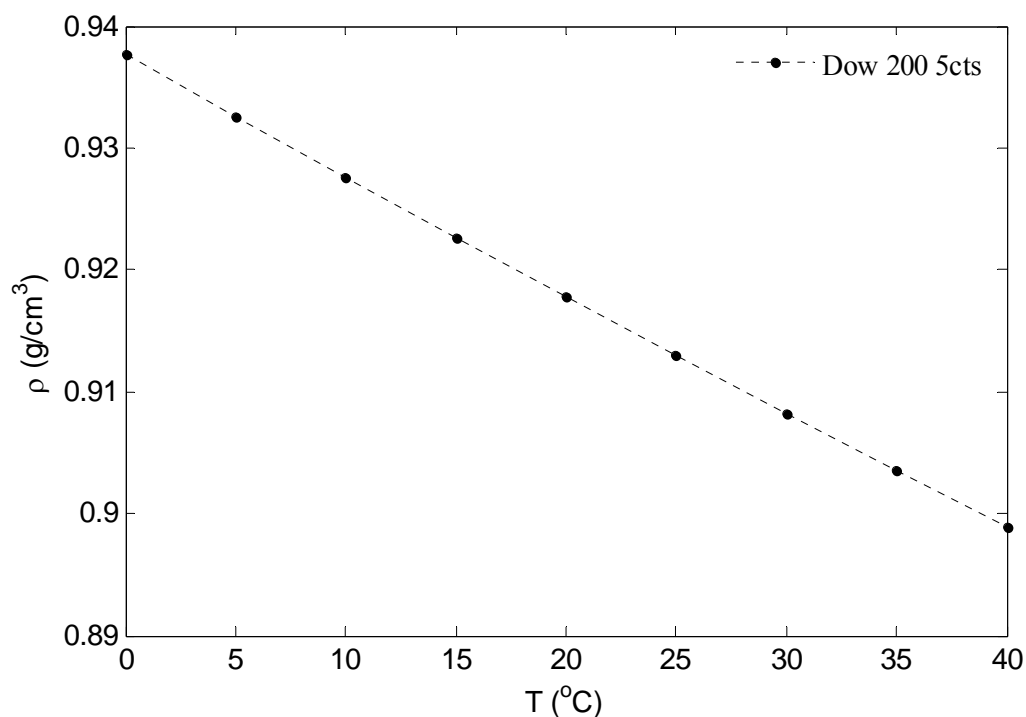


Figure 6-2. Density versus temperature for silicone oil.

6.2.2 Sample size

Sample volume has a first-order effect on DARS frequency observation; therefore, the size of the tested samples needs to be precisely measured. Moreover, the sample volume should be restricted to a limited range to satisfy the perturbation assumptions. Based upon our experience, a portion of 2-4% of the cavity volume is reasonable for the sample size. Too small a sample may result in a large reading error in the observation, while too large a sample may violate the perturbation assumption.

There are two sources for the possible effects of the sample volume: first, according to perturbation Eqn (2.3), the sample volume has an explicit first-order effect on the perturbation. Therefore, any uncertainties in the measurement of the sample size will go directly into the estimated compressibility of the studied materials. The second possible source of error is associated with the coefficient A in Eqn (2.3), which is a volume integral of the acoustic pressure over the sample body. The acoustic pressure inside a resonating cavity has a sinusoidal spatial distribution along the axis of the resonator, and thus over the sample body

located inside the cavity. In DARS, we assumed that the acoustic pressure distribution is unchanged between the reference sample and the studied sample. This assumption is sound if the size of the studied sample and that of the reference material are identical. However, if the sizes are mismatched, the acoustic pressure acting on different objects cannot be assumed to be equal. If it is erroneously assumed to be equal, the error will be transferred into the estimated compressibility of the studied sample through coefficient A .

The effect of the measurement uncertainty of sample volume will be discussed in Section 6.3.4.

6.2.3 Sample shape

From the perturbation theory, Eqn (2.3), the frequency shift is explicitly dependent on the volume of the sample rather than the shape. Therefore, we postulate that DARS is a potential way to evaluate the elastic properties of materials with irregular shapes, with the prerequisite that the sample volume can be accurately quantified, which in most cases is not a big challenge.

To verify the hypothesis, we tested two sets of standard materials, aluminum and Lucite. Each of the two sample sets had a total of twelve samples. Six of those had the same diameter (1.5") and various lengths (1.0", 1.2", 1.4", 1.6", 1.8", and 2.0"), and six had the same length (2.0") and various diameters (1.0", 1.1", 1.2", 1.3", 1.4", and 1.5"). The volume ratio of the samples to the cavity is in a range of 1.4-3.1%, which is acceptable for the perturbation assumption.

The cross-plot between the resonance modes, measured with the samples located at the center of the cavity, and the various sample volumes of the two sample sets is shown in Figure 6-3. A strong linear correlation exists for both materials. Moreover, the two linear trends intersect at the point where the sample volume is zero, and the corresponding resonance frequency is the empty cavity response. This behavior proves that, first, the perturbation is a function only of the volume of the sample (or, more precisely, the ratio of the sample's volume to that of the cavity) rather than being dependent on the sample's shape; second, the nonlinearity of the differential estimation caused by the discrepancy between the volume of the reference sample and that of the studied sample is not dramatic if the sample volume is controlled in a range of 2-4% of the cavity volume.

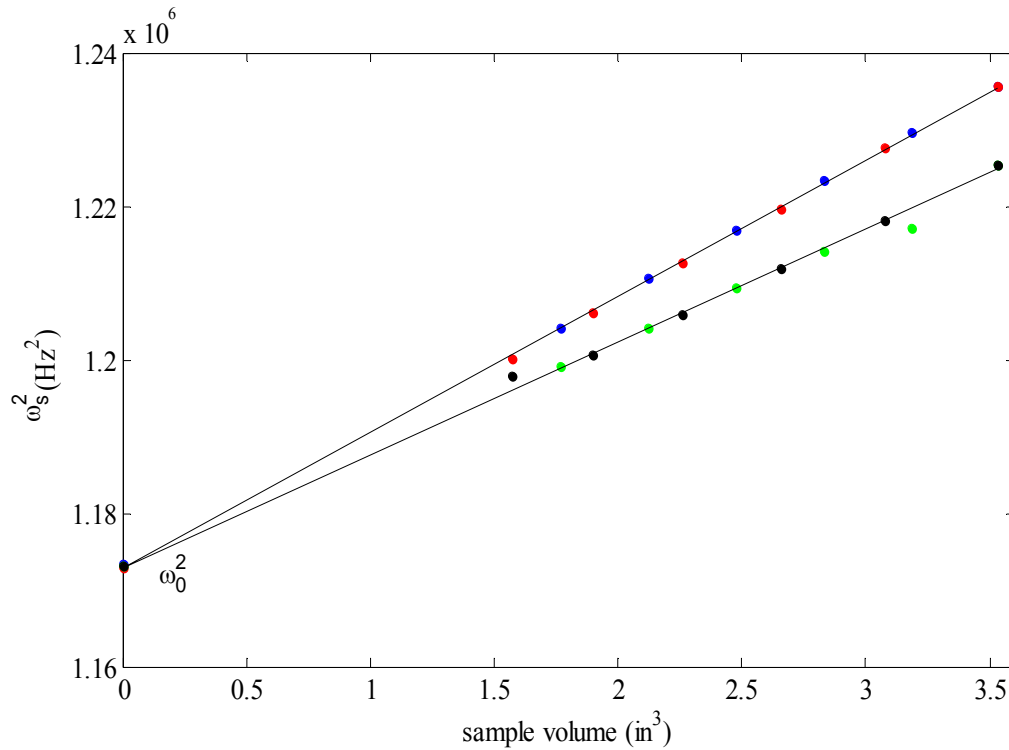


Figure 6-3. Frequency shift versus sample volume. DARS observation is insensitive to the sample's shape but sensitive to its volume.

Blue dots – Aluminum samples with 1.5" diameter but various lengths (1.0", 1.2", 1.4", 1.6", 1.8", and 2.0")

Red dots – Aluminum samples with 2.0" length but various diameters (1.0", 1.1", 1.2", 1.3", 1.4", and 1.5")

Green dots – Lucite samples with 1.5" diameter but various lengths (1.0", 1.2", 1.4", 1.6", 1.8", and 2.0")

Black dots – Lucite samples with 2.0" length but various diameters (1.0", 1.1", 1.2", 1.3", 1.4", and 1.5")

In Figure 6-3, for the data points of the samples with fixed diameter but varying lengths, small fluctuations around the trend line can be observed for both the aluminum and the Lucite sample sets, because the acoustic pressure distributed over the sample body is varying with length instead of being constant. The deviation is small and the assumption of constant pressure is reasonable for a first-order estimation. On the other hand, for the data points represent the results for the samples with fixed length but changing diameters, the results of both the aluminum and Lucite are well distributed along two straight lines, which

indicates that the pressure variation in the radial direction, a Bessel function, can be ignored, and that the error in the compressibility estimation thereby induced can also be ignored.

6.3 Error analysis

There are several possible error resources in DARS experiments and in the application of the perturbation theory. Some of the errors are inherent and inevitable, for instance the accuracy of the measurement instrument and the extent of the approximation in the perturbation theory. However, most of the errors are controllable or at least can be improved, e.g., errors caused by operator and observation error.

To gain insight into the possible errors within DARS and the way they affect the interpretation result, we need to slightly modify the perturbation equation. Recall the perturbation equation Eqn (2.3), at the center of the cavity,

$$\omega_s^2 - \omega_0^2 = -\omega_0^2 \left(\frac{V_s}{V_c} \right) \frac{\langle p \rangle^2}{\Lambda} \delta\kappa.$$

For the reference and tested samples, we can write two separate equations

$$\omega_s^2 - \omega_{0s}^2 = \omega_{0s}^2 \left(\frac{V_s}{V_c} \right) \frac{\langle p_s \rangle^2}{\Lambda_s} \frac{\kappa_s - \kappa_f}{\kappa_f}. \quad (6.1)$$

$$\omega_r^2 - \omega_{0r}^2 = -\omega_{0r}^2 \left(\frac{V_r}{V_c} \right) \frac{\langle p_r \rangle^2}{\Lambda_r} \frac{\kappa_r - \kappa_f}{\kappa_f}. \quad (6.2)$$

The sub-index s and r in Eqn (6.1) and (6.2) indicate the tested sample and reference sample, respectively; parameters ω_{0s} and ω_{0r} are the empty-cavity resonance frequency for the tested sample and reference sample, respectively.

Combining Eqn (6.1) and (6.2) we get,

$$\kappa_s = \left(\frac{\omega_s^2 - \omega_{0s}^2}{\omega_r^2 - \omega_{0r}^2} \right) \left(\frac{\omega_{0r}^2}{\omega_{0s}^2} \right) \left(\frac{\langle p_r \rangle^2}{\langle p_s \rangle^2} \frac{\Lambda_s}{\Lambda_r} \right) \left(\frac{V_r}{V_s} \right) (\kappa_r - \kappa_f) + \kappa_f. \quad (6.3)$$

Next we will use a Lucite sample to help analyze the possible errors and give recommendations to moderate some of these errors.

6.3.1 Error associated with temperature variation

The acoustic velocity of the background fluid in the DARS cavity depends linearly on temperature (Figure 6-1). Therefore, any change in temperature will result in variation of the resonance frequency, and this factor should be carefully considered.

The possible temperature drift in a DARS experiment is between the empty cavity and sample-loaded cavity in two consecutive measurements. Here we assume that the temperature variation exists only in the two measurements for the test sample, but not for the reference sample. The temperature change is transformed into frequency, ω_{0s} , in Eqn (6.3), through the linear correlation between the fluid acoustic velocity and temperature (Figure 6-1). The other parameters in Eqn (6.2) are held constant. We calculate the compressibility and bulk modulus of the Lucite sample at varying temperatures and plot the results in Figure 6-4. The corresponding error in bulk modulus and compressibility caused by temperature variation is shown in Figure 6-5. It is clear that the temperature drift has a strong effect on the estimation of the bulk modulus and compressibility.

In the current DARS apparatus, the temperature is loosely controlled by a room air conditioner, and a slow temperature drift with time always exists in the measurement (Figure 6-6). The typical rate of temperature change with time is about ± 0.5 °C/12hr. The time interval between the empty cavity and sample-loaded cavity measurements is about 5 minutes; therefore, the possible temperature change between the two consecutive measurements is about ± 0.007 °C. The resultant error in bulk modulus and compressibility is about 2% (Figure 6-4), which is still tolerable. If the time interval between the two measurements is long or large temperature fluctuations are observed, the temperature effect should be carefully considered.

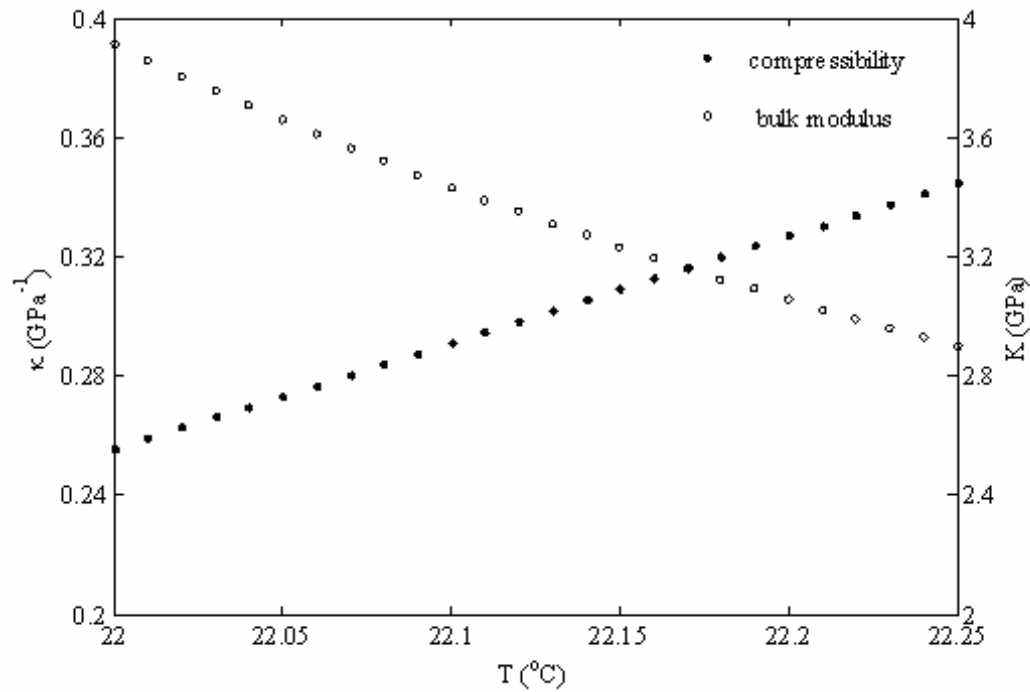


Figure 6-4. Sensitivity of estimated bulk modulus and compressibility to temperature drift in DARS measurement. A Lucite sample is used in this study.

There are two approaches to moderating the temperature-drift effect. The first is to build a highly sensitive thermal control unit through which the variation of the measurement temperature can be maintained in an acceptable range, say less than 0.01 °C. The advantage of this idea is that the temperature effect thus can be neglected. However, this method is not cost-effective. A custom-designed thermal unit at this sensitivity level can easily cost \$20k-\$50k. Moreover, adding this sophisticated instrument will inevitably complicate the operation and slow down the measurement procedure. The second method is to use a high-sensitivity thermal probe and temperature module to monitor the subtle change in temperature between the empty cavity and sample-loaded cavity measurements. We already know that the acoustic velocity of the background fluid depends linearly on temperature; therefore we may take advantage of this to eliminate the temperature-drift effect on the perturbation measurement. The idea is straightforward: by using the temperature probe we can accurately detect the temperature in the sample-loaded experiment; then, through the linear correlation between the acoustic velocity and temperature, we can precisely back-calculate the ‘corresponding’ empty-cavity resonance frequency at the sample-loaded temperature. The market value of a high-

resolution thermal probe (0.0007-0.001 °C) and temperature module (16 digits resolution) is about \$2k-\$3k.

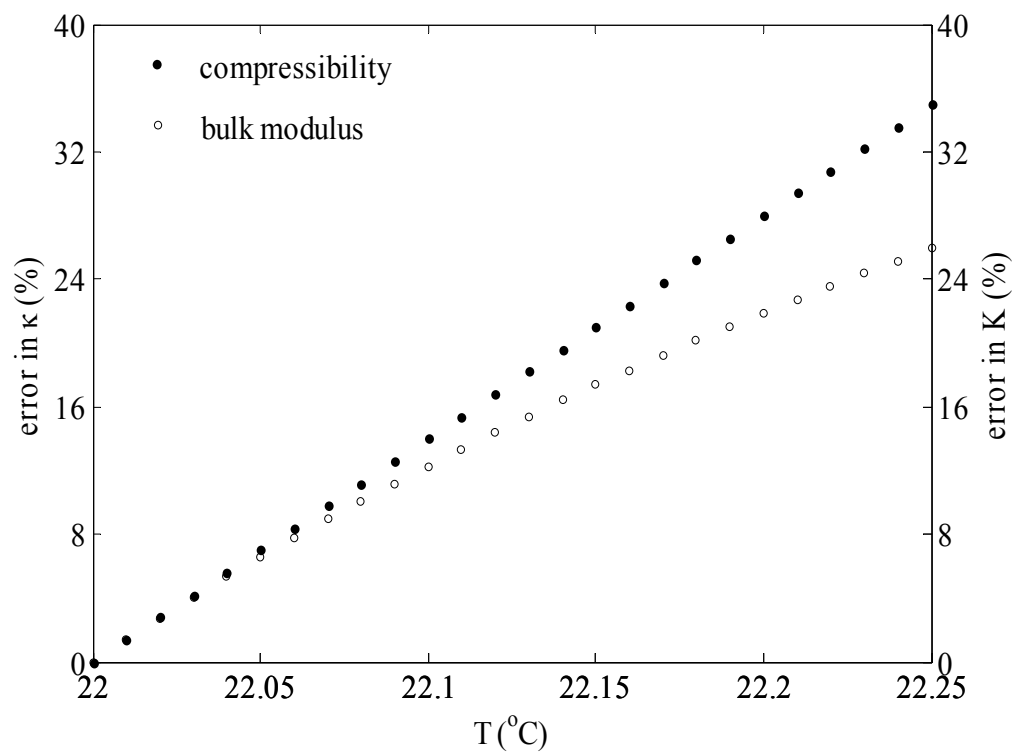


Figure 6-5. Correlation of errors in estimated compressibility and bulk modulus with the uncertainty in the volume of tested samples. A Lucite sample is used in this study.

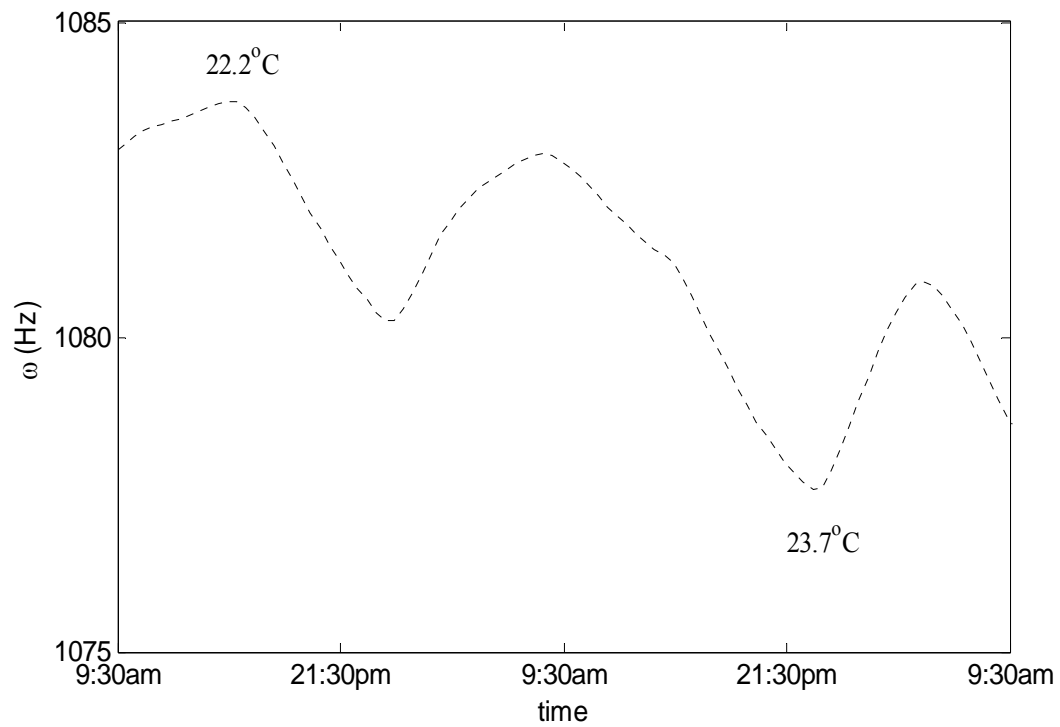


Figure 6-6. Resonance frequency drift with temperature variation of DARS apparatus. This is the empty cavity measurement, but we believe this phenomenon also exists in the sample-loaded measurement.

6.3.2 Instrument error

Inherent instrument error reflects the quality of the measurement instrument. In DARS experiments, this parameter refers to the resolution of the frequency acquisition instrument – the SR850 power lock-in amplifier. The nominal accuracy of this instrument is 30 μHz . This accuracy compared to the frequency step we frequently used in current measurement, 0.01 Hz/step, has large enough resolution window to capture the frequency change; therefore, we can safely ignore the error associated with the instrument.

6.3.3 Error associated with perturbation theory

Perturbation theory provides a first-order description of the resonance characteristic of the acoustic setup; thus any result of the perturbation model inevitably has errors associated with higher-order effects. The major error in the perturbation model comes from the coefficient A . This coefficient, calibrated by a reference sample, is assumed constant over all of the other tested materials, and this assumption forms the foundation of DARS. However, this assumption only holds when the lengths of the reference sample and the tested sample are comparable. Otherwise, the acoustic pressure distribution over the reference sample will be different from that over the tested sample, and thus the coefficient A will be different.

In Chapter 2 we discussed that the first-mode acoustic pressure distribution in a cylindrical cavity with length L_0 is proximately a cosine function,

$$p(x) = p_0 \cos\left(\frac{2\pi x}{L_0}\right),$$

where $p(x)$ is the acoustic pressure at location x ; parameter p_0 is the pressure amplitude. Parameter x is within the range of $[-L_0, L_0]$.

When a sample with length of L_s was put at the center of the cavity, the averaged pressure distribution over the sample would be

$$\bar{p}_s = \frac{A}{L_s} \int_{-L_s/2}^{L_s/2} \cos\left(\frac{2\pi x}{L_0}\right) dx = \frac{AL_0}{\pi L_s} \sin\left(\frac{\pi L_s}{L_0}\right).$$

If the length of the reference sample, L_r , is different from the tested sample, the averaged acoustic pressure over the reference sample then will be

$$\bar{p}_r = \frac{A}{L_r} \int_{-L_r/2}^{L_r/2} \cos\left(\frac{2\pi x}{L_0}\right) dx = \frac{AL_0}{\pi L_r} \sin\left(\frac{\pi L_r}{L_0}\right).$$

The ratio of the \bar{p}_s and \bar{p}_r will be

$$\frac{\bar{p}_s}{\bar{p}_r} = \frac{L_r \sin(\pi L_s / L_0)}{L_s \sin(\pi L_r / L_0)} \propto \frac{L_r}{L_s}. \quad (6.4)$$

Replacing the pressure ratio in Eqn (6.3) with (6.4), we get

$$\kappa_s = \left(\frac{\omega_s^2 - \omega_0^2}{\omega_r^2 - \omega_0^2} \right) \left(\frac{\langle L_s \rangle^2}{\langle L_r \rangle^2} \frac{\Lambda_s}{\Lambda_r} \right) \left(\frac{V_r}{V_s} \right) (\kappa_r - \kappa_f) + \kappa_f. \quad (6.5)$$

Holding all the other parameters constant in Eqn (6.5), we calculate the rate of the change in compressibility and bulk modulus at varying L_s . The result is illustrated in Figure 6-7. The error in both the compressibility and bulk modulus increases with the discrepancy between L_s and L_r . However, the magnitude is relatively small. For instance, a 5% length difference results in 0.1% error in both the compressibility and bulk modulus. This error is acceptable in our current measurement.

For the rock samples used in this thesis, the difference between their length and that of the reference aluminum sample is in the 5% range; therefore, the assumption that the acoustic pressure distribution over the reference sample and the rocks remains constant is reasonably acceptable.

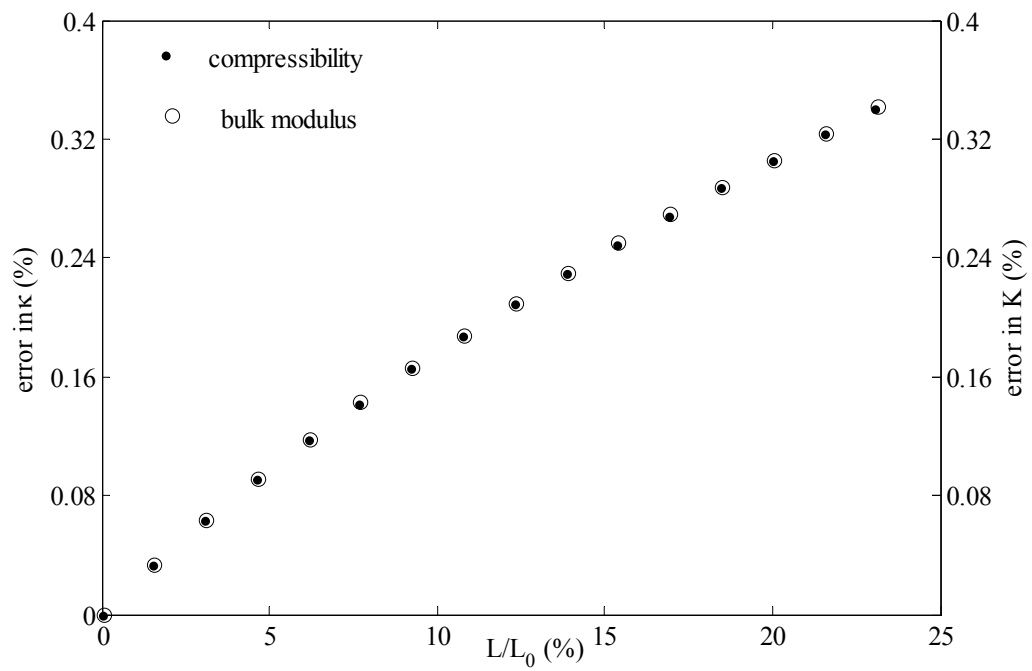


Figure 6-7. Error in estimated compressibility and bulk modulus caused by discrepancy between the length of the reference sample and that of the tested sample. A Lucite sample is used in this study.

6.3.4 Error associated with sample volume measurement

Another major error comes from the uncertainty in the volume measurement of the tested sample. From Eqn (2.3), we know that the sample volume has a first-order effect on the resonance frequency and thus on the estimated compressibility of the tested sample. To study the magnitude of the effect of the uncertainties in sample volume on the compressibility estimation, we calculate the compressibility and bulk modulus under varying degrees of uncertainty in the sample volume, V_s , with Eqn (6.3). All other parameters in the equation were held constant. The estimated compressibility and bulk modulus versus the uncertainties in the sample volume are shown in Figure 6-8. The corresponding errors in the compressibility and bulk modulus are shown in Figure 6-9. It is clear that the uncertainty in the sample

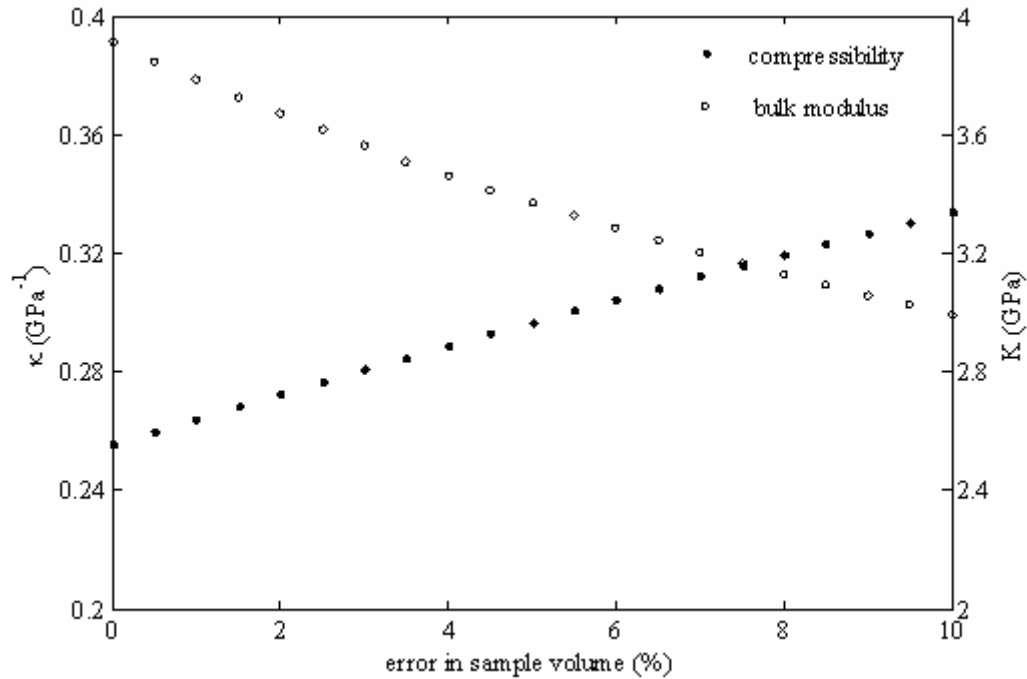


Figure 6-8. Sensitivity of estimated bulk modulus and compressibility to the uncertainties in the volume of the tested sample. A Lucite sample is used in this study.

volume has a strong effect on modulus and compressibility estimation and should be carefully quantified.

All samples used in this study were prepared in a cylindrical shape with a nominal length of 1.5 inches and diameter of 1 inch. The volume of each sample was calculated using

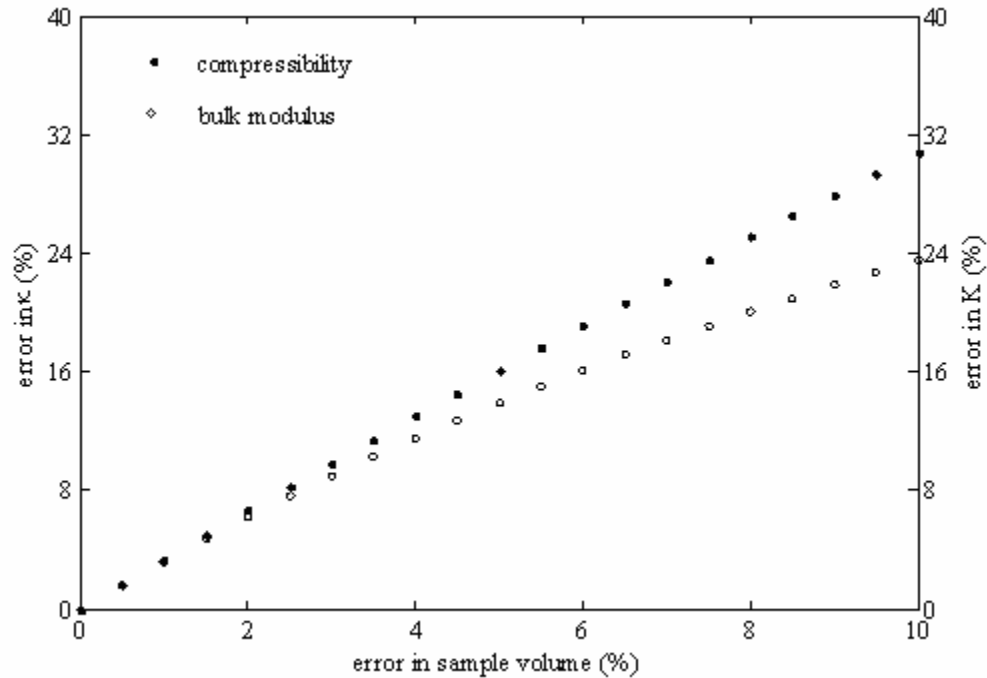


Figure 6-9. Correlation of errors in estimated bulk modulus and compressibility with the uncertainties in the volume of the tested sample. A Lucite sample is used in this study.

the measured diameter and length. The diameter and length are the average of five measurements taken at different orientations and positions. The nominal accuracy of the measurement tool, a caliper in our case, is ± 0.001 inch; therefore, the uncertainty in the sample volume caused by the inherent error of the measurement tool is far less than 0.01% of the sample volume; therefore, this small effect can be safely ignored (Figure 6-9). The major error associated with volume measurement is caused by the ‘irregular’ shape of the sample. Although all of the tested samples were carefully drilled to maintain a cylindrical shape, we still observe a ± 0.005 inch change in diameter for most of the samples. Even worse are the uncertainties in the length measurements. The two ends for most of the samples are not completely parallel, with most having a ± 0.015 inch change in length depending on radial position. Therefore, the ± 0.005 inch uncertainty in diameter and ± 0.015 inch uncertainty in

length can result in 1.0-1.8% uncertainty of the calculated sample volume. From Figure 6-9 we can tell that this 1.0-1.8% volume uncertainty can result in 3-7% error in the compressibility and bulk modulus estimations. The small uncertainty in the sample volume is magnified when we calculate the compressibility and modulus with Eqn (2.7) and (2.8).

To achieve 1% accuracy in the estimation of compressibility and bulk modulus, the maximum tolerance for error in the sample volume is 0.4%, which is far beyond the capacity of our current volume measurement method. An approach under consideration is to use a liquid displacement method, e.g., a high-resolution baker or custom designed apparatus. This may yield a more reliable reading of sample volume; also, it gives us more flexibility about the sample shape. As we discussed in section 6.2.3, DARS is not sensitive to sample shape, a fact we should exploit. We can still rely on the routine caliper measurement; however, we need to machine the samples to closer tolerances to achieve 0.4% accuracy in volume measurement. This strict requirement apparently excludes many of the fragile earth materials that are of most interest, such as coals and most reservoir rocks.

Summarizing the four errors, the dominant errors are caused by the uncertainty in the sample volume and the changing temperature in the experiment. However, these two errors are controllable or at least can be improved. The other two errors, related to the nature of the measurement instrument and the perturbation theory, are inevitable; however, their effects are relatively small and in most cases can be ignored.

Finally, the error in the ultrasound velocity measurements of the reference sample may also affect the accuracy of the compressibility estimate of DARS tested materials, by affecting the compressibility of the reference material. For instance, a ± 15 m/s variation was observed both in the p- and s-wave velocity results of which are 6320 ± 15 m/s and 3090 ± 15 m/s, respectively. The variations of the two velocities result in a $\pm 0.2\%$ uncertainty in the compressibility estimate of the aluminum sample. This uncertainty in the aluminum's compressibility will finally be transformed into the compressibility estimate of the tested samples. Fortunately, the error contribution by the uncertainty in the reference sample's compressibility is relatively small, less than 0.3% for most of the studied materials.

6.4 Effect of open flow surface on effective compressibility

From Eqn (3.5) in Chapter 3, we know that the effective compressibility is a function of the volume of the dynamic flow across the open surface boundary of the tested sample. An

immediate question to ask is what is the effect of the open flow surface area on the effective compressibility, because the open area controls the volume of the dynamic flow. To answer this question, we prepared four Berea samples (A, B, C and D), which were drilled from the same rock block. The four samples have same dimension —1.5 inches in length and 1 inch in diameter —and identical statistic properties, such as permeability, porosity, tortuosity and bulk modulus. The four samples were prepared with different surface boundary configurations: sample A has fully closed surface; sample B has the cylindrical surface sealed but two ends open; sample C has the two ends sealed but the cylindrical surface open; and sample D is fully open. The configuration of the boundary conditions of the four samples is shown in Figure 6-10. The four samples were saturated with the same fluid as in the DARS cavity.

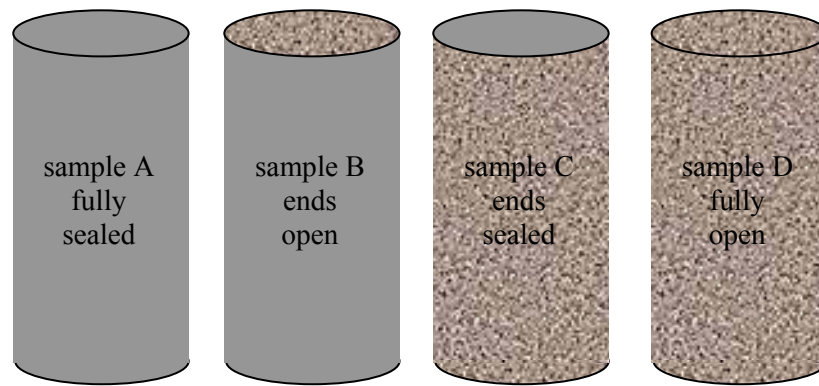


Figure 6-10. Configuration of the surface boundary for four Berea samples. The four rocks were cut from the same Berea sandstone rock block and prepared with following surface boundary conditions (left to right): Sample A - fully sealed with epoxy; Sample B - cylindrical surface sealed with epoxy; Sample C - two ends sealed with epoxy; Sample D - fully open sample surface.

We calculated the compressibility of the four samples from DARS measurement results and plotted the compressibility versus the corresponding open surface area in Figure 6-11. The compressibility increases systematically with the increment of open surface area. Sample A has zero open surface area; therefore, its compressibility is the smallest. Sample D has the maximum open surface area, thus it has the maximum compressibility. The compressibility of sample B and C are located between that of sample A and D and are

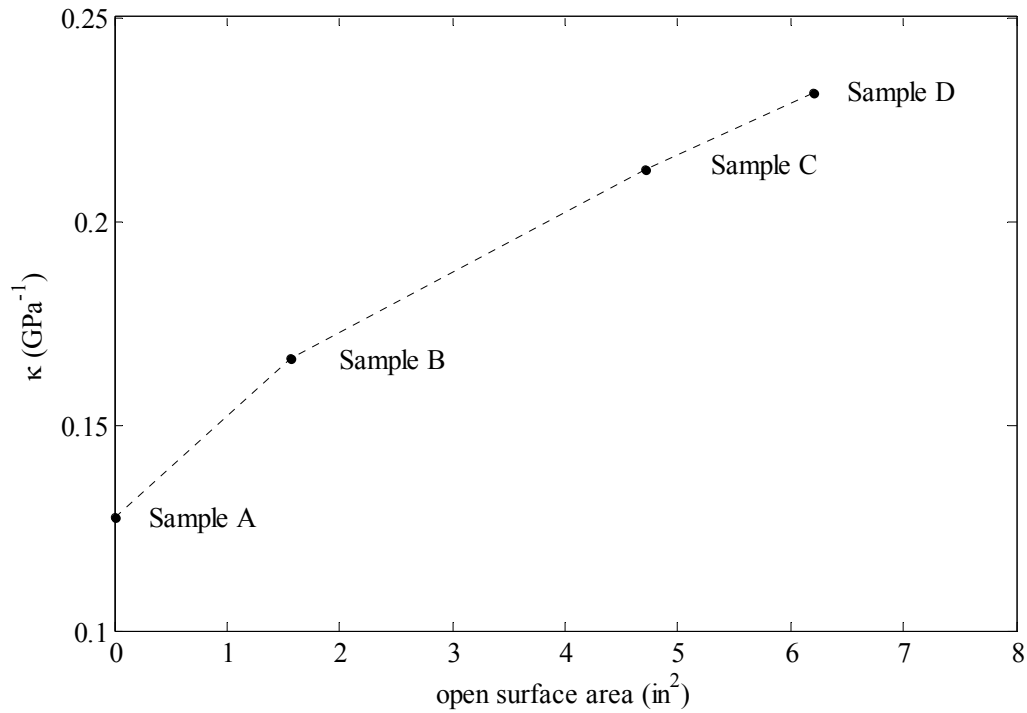


Figure 6-11. Effective compressibility versus open flow surface area. The four rocks were cut from the same Berea sandstone rock block. Sample A - fully sealed with epoxy; Sample B - cylindrical surface sealed with epoxy; Sample C - two ends sealed with epoxy; Sample D - fully open sample surface.

consistent with their open surface area. The interesting observation is that the compressibility does not depend linearly on the open surface area. This phenomenon is due to the difference of the dynamic flow paths inside the four samples. In sample B, the dynamic flow is along the axial direction of the sample. In sample C, the dynamic flow is in the radial direction. In sample D, however, the dynamic flow is three dimensional and the regime of the flow path is completely different from that in samples B and C. Therefore, the pattern of the open surface will affect the path and efficiency of the dynamic flow.

6.5 Diffusion depth discussion

The solid and fluid interaction in DARS measurement of porous materials is a dynamic diffusion process. We are interested in how deep the dynamic diffusion penetrates into the porous medium. This question is critical because it reflects the quality and reliability

of the DARS measurement. For instance, if the dynamic diffusion only penetrates a shallow zone of the tested sample, the property we interpreted may not represent the bulk property of the sample.

We used diffusion depth to help us study this problem. Diffusion depth in this thesis is defined by the distance in the tested sample where the diffusion pressure is $1/e$ times of the pressure on the sample surface.

$$p(L_d) = \frac{P_0}{e}.$$

In a finite 1D diffusion regime (Chapter 3, section 3.3), the pressure profile is

$$p(x) = \frac{e^{\alpha L}}{1 + e^{2\alpha L}} (e^{\alpha x} + e^{-\alpha x}) p_0.$$

Therefore, the pressure at diffusion depth L_d will be

$$p(L_d) = \frac{e^{\alpha L}}{1 + e^{2\alpha L}} (e^{\alpha(L-L_d)} + e^{-\alpha(L-L_d)}) p_0 = \frac{P_0}{e}. \quad (6.6)$$

It is difficult to derive an explicit expression for L_d from Eqn. (6.6), so we did numerical analysis. The frequency used in this study was 1000 Hz, and the porosity of the model was 20%. We calculated the diffusion depth of models with a variety of permeability and length combinations. The results are shown in Figure 6-12. The color bar represents the ratio of diffusion depth, L_d , to model length, L . Red means the diffusion depth is comparable to the length of the model, or the dynamic diffusion senses the whole section of the studied model. On the other hand, dark blue means the diffusion depth is far less the model length and the dynamic diffusion only penetrates a very shallow zone of the model. For instance, if we have a sample with permeability of 30 mD, from Eqn (6.6) we calculated the diffusion depth of the sample is about 1 cm. If the sample length is 10cm, the diffusion length thus is only 10% of the sample length and the dynamic flow recovers only a small section of the sample. To improve the recovery ratio, the simple way is to cut the sample shorter, e.g., 1 cm.

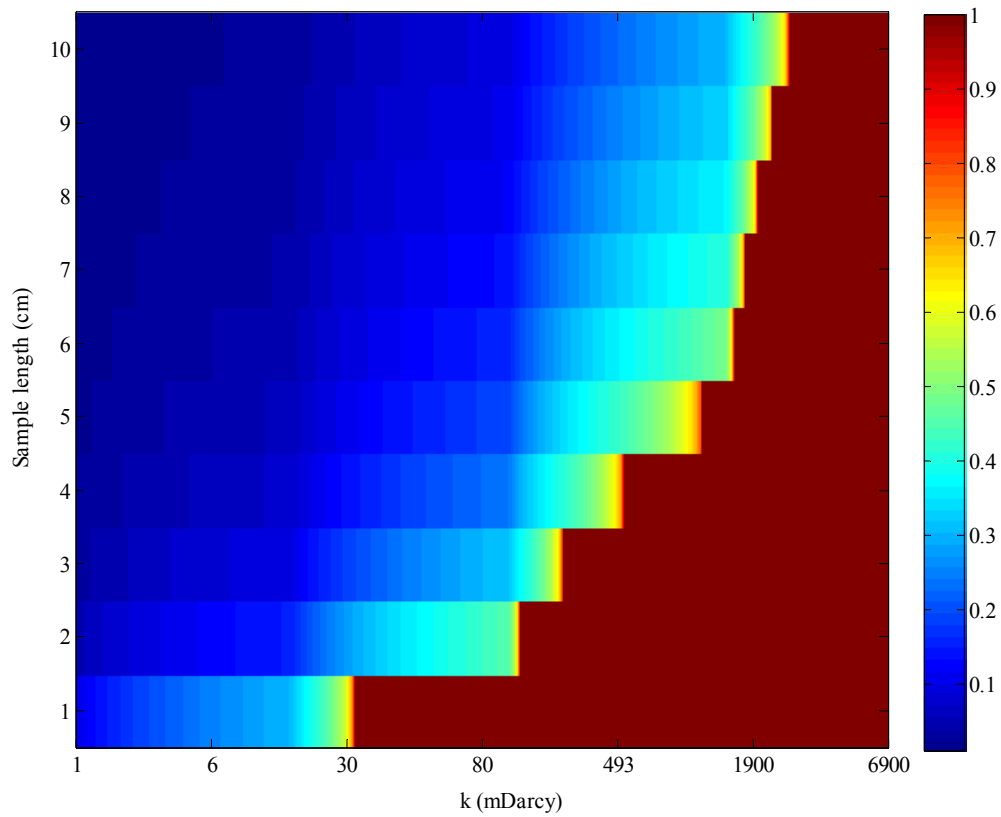


Figure 6-12. Ratio of diffusion depth to sample length for rocks with varying permeabilities. The color bar represents the ratio of the diffusion depth, L_d , to the model length, L . Red means the diffusion depth is comparable to the sample length; deep blue means the diffusion length is far less than the sample length.

6.6 Conclusions

There are four error resources in DARS experiment: measurement error caused by temperature drift; error caused by uncertainties in the volume of the tested samples; system error associated with the instrument and inherent error in the perturbation theory. The first two are the major errors and have a strong effect on the estimated compressibility and bulk modulus of the tested samples. The other two errors are inevitable; however, their effects are of high order and in most cases can be neglected.

Temperature variation in DARS measurements changes the resonance frequency by affecting the acoustic velocity of the background fluid medium. The volume of the tested sample has a first-order effect on frequency shift in DARS measurement. To satisfy the perturbation theory, the sample size should be limited to a range of 2-4% of the cavity size. The volume of the reference material and the tested sample should match.

DARS is insensitive to the shape of the tested sample. This feature provides the potential to measure materials with irregular shapes, such as drilling cuts, which are abundant but hard to measure with routine rock physics measurement techniques.

The pattern of the open surface boundary for porous materials controls the volume of the dynamic flow across the surface boundary thus it has significant effect on the effective compressibility.

Dynamic diffusion in DARS measurement of porous materials provides a way to investigate the flow properties of porous media. However, the estimated flow property is subject to the depth the dynamic flow can penetrate into the sample. If the dynamic flow senses only a small section of the sample body, the flow property may not represent the bulk property of the tested sample.

Chapter 7

Summary of conclusions and assumptions

7.1 Differential Acoustic Resonance Spectroscopy

These are the major steps I completed for the development and application of differential acoustic resonance spectroscopy technique.

(1) I constructed a (DARS) system based upon an acoustic perturbation theory.

(2) I successfully conducted lab measurements on both nonporous materials and porous materials with the DARS setup.

(3) I developed an analytical compressibility model based on a dynamic diffusion concept and, the results yielded by both the analytical model and DARS observations on a set of 17 porous samples match reasonably well.

(4) I combined the analytical model with DARS measurement to predict the permeability of the 17 samples and compared the results with those given by direct gas injection measurement; the results agree well for the materials with intermediate permeability, e.g., 10 to several thousand mD.

(5) I applied COMSOL, a finite-element tool, to study the diffusion phenomenon in a finite, cylindrical medium with homogeneous and heterogeneous flow regimes. I compared the numerical results of the diffusion pressure for the 1D axial diffusion model (homogeneous) with those given by a 1D analytical solution; the results agree well.

(6) I estimated the dynamic-flow-related compressibility of the 1D homogeneous model and compared the estimated compressibility with that given by our analytical compressibility model. The results match reasonably well.

7.2 General conclusions

We have developed a procedure for estimating the effective compressibility of saturated rocks under a dynamic fluid loading condition.

DARS-estimated compressibility for nonporous materials matches that derived from ultrasonic velocity measurement and density measurement; however, this is not always true for porous materials.

The agreement of the results given by both the analytical compressibility model and the DARS measurement indicates that the interaction between the fluid and solid in porous media is a complex dynamic diffusion process.

Our current setup is appropriate for porous rocks with intermediate permeability. To extend the measurement to low-permeability rocks, we need to design a longer cavity. To study high-permeability rocks, we need to explore higher resonance modes.

The undrained measurements on porous materials yield the wet-frame bulk modulus, which is equivalent to the Gassmann low-frequency wet-frame bulk modulus of porous samples.

7.3 Major assumptions

The following are the major assumptions related to DARS measurement and the perturbation model, Eqn (2.7):

- (1) The effect of the energy radiation of an open-ended cavity is small and can be ignored.
- (2) The acoustic pressure is constant over different tested samples.
- (3) At the center of the cavity, the value of the acoustic velocity is small and can be ignored compared to the acoustic pressure; thus the frequency shift is entirely caused by the perturbation on the acoustic pressure field.
- (4) Temperature drift can be ignored in both the empty-cavity and sample-loaded-cavity measurements.
- (5) In DARS undrained measurements, the pressure distribution inside the sample has no effect on the perturbation measurement.

The following are the major assumptions in the derivation of the 1D analytical compressibility model, Eqn (3.8):

- (1) The porous medium is homogeneous and isotropic.
- (2) Diffusion in the pore space is purely in one dimension along the axial direction.
- (3) The sample matrix is incompressible as compared to the pore fluid.
- (4) The medium is a perfect right circular cylinder; thus we can integrate the diffusion pressure profile in the pore space to get an explicit expression for the effective compressibility, Eqn (3.8).
- (5) The permeability we estimate by combining the DARS measurement with the analytical compressibility model represents the global permeability, regardless of how deep the diffusing flow is sensing into the sample.

Appendix A

Standing wave

Acoustic wave equation states that

$$\frac{\partial^2 p}{\partial t^2} = \rho \kappa \nabla^2 p, \quad (\text{A.1})$$

where parameter ρ and κ represent the density and compressibility of air, and p is the acoustic pressure field.

The 1D solution of Eqn (A.1) is given by

$$p(x, t) = A \sin[k(x - vt) + \theta], \text{ or } p(x, t) = A \sin(kx - \omega t + \theta),$$

where k is wave number defined by $k \equiv 2\pi/\lambda = \omega/v$; ω is angular frequency define by $\omega = 2\pi f$; λ is wavelength; θ is phase angle; and v is the traveling velocity given by $v = 1/\sqrt{\rho\kappa}$.

If a sound wave hits a rigid wall, then displacements perpendicular to that rigid wall are not possible; therefore, the wave is reflected from the wall, such that the component of the wave vector perpendicular to the wall changes sign. If the wave e.g. travels in a rectangular box with rigid walls perpendicular to one set of walls, the total wave will consist of the coupling of the wave itself, the first reflection from a wall, and other reflections from the other walls, etc.

If we choose the wavelength in such a way that the last wave coincides with the original wave, then a resonance occurs, and the wave formed this way is called a standing wave. Note that the boundary condition at the wall is such that the displacement should be

zero, or the amplitude of the pressure a maximum. The sum of two waves traveling in opposite directions is given by:

$$\begin{aligned} p(x,t) &= A[\cos(kx - \omega t) + \theta] + \cos[\cos(-kx - \omega t) + \theta] \\ &= 2A \cos(kx + \theta) \cos(\omega t) \end{aligned} \quad (\text{A.2})$$

The condition for resonance is that $\cos(kx + \theta)$ is one for $x = 0$ and for $x = L_x$ if L_x is the length of the box. This condition is fulfilled for $k = n\pi / L_x$ with $n = 1, 2, 3, \dots$.

At low frequency, the longitudinal resonance modes dominate the acoustic response in the cavity and the acoustic pressure is a sinusoid. For the fundamental mode, there is one node at the center. The basic wave relationship leads to the frequency of the fundamental:

$$f = \frac{v}{2L} \quad (\text{A.3})$$

Appendix B

Nonlinear curve fitting

A sharp resonance can be described by the Lorentzian formula (Mehl, 1978):

$$a = \frac{A_0}{[w + i(\omega - \omega_0)]}, \quad (\text{B.1})$$

in which $|a|$ is measured signal amplitude, $\arg a$ is the phase of it, ω_0 is the frequency of the normal mode, w is the line-width, and A_0 is the peak amplitude.

In the presence of a large background signal, nonlinear fitting is essential to processing complicated data. This technique makes it possible to use more complicated functions to describe the background. Assuming the background, which is linear with respect to ω , is

$$a_b = b_1 + ib_2 + (c_1 + ic_2)(\omega_1 - \omega_0). \quad (\text{B.2})$$

The conventional Lorentzian form is simply modified as follows:

$$a = \frac{A_0 f}{[2wf_0 + i(f^2 - f_0^2 + w^2)]}. \quad (\text{B.3})$$

Then a data set $\{f_i, w_i\}$, $i = 1, 2, 3 \dots N$ can be fit simply by minimizing

$$x^2 = \sum_{i=1}^N [a_i - a(f_i)]^2. \quad (\text{B.4})$$

The resonance frequency and line-width can be picked out from the fitting procedure.

Figure B-1 demonstrates the idea of the fitting. The solid curve in the plot is real recorded data. The anti-symmetry of the data curve was induced by the background noise, cross-talk of the instrument, and the overlapping of adjacent modes. The combination of these deficiencies will distort the resonance peak and if we simply pick the peak frequency as the resonance frequency, we may mis-interpret the measurement result. I observed that the peak frequency read out directly from the data is always higher than that given by the curve fit, and this phenomenon associates both within DARS empty cavity and sample loaded measurements. In Table B-1, as an example, I listed the frequencies given by the two different approaches of the 5 solid samples used to test the cavity. Clearly, the direct reading yields larger estimates of the frequency. I also calculated and compared the compressibility of the four plastic materials by using the frequencies given by the two different methods. The compressibility derived from the direct reading frequency is different from that derived from the curve fit frequency. Even though the magnitude of the difference is small, less than 1.5%, it is clearly there. Therefore, to have more accurate estimate of the compressibility of the tested materials, we should use the curve fit frequency results. The aluminum is chosen as the reference sample whose compressibility is derived from ultrasound velocity measurements.

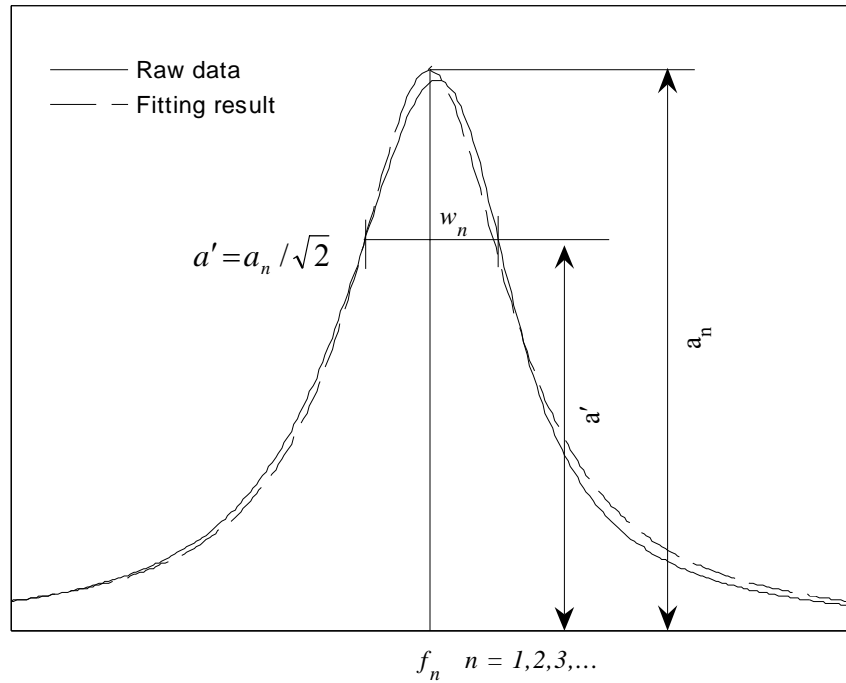


Figure B-1. Lorentzian curve-fitting technique.

Table B-1. Frequency data and compressibility of 5 nonporous samples.

	Direct reading from data				Curve fit				Difference in compressibility
	ω_0 (Hz)	ω_s (Hz)	$\omega_s - \omega_0$ (Hz)	κ_s (GPa ⁻¹)	ω_0 (Hz)	ω_s (Hz)	$\omega_s - \omega_0$ (Hz)	κ_s (GPa ⁻¹)	
Aluminum	1082.1	1091.5	9.4337	0.0118	1082.0	1091.4	9.4319	0.0118	Reference
Delrin	1082.4	1090.4	8.0617	0.1698	1082.2	1090.3	8.0771	0.1715	-1%
Lucite	1081.5	1089.4	7.9467	0.1853	1081.3	1089.3	7.9208	0.1833	1.09%
PVC	1082.6	1090.3	7.6887	0.2032	1082.5	1090.2	7.7124	0.2059	-1.34%
Teflon	1082.8	1089.4	6.5697	0.3383	1082.6	1089.2	6.5659	0.3377	0.17%

Appendix C

Sample preparation

All rock samples studied in this thesis are drilled with a nominal diameter, d , of 1 inch and cut with a nominal length, l , of 1.5 inch. The cores were rinsed, dried at ambient temperature for one day, and then oven dried at 85°C for two days and then allowed to cool down to room temperature in a desiccator.

Ultrasound p- and s-wave velocities, density, porosity and permeability are measured before the DARS measurements. All velocity measurements are taken at room temperature in a pressure vessel filled with hydraulic oil used as pressure fluid. Samples are jacketed by Tygon tubing. In the measurement, a 0.5 bar confining pressure is applied to obtain a better sample-sensor coupling, and the pore pressure is vented to atmosphere, thus the effective pressure is simply the confining pressure. Standard ultrasonic transmission technique is used to measure velocity.

Nitrogen gas permeability, k_g , was measured in a Hassler-type core holder at a confining pressure of 300 psi. For the tested sample, the permeability to nitrogen ranged from 0.5 mD to 12 Darcy. Porosity was measured with a porometer. The porosity of studied materials ranged from about 0.4% to 35%. Core properties are provided with the individual data sets. Densities of the studied rocks are measured by the routine mass-to-bulk volume ratio. The wet densities are calculated based on the dry frame density, density of the saturated fluid, and measured porosity.

After the velocity, density, porosity and permeability measurements, the samples were immersed in a tank filled with the same fluid as inside the acoustic resonator and the pressure of the tank was decreased to 0.1 torr for 4 hours. This depressurization induces expansion of the gas bubbles trapped in the samples. Eventually, air escapes from the porous media. Finally, fluid is forced to fill the pore structure previously occupied by the air fraction as the tank re-equilibrates to atmosphere pressure.

Appendix D

1D diffusion equation

Considering an arbitrary domain, Ω , in a fluid-saturated porous medium (Figure D-1), the mass of the fluid stored inside Ω is

$$M = \iiint_{\Omega} \rho_f dx dy dz, \quad (\text{D.1})$$

where ρ_f is the density of the pore fluid.

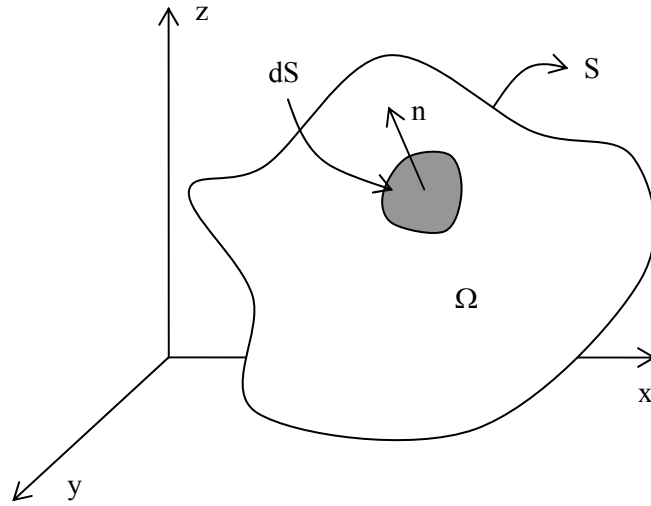


Figure D-1. Configuration of mass divergence in an arbitrary domain, Ω .

The rate of the mass change with respect to time can be written as

$$\frac{dM}{dt} = \iiint_{\Omega} (\rho_f)_t dx dy dz. \quad (D.2)$$

In Eqn (D.2), $(\rho_f)_t$ is the rate of change of the density with time.

If there is no sink inside Ω , the mass of the pore fluid inside this region cannot change except by flowing in or out through the boundary surface S of domain Ω :

$$\frac{dM}{dt} = \oiint_S \left(\rho_f \cdot \frac{\partial \Phi}{\partial n} \right) dS, \quad (D.3)$$

where Φ is flow velocity potential and $\partial \Phi / \partial n$ is the directional derivative in the outward normal direction, n being the unit outward normal vector on boundary of domain Ω . Therefore, $\rho_f (\partial \Phi / \partial n)$ is the mass flux through the surface boundary S of domain Ω .

According to Darcy's law, the velocity of the fluid flow inside a porous medium can be written as

$$\bar{u} = \frac{\partial \Phi}{\partial n} = - \frac{\bar{k}}{\phi \eta} \nabla p, \quad (D.4)$$

in which ϕ and \bar{k} are the porosity and permeability of the medium, and η is the viscosity of the pore fluid. For a homogenous and isotropic medium, the permeability is a scalar. To be more general, here I treat it as a tensor.

Substituting Eqn (D.4) in (D.3), we get

$$\frac{dM}{dt} = \oiint_S \left(- \rho_f \frac{\bar{k}}{\phi \eta} \nabla p \right) dS. \quad (D.5)$$

Hence, we have

$$\frac{dM}{dt} = \iiint_{\Omega} (\rho_f)_t dx dy dz = \oiint_S \left(- \rho_f \frac{\bar{k}}{\phi \eta} \nabla p \right) dS. \quad (D.6)$$

Because the domain D is chosen arbitrarily, by Green's theorem, we can write Eqn (D.6) as

$$\iiint_{\Omega} (\rho_f)_t dx dy dz = \iiint_{\Omega} \nabla \cdot \left(-\rho_f \frac{\bar{\bar{k}}}{\phi \eta} \nabla p \right) dx dy dz. \quad (\text{D.7})$$

Therefore we get

$$(\rho_f)_t = \nabla \cdot \left(-\rho_f \frac{\bar{\bar{k}}}{\phi \eta} \nabla p \right). \quad (\text{D.8})$$

To get a connection between the rate of density change with respect to time and that of pressure, we apply the definition of compressibility, which states that

$$\kappa_f = -\frac{1}{V_0} \frac{\Delta V_f}{\Delta p}, \quad (\text{D.9})$$

in which V_0 is the total volume of the fluid inside an arbitrary portion of the porous material; parameter Δp is the stress applied on the fluid and ΔV_f is the corresponding volume change of the fluid.

The volume change of the fluid can also be expressed as

$$\Delta V_f = \frac{M}{\rho_{f0}} - \frac{M}{\rho'_f} = \frac{M(\rho'_f - \rho_{f0})}{\rho_{f0}\rho'_f} = \frac{M\Delta\rho_f}{\rho_{f0}\rho'_f}. \quad (\text{D.10})$$

In Eqn (D.10), ρ_{f0} and ρ'_f are the density of the fluid with and without the certain stress. If we furthermore assume that the fluid is slightly compressible, e.g., $\rho'_f \approx \rho_{f0}$, then we can rewrite Eqn (D.10) as

$$\Delta V_f = \frac{M\Delta\rho_f}{\rho_{f0}^2} = \frac{V_0\Delta\rho_f}{\rho_{f0}}. \quad (\text{D.11})$$

Substituting Eqn (D.11) into (D.9), we have

$$\kappa_f = -\frac{1}{V_0} \frac{\Delta V_f}{\Delta p} = -\frac{1}{\rho_{f0}} \frac{\Delta \rho_f}{\Delta p}. \quad (\text{D.12})$$

If the pressure change is time dependent, Eqn (D.12) then can be written as

$$\kappa_f = -\frac{1}{\rho_{f0}} \frac{\left(\Delta \rho_f / \Delta t \right)}{\left(\Delta p / \Delta t \right)}. \quad (\text{D.13})$$

If the time variable is infinitely small, we can rewrite Eqn (D.13) as

$$\kappa_f = -\frac{1}{\rho_{f0}} \lim_{t \rightarrow 0} \frac{\left(\Delta \rho_f / \Delta t \right)}{\left(\Delta p / \Delta t \right)} = -\frac{1}{\rho_{f0}} \frac{(\rho_f)_t}{p_t}. \quad (\text{D.14})$$

Rearranging Eqn (D.14) we get

$$(\rho_f)_t = -\rho_{f0} \kappa_f p. \quad (\text{D.15})$$

Replacing the term $(\rho_f)_t$ in (D.8) with Eqn (D.15), we have

$$-\rho_{f0} \kappa_f p_t = \nabla \cdot \left(-\rho_f \frac{\bar{\bar{k}}}{\phi \eta} \nabla p \right). \quad (\text{D.16})$$

If the density of the fluid is spatially constant in region Ω , Eqn (D.16) can then be expressed as

$$p_t = \frac{\bar{\bar{k}}}{\phi \eta \kappa_f} \nabla^2 p. \quad (\text{D.17})$$

Setting $D = \bar{\bar{k}} / \phi \eta \kappa_f$, we get the final expression of the diffusion equation,

$$\nabla^2 p = \frac{1}{D} \frac{\partial p}{\partial t}, \quad (\text{D.18})$$

or,

$$\frac{\partial^2 p}{\partial x^2} + \frac{\partial^2 p}{\partial y^2} + \frac{\partial^2 p}{\partial z^2} = \frac{1}{D} \frac{\partial p}{\partial t}. \quad (\text{D.19})$$

The parameter D in Eqn (D.17) is the diffusivity of the porous medium and has the dimension $[l^2/t]$.

In homogeneous porous media, the diffusion is dependent on only one coordinate and Eqn (D.19) can be simplified to a 1D expression

$$\frac{\partial^2 p}{\partial x^2} = \frac{1}{D} \frac{\partial p}{\partial t}. \quad (\text{D.20})$$

Furthermore, if acoustic pressure is time harmonic, i.e., $p(r,t) = p(r)e^{i\omega t}$, we can rewrite Eqn (D.20) as

$$\frac{\partial^2 p}{\partial x^2} - \frac{i\omega}{D} p = 0. \quad (\text{D.21})$$

The general solution of Eqn (D.21) is

$$p(x) = A\Delta P e^{\alpha x}, \quad (\text{D.22})$$

in which ΔP is the amplitude of the pressure change, $\alpha = \sqrt{i\omega/D}$ and A is a constant coefficient.

In our particular case, the sample's side surface is sealed and the dynamic flow is at the two open ends; therefore, the pressure distribution inside the pore space is a superposition

of two opposite pressure profiles, Figure D-2, with boundary conditions $p(L) = p_0$ and $p(-L) = p_0$, separately, and parameter L is the half-length of the sample.

Therefore, we have

$$\begin{aligned} p_1(x) &= p_0 e^{\alpha(x-L)}, \quad (x \leq L) \\ p_2(x) &= p_0 e^{\alpha(-x-L)}, \quad (x \geq -L) \end{aligned} \quad (\text{D.23})$$

Hence the combined pressure profile is

$$p(x) = Ap_1 + Bp_2. \quad (\text{D.24})$$

in which A and B are two constant coefficients.

Reapplying the boundary conditions $p(L) = p_0$ and $p(-L) = p_0$, we get

$$A = B = \frac{e^{2\alpha L}}{1 + e^{2\alpha L}}. \quad (\text{D.25})$$

Thus, the final expression of the pressure field inside the pore fluid will be

$$p(x) = \frac{e^{\alpha L}}{1 + e^{2\alpha L}} p_0 (e^{\alpha x} + e^{-\alpha x}). \quad (\text{D.26})$$

In deriving the diffusion equation, I ignored the compressibility of the solid matrix with the assumption that the matrix is less compressible than the fluid, and thus the porosity can be treated as constant. More generally, the porosity change with pressure should also be considered, and diffusivity D should include the compressibility of the fluid and the solid skeleton simultaneously, e.g., the compressibility in D is a summation of the compressibility of the fluid and that of the solid matrix.

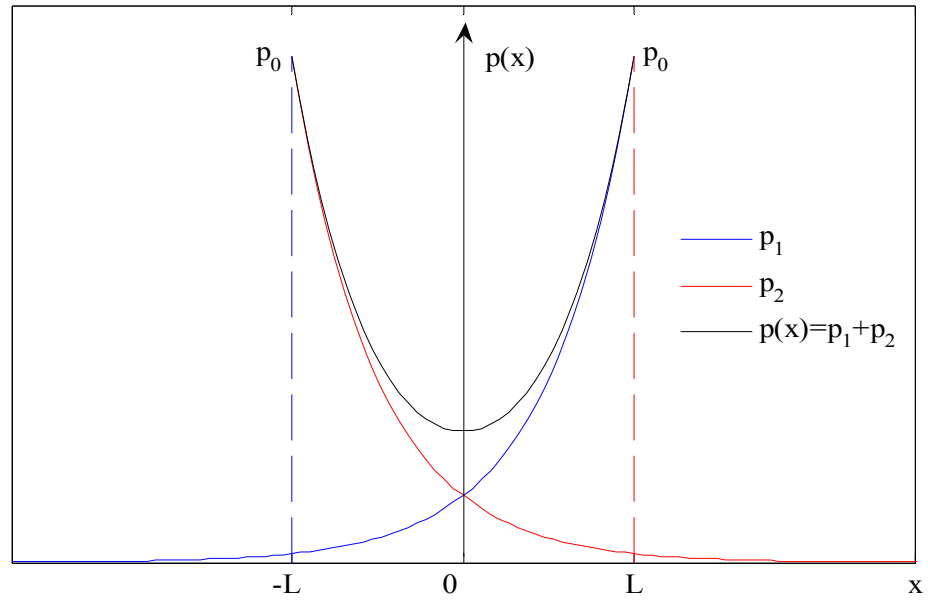


Figure D-2. Pore pressure distribution inside a porous medium under a dynamic fluid-loading condition.

Appendix E

Effective compressibility

The compressibility of a rock sample is evaluated by the bulk-volume-normalized net volume change over the applied net stress. In the following analysis, I assume the rock sample to be homogeneous and isotropic and embedded with pore space, which has arbitrary shape and complexity. The pore space is saturated with fluid.

E.1 Static effective compressibility

Considering a fluid-saturated rock sample with bulk volume V and porosity ϕ , placed in some hydrostatic pressurized fluid, the sample matrix will subsequently shrink and additional fluid will also be introduced into the pore space to balance the pressure gradient inside and outside the sample. The solid matrix and the pore fluid endure equivalent pressure. In rock-physics language, this configuration is called the iso-stress condition, and the corresponding bulk modulus of the rock (including the pore fluid) is called the Reuss lower-bound bulk modulus. The compressibility of the sample under such a stress condition is evaluated by the ratio of the net volume change of the sample and the net pressure applied over the sample body. The net volume change of the sample consists of two contributions, the volume change of the matrix and the extra amount of fluid accumulated in the pore space. Thereafter the bulk compressibility could be superposed from two different experiments. One experiment holds the pore pressure constant and applies stress to the solid matrix; this is the so-called drained state and the acquired compressibility/modulus is purely that of the rock frame matrix. Another experiment is to hold the stress constant and inject fluid in the pore space. The ratio of the change in the volume of fluid added to storage per unit bulk volume divided by the change in pore pressure gives the storage coefficient, a part of the compressibility of the rock attributed to the fluid storage in the pore space.

From the Reuss model, the compressibility of fluid-saturated porous materials can be quantified as

$$\frac{1}{\overline{M}} = \sum \frac{\varphi_i}{M_i}, \quad (\text{E.1})$$

In Eqn (E.1), \overline{M} is the effective modulus; φ_i and M_i are the volume percentages and moduli of the corresponding components.

Rewriting Eqn (E.1) in compressibility form, and for a solid-fluid two-phase system, we get the corresponding Reuss effective compressibility:

$$\kappa_e = (1 - \phi)\kappa_s + \phi\kappa_f. \quad (\text{E.2})$$

The parameter ϕ is the volume percentage of the fluid section, or the porosity of the system.

Equation (E.2) tells that, in an iso-stress condition, the pore fluid dominates the effective compressibility of fluid-saturated porous materials. Since the solid part is harder than the fluid—which is generally true for most sedimentary materials in nature—the iso-stress state yields the upper bound of effective compressibility (or the lower bound of effective bulk modulus) of porous materials. For porous materials with extremely low porosity, the effective compressibility of the material therefore is controlled mainly by the solid matrix, because the contribution from the pore fluid part is small and can be neglected.

E.2 Dynamic effective compressibility

If we repeat the experiment in section E.1, but the applied pressure in the fluid is periodic rather than hydrostatic, the periodic pressure change causes the fluid to flow into and out of the sample. Under this scenario, the effective compressibility of the material can still be quantified by the ratio of the net volumetric strain to the corresponding stress. The net volume change consists of a combination of the change in the solid matrix and the extra amount of fluid flowing in and out the pore structure.

Hence, the effective compressibility of the sample, according to the definition of compressibility, will be,

$$\kappa_e = -\frac{1}{V_s} \frac{(\Delta V_m + \Delta V_f)}{\Delta p}, \quad (\text{E.3})$$

where V_s is the bulk volume of the sample. ΔV_m is the volume change of the matrix (wet in this case), and ΔV_f is the volume change due to the extra fluid flowing into and out of the pore space; Δp is the pressure applied on the sample, which is equivalent to the p_0 in Eqn (D.26).

The volume change of the sample matrix can be derived according to the definition of the compressibility, with the compressibility a required known property of the solid matrix. However, because the sample is saturated and the stress working on the matrix is periodic rather than static, the compressibility of the matrix in this state is not simply the dry-frame compressibility. Here I write the compressibility of the matrix as κ_u , which is defined as the reciprocal of the undrained bulk modulus or Gassmann wet frame bulk modulus for fluid-saturated porous materials; I investigate this quantity in Chapter 5 and the way to quantify it experimentally. Hence, ΔV_m can be expressed as

$$\Delta V_m = -\kappa_u V_s p_0. \quad (\text{E.4})$$

The net volume change of the pore fluid is equal to the amount of fluid flowing into and out of the pore space driven by the periodically changing pressure. Because the fluid pressure profile inside the sample is a function of position Eqn (D.26), a volume integral is required to quantify the total amount of fluid involved in the flow. Since the sample has a cross-sectional area A in the direction that is orthogonal to the pressure gradient, the total volume of the fluid involved in the flow can be written as

$$\Delta V_f = -\int \phi \kappa_f p(x) A dx. \quad (\text{E.5})$$

In our particular case, the samples I measured are cylindrical core plugs. To satisfy 1D flow, I sealed the sample side surface and left only the two ends open (Figure E-1). Therefore, the periodic flow happens only at the two ends of the samples. In this case, the flow area is $A = \pi r_0^2$, therefore Eqn (E.5) can be written as

$$\Delta V_f = -\int \phi \kappa_f p(x) \pi r_0^2 dx . \quad (\text{E.6})$$

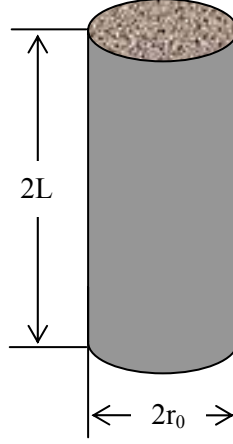


Figure E-1. For a porous sample with cylindrical shape and side surface being sealed, the fluid flow happens only at the two open ends.

Because the flow happens symmetrically on the two ends of the sample, the total amount of the fluid flowing in or out the sample will be

$$\Delta V_f = -\int \phi \kappa_f p(x) dV = -\pi r_0^2 \phi \kappa_f \int p(x) dx . \quad (\text{E.7})$$

Substituting Eqn (E.4) and (E.7) into (E.3), we have

$$\kappa_e = -\frac{1}{V_s} \frac{\left(-\kappa_u V_s p_0 - \pi r_0^2 \phi \kappa_f \int p(x) dx \right)}{p_0} . \quad (\text{E.8})$$

Replacing p_0 with Eqn (D.26) and V_s with $2\pi r_0^2 L$ in Eqn (E.8), we have

$$\kappa_e = \kappa_u + \frac{\phi \kappa_f}{L} \frac{e^{\alpha L}}{1 + e^{2\alpha L}} \int \left(e^{\alpha x} + e^{-\alpha x} \right) dx , \quad (\text{E.9})$$

Ignoring the details of the derivation, we get the final expression of the effective compressibility of a fluid-saturated sample under dynamic loading:

$$\kappa_e = \kappa_u + \frac{\phi \kappa_f}{\alpha L} \frac{e^{2\alpha L} - 1}{e^{2\alpha L} + 1}. \quad (\text{E.10})$$

Appendix F

Crossover frequency

For a given sample with fixed flow properties, a critical frequency exists, below which the pore pressure will partially or maybe fully equilibrate. This critical frequency can be quantified by setting the second derivative of the effective compressibility with respect to frequency equal to zero,

$$\frac{\partial}{\partial \omega} \left(\frac{\partial \kappa_e}{\partial \omega} \right) = 0. \quad (\text{F.1})$$

or,

$$\frac{\partial}{\partial \omega} \left[\frac{\partial}{\partial \omega} \left(\kappa_u + \frac{\phi \kappa_f}{\alpha L} \frac{e^{2\alpha L} - 1}{e^{2\alpha L} + 1} \right) \right] = 0. \quad (\text{F.2})$$

In equation (F.2), the parameter κ_u is frequency independent; hence, this equation can be rewritten as

$$\frac{\partial}{\partial \omega} \left[\frac{\partial}{\partial \omega} \left(\frac{\phi \kappa_f}{\alpha L} \frac{e^{2\alpha L} - 1}{e^{2\alpha L} + 1} \right) \right] = 0. \quad (\text{F.3})$$

To simplify the derivation, we apply three auxiliary parameters, X, Y and Z, which are defined by

$$X = \frac{\phi \kappa_f}{\alpha L}, \quad Y = e^{2\alpha L} \quad \text{and} \quad Z = \frac{e^{2\alpha L} - 1}{e^{2\alpha L} + 1} = \frac{Y - 1}{Y + 1}, \quad \text{respectively.}$$

Therefore, we can simplify Eqn (F.3) as

$$\frac{\partial}{\partial \omega} \left[\frac{\partial}{\partial \omega} (XZ) \right] = X''Z + 2X'Z' + XZ'' = 0. \quad (\text{F.4})$$

Parameter α in equation (F.3) is the only depending parameter on frequency, and its first derivative with respect to frequency is

$$\frac{\partial \alpha}{\partial \omega} = \frac{\partial}{\partial \omega} \left(\sqrt{\frac{i\omega}{D}} \right) = \frac{1}{2\omega} \left(\frac{i\omega}{D} \right) \sqrt{\frac{D}{i\omega}} = \frac{\alpha}{2\omega}. \quad (\text{F.5})$$

The first derivative of X, Y and Z to frequency are

$$X' = \frac{\partial}{\partial \omega} \left(\frac{\phi \kappa_f}{\alpha L} \right) = \frac{\phi \kappa_f}{L} \left(-\frac{1}{\alpha^2} \frac{\alpha}{2\omega} \right) = -\frac{X}{2\omega}. \quad (\text{F.6})$$

$$Y' = \frac{\partial}{\partial \omega} \left(e^{2\alpha L} \right) = \frac{\alpha L}{\omega} e^{2\alpha L} = \frac{\alpha L}{\omega} Y. \quad (\text{F.7})$$

$$Z' = \frac{\partial}{\partial \omega} \left(\frac{Y-1}{Y+1} \right) = \frac{2Y'}{(Y+1)^2}. \quad (\text{F.8})$$

The second derivative of X, Y and Z to frequency are

$$X'' = \frac{\partial}{\partial \omega} \left(-\frac{X}{2\omega} \right) = \frac{X}{4\omega^2}. \quad (\text{F.9})$$

$$Y'' = \frac{\partial}{\partial \omega} \left(\frac{\alpha L}{\omega} Y \right) = \left(\frac{\alpha L}{2\omega^2} + \frac{\alpha^2 L^2}{\omega^2} \right) Y. \quad (\text{F.10})$$

$$Z'' = \frac{\partial}{\partial \omega} \left[\frac{2Y'}{(Y+1)^2} \right] = \frac{2Y''(Y+1) - 4Y'^2}{(Y+1)^3}. \quad (\text{F.11})$$

Substituting the series equations (F.6) to (F.11) into (F.4) and ignoring the tedious mathematics we get

$$\frac{X}{4} \frac{Y-1}{Y+1} - \frac{\alpha L X Y}{(Y+1)^2} - \frac{2\alpha^2 L^2 X Y (Y-1)}{(Y+1)^3} = 0. \quad (\text{F.12})$$

Replacing X and Y with their corresponding expression in equation (F.12) we can solve for the critical frequency.

In the high-frequency range, the system has no time to relax; therefore, nonlinear effects might influence the volume change of the solid matrix. Meanwhile, the inertial effect on the fluid, which increases with frequency, will also affect the fluid flow. All of these issues may complicate the transient flow phenomena.

Appendix G

Permeability estimation

It is difficult to get an explicit expression of permeability from Eqn (4.2),

$$\kappa_e = \kappa_u + C \frac{\phi \kappa_f}{\alpha L} \frac{e^{2\alpha L} - 1}{e^{2\alpha L} + 1}, \alpha = \sqrt{\frac{i\omega}{D}} = \sqrt{\frac{i\omega \phi \eta \kappa_f}{k}}.$$

Hence we will rely on a numerical procedure (Matlab subroutine) to search for the optimal permeability by forcing the calculated κ_e to match the DARS drained compressibility, κ_d .

The procedure follows:

- (1) Give an initial guess of permeability
- (2) Calculate κ_e with Eqn (4.2).
- (3) Compare κ_e with DARS drained compressibility, κ_d , if the match is in 0.1%, then stop the search and the current permeability will be the final solution. Otherwise go to step 4.
- (4) Compare κ_e and κ_d .
 - (4a) If $\kappa_e > \kappa_d$, the permeability is overestimated and it will be scaled down by 1% of the difference between κ_e and κ_d . Then repeat step (3) and (4a) till find the optimal solution of permeability.
 - (4b) If $\kappa_e < \kappa_d$, the permeability is underestimated and will be scaled up by 1% of the difference between κ_e and κ_d . Repeat step (3) and (4b) till find the final solution of permeability.

The reason I scaled the step size of the permeability change in the searching by 1% of the difference between κ_e and κ_d in each iteration is due to two considerations: firstly, the

numerical search converges fast because the step size of the change in permeability is relatively flexible and can be large in the early iterations; secondly, high accuracy in permeability estimate because the step size of the permeability change will be very fine when κ_e getting closer and closer to κ_d .

The accuracy of the estimated permeability is controlled by two constrains, the tolerance of the difference between κ_e and κ_d , and the step size of the permeability change. Of course higher constrain yields better accuracy; however, the sacrifice is computing time. I tried to raise the two constrains by an order: 0.01% tolerance of the difference between κ_e and κ_d , and the step size of permeability change is scaled by 0.1% of the difference between κ_e and κ_d . The accuracy in the permeability estimate is enhanced only by 0.3% with the cost of more than tens of times increase of iterations. The current setup of the two constrains is sufficient for our requirements.

Bibliography

- Barenblatt, G.I., Entov, V.M., and Ryzhik, V.M., 1990, Theory of Fluid Flows through Natural Rocks: Dordrecht, Kluwer Academic Publishers.
- Berryman, J. G., 1999, Origin of Gassmann's equation: Geophysics, 64, 1627-1629.
- Biot, M. A., 1956a, Theory of propagation of elastic waves in a fluid-saturated porous solid. II. High-frequency range: J. Acoust. Soc. Am., 28, 168-178.
- Biot, M. A., 1956b, Theory of propagation of elastic waves in a fluid-saturated porous solid. I. Low-frequency range: J. Acoust. Soc. Am., 28, 179-191.
- Biot, M. A., 1962a, Generalized theory of acoustic propagation in porous media: J. Acoust. Soc. Am., 34, 1254-1264.
- Biot, M. A., 1962b, Mechanics of deformation and acoustic propagation in porous media: J. App. Phys. 33, 1482-1498.
- Bourbie, T., 1987, Acoustics of porous media: Gulf of Publishing Company.
- Brie, A., et al., 1995, Shear sonic interpretation in gas-bearing sands: paper SPE 30595 presented at the APE Annual Technical Conference & Exhibition, Dallas, Oct. 1995.
- Carcione, J. M., Kosloff, D., and Kosloff, R., 1988, Viscoacoustic wave propagation simulation in the earth: Geophysics, 53, 769-777.
- Colgate, S. O., Sivaraman, A. and Reed, K., 1990, Acoustic determination of the ideal-gas heat capacity of n-heptane at high temperature: J. Chem. Thermodynamics, 22, 245-252
- Colgate, S. O., Sona, C.F. Reed K.R. and Sivaraman, A., 1990, Experimental ideal gas reference state heat capacities of gases and vapors: J. Chem & Engi. Data, Vol. 35, No.1, 1990.
- Colgate, S. O., Sivaraman, A. and Dejsupa, C., 1992, Acoustic cavity method for sonic speed measurements in liquids and oils: Fluid Phase Equilibria, 79 (1992) 221-229, Elsevier Science Publishers B.V., Amsterdam.
- Cortis, A., et al., 2003, Influence of pore roughness on high-frequency permeability: Physics of Fluids, 15, 1766-1775.

- Dutta, N. C., and Ode, H., 1979a, Attenuation and dispersion of compressional waves in fluid-filled porous rocks with partial gas saturation (White model) – Part I: Biot theory: *Geophysics*, 44, 1777-1788.
- Dutta, N. C., and Ode, H., 1979b, Attenuation and dispersion of compressional waves in fluid-filled porous rocks with partial gas saturation (White model) – Part II: Results: *Geophysics*, 44, 1789-1805.
- Dutta, N. C., and Sheriff, A. J, 1979, On White's model of attenuation in rocks with partial gas saturation: *Geophysics*, 44, 1806-1812.
- Dvorkin, J., and Nur, A., 1993, Dynamic poroelasticity: A unified model with the squirt and the Biot mechanisms: *Geophysics*, 58, 524-533.
- Dvorkin, J., Nolen-Hoeksema, R., and Nur, A., 1994, The squirt-flow mechanism: Macroscopic description: *Geophysics*, 59, 428-438.
- Dvorkin, J., Mavko, G., and Nur, A., 1995, Squirt flow in fully saturated rocks: *Geophysics*, 60, 97-107.
- Gardner, G.H.F., Wyllie, M.R.J., Droschak, D.M., 1964, Effects of pressure and fluid saturation on the attenuation of elastic waves in sands: *J. Pet. Tech.*, 189-198, 1964
- Gassmann, F., 1951, Uber die elastizitat poroser medien: *Vier. Der Natur Gesellschaft*, 96, 1-23.
- Han, De-hua, and Batzle, M. L., 2004, Gassmann's equation and fluid-saturation effects on seismic velocities: *Geophysics*, 69, 398-405.
- Harris, J. M., 1996, Differential acoustic resonance spectroscopy: STP Annual Report, Stanford, Vol 7, No. 1, July 1996.
- Harris, J. H., Quan, Y. L., Xu, C. T., 2005, Differential Acoustic Resonance Spectroscopy: An experimental method for estimating acoustic attenuation in porous media, SEG expanded abstract, 1569-1572.
- Harris, J. M., 2007, Differential Acoustic Resonance Spectroscopy, SWP internal report.
- Hofmann, R., Batzle, M., Duranti, L. and Han, D. H., 2005, Frequency dependent velocities: mechanism and implications, *Rainbow in the Earth – 2nd International Workshop*, Lawrence Berkeley National Laboratory, Berkeley, California, August 17-18, 2005.
- Hofmann, R., Batzle, M. and Han, D. H., 2000, Fluid control on velocity dispersion, *Petrophysics meets Geophysics – Paris, France*, 6-8 November 2000.

- Johnson, D. J., 1990, Probing porous media with superfluid acoustics: *J. phys.*, SA449-SA455.
- Johnson, D. J., Hemmick, D. L., and Kojima, H., 1994, Probing porous media with first and second sound. I. Dynamic permeability: *J. Appl. Phys.*, 76(1), 104-114.
- Johnson, D. J., 2001, Theory of frequency dependent acoustics in patchy-saturated porous media: *J. Acoust. Soc. Am.*, 110(2), 682-694.
- Knight, R., Dvorkin, J., and Nur, A., 1998, Acoustic signatures of partial saturation: *Geophysics*, 63, 132-138.
- Lemarinier, P., Henry, M., Allard, J-F., Bonardet, J. L., and Gedeon, A., 1995, Connection between the dynamic bulk modulus of air in a porous medium and the specific surface: *J. Acoust. Soc. Am.*, 97(6), 3478-3482.
- Mavko, G. and Nur, A., 1975, Melt squirt in the asthenosphere: *J. Geophys. Res.*, 80, 1444-1448.
- Mavko, G., and Nur, A., 1979, Wave attenuation in partially saturated rocks: *Geophysics*, 44, 161-178.
- Mavko, G., Jizba, D., 1991, Estimating grain-scale fluid effects on velocity dispersion in rocks: *Geophysics*, 56, 1940-1949.
- Mavko, G., Mukerji, T., 1995, Seismic pore space compressibility and Gassmann's relation: *Geophysics*, 60, 1743-1749.
- Mavko, G., Mukerji, T., and Dvorkin, J., 1998, *The rock physics handbook: Tools for seismic analysis in porous media*: Cambridge Univ. Press.
- Murphy, W. F., Winkler, K. W., and Kleinberg, 1984, Contact microphysics and viscous relaxation in sandstones, in Johnson, D. L. and Sen, P. N., Eds., *Physics and Chemistry of Porous media*: Am. Inst. Phys.
- Murphy, W. F., Winkler, K. W., and Kleinberg, 1986, Acoustic relaxation in sedimentary rocks: Dependence on grain contacts and fluid saturation: *Geophysics*, 51, 1986, 757 – 766.
- Mehl, J.B., 1978, Analysis of resonance standing-wave measurements: *J. Acoust. Soc. Am.*, 64(5), Nov, 1978.
- Migliori, A., and Sarrao, J. L., 1997, *Resonant ultrasound spectroscopy: applications to physics, materials measurements, and nondestructive evaluation*: John Wiley & Sons, INC., New York.

- Moldover, M. R., Mehl, J. B. and Greespan, M., 1986, Gas-filled spherical resonator: theory and experiment: *J. Acoust. Soc. Am.*, 79(2).
- Morse, P. M. and Ingard, K. U., 1968, *Theoretical acoustics*: McGraw-Hill Book Company. New York.
- O'Connell, R., and Budiansky, B., 1974, Seismic velocities in dry and saturated cracked solids: *J. Geophys. Res.*, 79, 5412-5426.
- O'Connell, R., and Budiansky, B., 1977, Viscoelastic properties of fluid-saturated cracked solids: *J. Geophys. Res.*, 82, 5719-5736.
- Palmer, I. D., and Traviolia, M. L., 1980, Attenuation by squirt flow in undersaturated gas sands: *Geophysics*, 45, 1780-1792.
- Petyt, M. and Lim, S. P., 1978, Finite element analysis of the noise inside a mechanically excited cylinder: *International Journal for Numerical Methods in Engineering*, Vol. 13, 109-122.
- Pham, N. H., et al., 2002, Wave velocities and attenuation of shaley sandstones as a function of pore pressure and partial saturation: *Geophysical Prospecting*, 50, 615-627.
- Pride, S. R., Berryman, J. G., and Harris, J. M., 2004, Seismic attenuation due to wave-induced flow, *J. of Geophysical Research*, Vol. 109, B01201.
- Pride, S.R., J.M. Harris, D. Johnson, A. Mateeva, K. Nehei, R. Nowack, J. Rector, H. Spetzler, R. Wu, T. Yamamoto, J. Berryman, M. Fehler, 2003, Permeability dependence of seismic amplitudes, *The Leading Edge of Geophysics*, p. 518-525.
- Sam, M. S., Neep, J. P., and Worthington, M. H., 1997, The measurement of velocity dispersion and frequency-dependent intrinsic attenuation in sedimentary rocks: *Geophysics*, 62, 1456-1464.
- Spoor, P. S. and Swift, G. W., 1999, Mode-locking of acoustic resonators and its application to vibration cancellation in acoustic heat engines: *J. Acoust. Soc. Am.*
- Wang, Z., and Nur, A., 1988, Velocity dispersion and the "local flow" mechanism in rocks: 58th Ann. Internat. Mtg., Soc. Explor: Geophysics, Expanded Abstracts, 928-930.
- Wang, Z., 2001, Fundamentals of seismic rock physics: *Geophysics*, 66, 398-412.
- White, J. E., 1975, Computed seismic speeds and attenuation in rocks with partial gas saturation: *Geophysics*, 40, 224-232.
- White, J. E., 1983, *Underground acoustics*: McGraw-Hill Book Company. New York.

- Winkler, K., 1985, Dispersion analysis of velocity and attenuation in Berea sandstone: J. Geophys. Res., 90, 6793-6800.
- Winkler, K., 1986, Estimates of velocity dispersion between seismic and ultrasonic frequencies: Geophysics, 51, 183-189.
- Xu, C. T., Harris, J. H., Quan, Y. L., 2006, Flow properties estimation of porous materials with a model of dynamic diffusion: SEG expanded abstract, 1569-1572.